Characterization and emplacement modelling of gold deposition within the Franciscan complex: An example from the Los Burros mining district, California

by

Jacob Hughes

B.S., Western Kentucky University, 2015

A THESIS

submitted in partial fulfillment of the requirements for the degree

MASTER OF SCIENCE

Department of Geology
College of Arts and Sciences

KANSAS STATE UNIVERSITY
Manhattan, Kansas

2018

Approved by:

Major Professor
Dr. Brice Lacroix

Copyright

Abstract

The Los Burros mining district (LBMD) is located within the Lucia subterrane (Underwood et al., 1995) along the Sur- San Gregorio-San Simeon-Hosgri fault system of California's Franciscan complex. The LBMD presented an attractive gold prospecting and mining area during the late 19th and early 20th centuries. Recent interest in the area has focused on fault-offset modelling through thermochronology (Underwood et al., 1995, Chapman et al., 2016). However, the mechanism, conditions, and timing of ore formation in the area are poorly constrained due to a lack of academic interest and documentation. This research seeks to arrive at a better understanding of gold emplacement mechanisms in the LBMD through an examination of lithologic and structural controls coupled with source fluid composition and peak P/T constraints. Sampling and mapping of lithologies and structures within the vicinity of the LBMD were conducted during the summer of 2016. Samples were collected for clay-fraction and bulk-rock mineralogy via XRD analyses, petrographic inspection and interpretation, including fluid inclusion microscopy/microthermometry as well as Raman spectroscopy. These analyses were conducted in an endeavor to constrain and explain a previously identified regional thermal anomaly within the vicinity of the LBMD with the intention of characterizing and modelling the impacts of structural controls on gold deposition.

The results of this study suggest gold deposition from a gas-poor, metamorphic source-fluid with approximately 300 ppm CH_4, CO_2 density of 0.15 g/cm^3, and an average salinity of 1.7 wt % NaCl equivalent. These data, along with peak P/T conditions of ~285°C and 680 bars were inferred using input from illite crystallinity data, fluid inclusion microthermometry, and the application of the Raman spectroscopy of carbonaceous material (RSCM) geothermometer used by Lahfid et al. Gold mobilization from sulfide and carbonaceous-rich sediments through

polyphase deformation events led to emplacement along structural and lithologic contacts likely as a syn-orogenic event. Gold emplacement occurred during the reorientation of the regional structure by transpression.

Table of Contents

List of Figures

List of Tables

Acknowledgements

I’d like to thank my peers, committee members, and family for their continued support. None of this would have been possible without you.

Chapter 1 - Introduction

Orogenic gold is a class of gold deposition that includes deposits previously referred to as mesothermal gold, lode gold, shear-zone-hosted gold, greenstone-hosted gold, and turbidite-hosted gold (Groves et al., 1998). The uniting feature of these apparently disparate mineralization types is the intimate association, both spatially and temporally, with orogenic processes. Simply, orogenic gold refers to gold emplacement associated with accretionary and collisional orogens (Tomkins, 2013). Goldfarb et al. (2001) also note a close link between gold ore formation and granitoid emplacement, indicative of thermal events contemporaneous with orogeny or slightly afterwards. Fluid production via magmatic or metamorphic de-watering processes may then act to concentrate disseminated sulfides, and consequently gold, in sufficient quantities for viable gold ore formation. The implication is that the controls on orogenic gold occurrence are more strongly influenced by structural constraints (e.g., fault, shear zones, veins, etc.) on the migration of hot, gold-rich fluids than on the nature of host-rocks, as evidenced by the observed, non-unique associations between gold deposits and host rock lithology (Goldfarb et al., 2001).

Lindgren (1909) defined three "metallogenic epochs" (eras of pronounced ore formation) that began ~2.8 b.y. ago and are concentrated mostly during the Middle Archean, Neoproterozoic, and continuously throughout the Phanerozoic. It is postulated that a tectonic shift away from plume-driven, cratonic crustal formation to plate-driven, "Cordilleran-style" crustal accretion of long, discontinuous terranes, possibly as far back as 2.8 Ga, provided conditions amenable to gold ore emplacement (Goldfarb et al., 2001). These marginal, collisional events provided for zones of relative crustal weakness. Tectonic re-working and transpressional stresses allowed for the accumulation of supralithostatic pressures and gold-bearing fluid

migration along fault pathways (Groves et al., 1998, Goldfarb et al., 2001). According to Goldfarb et al. (2001) hydraulic pressure build-up of ore-bearing fluids may result in extreme fluid pressures (suprahydrostatic to lithostatic) that can cause sudden, violent displacement along faults or induce fracturing in surrounding rocks. Cyclical pressure build-up and release in some orogenic systems may be observed by multiple generations of ore deposition within vein deposits, each corresponding to a separate surge of hydraulically driven source fluid (Peterson and Mavrogenes, 2014). Formation depths for orogenic gold deposits also cover a wide range; anywhere from near-surface depths to depths up to 20 km. Groves et al. (1998) prescribe a secondary classification scheme to distinguish shallow emplacement (less than 6 km), so-called "epizonal classes", from intermediate (6-12 km) mesozonal classes, and deep emplacement (greater than 12 km) typified by hypozonal classes shown in **Figure 1-1** (Groves et al., 1998).

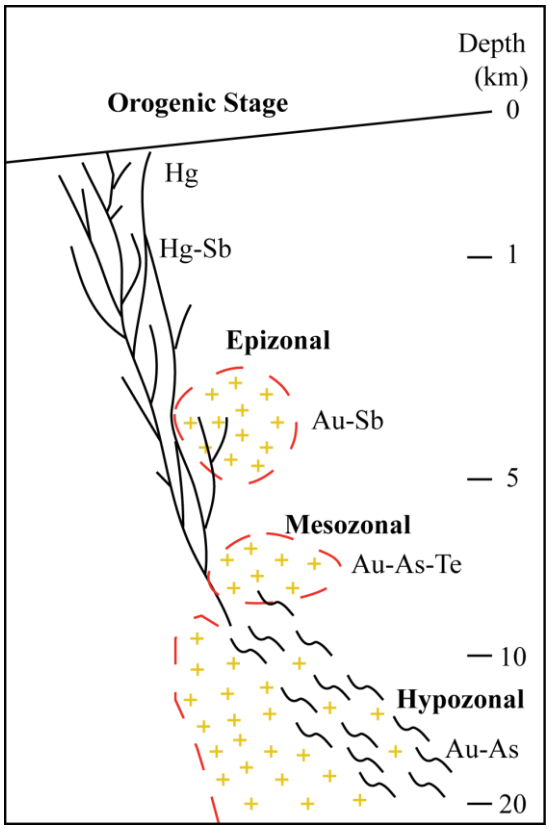

Figure 1-1. *Schematic visualization of gold formation at depth within the upper crust during orogenic activity (after Groves et al., 1998).*

Goldfarb et al. (2001) assert that orogenic gold occurrences and related deposits account for historic production over 1 billion ounces of gold, with Precambrian deposits accounting for roughly half of this total. Phillips (2013) estimates that 75% of total recovered gold worldwide originated from orogenic deposits. Orogenic gold occurrences within high-pressure, low-temperature settings (temperatures from 125 to 350^{o}C and pressures from 4 to 10 kbar) such as deposits hosted within the Sanbagawa metamorphic belt, Japan (Pohl, 2011; Moure and Enami, 2008), are less common than those associated with greenstone belts, and less studied. Therefore, characterization and investigation of emplacement mechanisms for these orogenic gold deposits are warranted to explain emplacement mechanisms within these marginal tectonic environments.

This study examines the Los Burros Mining District (LBMD) within Monterey County, California, to investigate gold emplacement within the HP/LT rocks of the Franciscan complex where the relationship between ore deposition and regional, blueschist-grade metamorphism is poorly constrained. In addition, this study tests the viability of the low-temperature RSCM geothermometer of Lahfid et al. (2010) in a unique tectonic environment to investigate a thermal anomaly reported by Underwood et al. (1995). This thermal anomaly is hypothesized to be a post-orogenic hydrothermal event related to LBMD gold deposition (Underwood et al., 1995; Lahfid et al., 2010). Previous research indicates isothermal temperature anomalies measured via vitrinite reflectance and illite crystallinity (Underwood et al., 1995) and low-temperaure RSCM geothermometry (Lahfid et al., 2010) are highest within the LBMD and cut across two metamorphic isograds (Ernst, 1980). These two metamorphic zones are I: pumpellyite ± prehnite and II: lawsonite ± pumpellyite, aragonite, jadeitic pyroxene shown in **Figure 2-1**. The LBMD contains a continuum from high anchizone to blueschist facies as supported by these data and the ubiquity of typical blueschist minerals such as glaucophane.

These observations lead to two questions that will be addressed in this thesis: Is gold deposition somehow tied to or influenced by a hydrothermal event which post-dates metamorphism and deformation? If so, what is the nature of this inferred hydrothermal event? In this study we propose to establish a structural model and to constrain the pressure-temperature conditions that control LBMD gold-deposition. To address this issue, we apply illite crystallinity, fluid inclusion microthermometry, and the Raman spectroscopy of carbonaceous material (RSCM) geothermometer. We further highlight the nature of the thermal anomaly and its relationship to LBMD gold-deposits within the Alder Creek study area.

Chapter 2 - Geologic and tectonic setting

2.1- Tectonic setting

The Los Burros mining district (LBMD), shown in **Figure 2-1**, lies within the Lucia subterrane of the Nacimiento block; a component of the Franciscan subduction complex of central coastal California (Underwood et al., 1995). It spans ~300 x 30 km of the Coast Ranges beginning ~10 km south of San Francisco Bay and continuing to its southern terminus at the Santa Ynez fault (Chapman et al., 2016). The Nacimiento block is bound to the east by the Salinian block at the Sur-Nacimiento fault (Page, 1970). The Nacimiento block is composed predominantly of accretionary wedge sediments from the late Jurassic to early Cretaceous, ages of which have been confirmed by U-Pb chronology on detrital zircons (Hall, 1991; Chapman et al., 2016). (Page, 1972; Ernst, 1980; Hall, 1991; Chapman et al., 2016; Lori, 2016). K-Ar dates from metamorphic potassium-bearing phases, such as micas, from the metamorphic zones described by Ernst (1980) place the timing of regional metamorphism at 70 to 80 Ma (Suppe and Armstrong, 1972).

Chapman et al., (2016) assert that the sediments of the Nacimiento block originate from southern California based on the elevated abundance of Late Cretaceous detrital zircons relative to Jurassic-Early Cretaceous detrital zircons. These criteria are established with respect to the relative younging trend of continental arcs in southern California versus central California (Ernst, 2015). Since subduction processes in southern California led to a westward younging arc, the relative proportions of “young” to “old” zircons are expected to be higher for sediments sourced in southern California as compared to central California. Thus, a ratio of “young” Late Cretaceous to “old” Jurassic-Early Cretaceous detrital zircons provides evidence of likely sediment provenance between the two distinct source regions. The predominance of Late

Cretaceous zircons suggests that the sediments of the Nacimiento block were not deposited in-situ, outboard of present-day central Californian continental arcs, but rather originated much farther south; likely experiencing a total offset of ~150 km (Clark et al., 1984; Chapman et al., 2016).

The Lucia and Point Sur subterranes from the Nacimiento block carry no evidence of an origin exotic to the rest of the Nacimiento block (Underwood et al. 1995). Subterrane delineation in this context is instead justified by position relative to regional fault systems. The Lucia subterrane, which contains the Los Burros district, is situated in the central portion of the Nacimiento block and lies between the San Gregorio–San Simeon–Hosgri fault zone and the western margin of the Salinian block (Underwood et al., 1995). The Lucia subterrane is bounded to the east by the Sur-Nacimiento fault zone (Page, 1970) (**Figure 2-1).**

The San Gregorio–San Simeon–Hosgri fault zone intersects the prevailing San Andreas dextral strike-slip fault system farther to the north, just west of San Francisco (**Figure 2-1** and **Figure 2-2**). Underwood et al. (1995) used vitrinite reflectance and illite crystallinity (IC) to estimate fault displacement and offset of the San Gregorio-San Simeon-Hosgri fault zone separating the Point Sur to Lucia subterranes. These authors describe Neogene-Quaternary offset totaling only 5-10 km between Point Sur and Lucia subterranes. It is unclear whether dextral offset is transferred within the study area of the Lucia subterrane via a single, through-going fault system, or a series of discontinuous fault segments, since delineating fault-coastline intersections and fault segment relationships is complicated by off-shore fault components (Hall, 1991; Underwood, 1995).

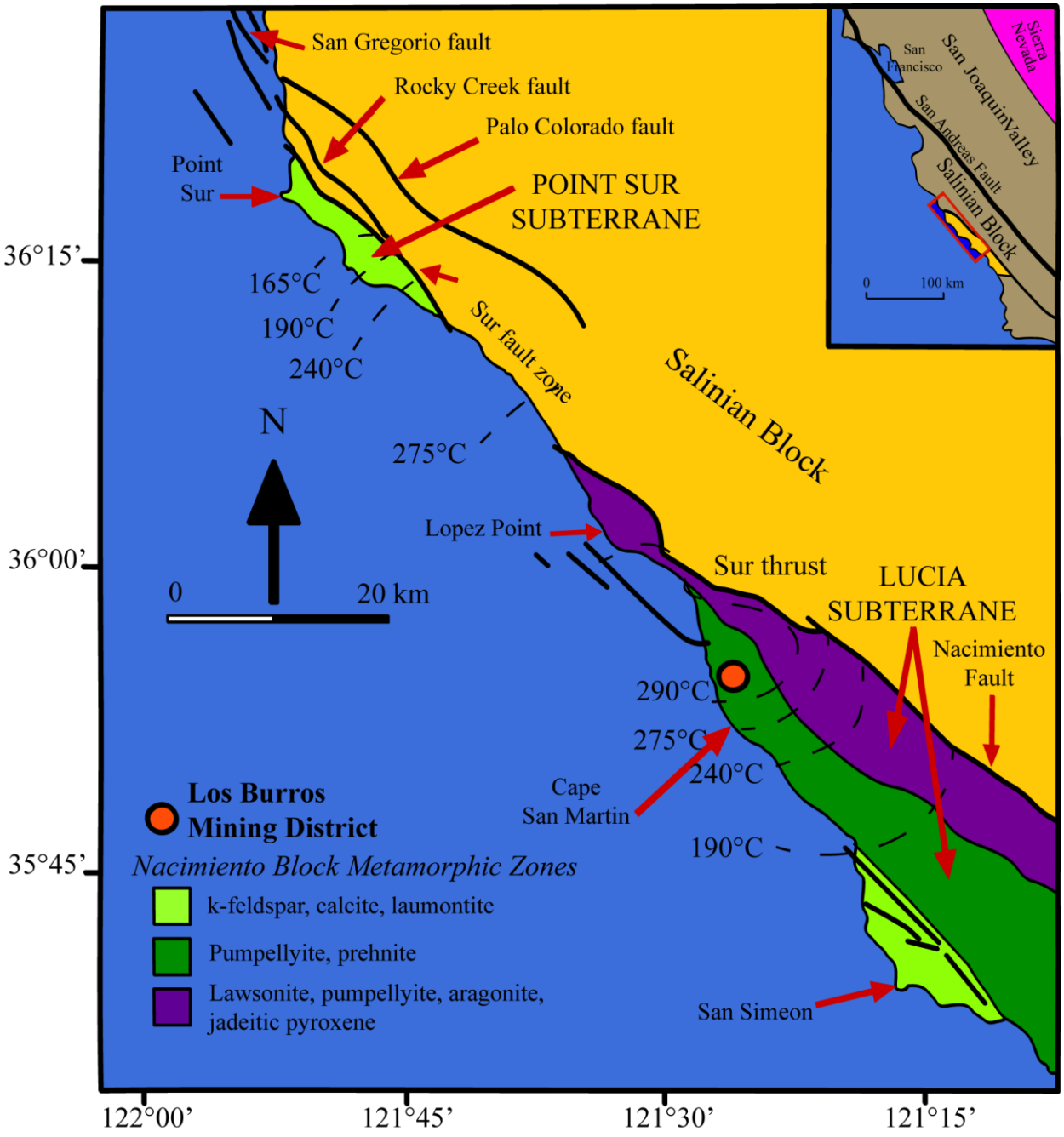

Figure 2-1. *Geologic map highlighting the Lucia subterrane and the relative location of the Los Burros gold district.* Modified from Lahfid et al. (2010). Dashed lines are temperature contours calculated on the basis of illite crystallinity by Underwood et al. (1995).

2.2- Thermal anomaly

Based on both vitrinite reflectance (Rm) and illite crystallinity methods, Underwood et al. (1995) suggested that the Nacimiento block is locally perturbed by a thermal anomaly (up to ~300ºC) in the vicinity of Cape San Martin and the LBMD (**Figure 2-1**). More recently, Lahfid et al. (2010) expound upon this thermal anomaly through the application of the Raman spectroscopy of carbonaceous materials (RSCM) geothermometer to independently corroborate the presence of a thermal anomaly centered on the LBMD.

The vitrinite isoreflectance contours proposed by Underwood et al. (1995) cut regional metamorphic isograds (Ernst, 1982), suggesting a post-orogenic hydrothermal event (Underwood et al., 1995) Although both the thermal anomaly and LBMD deposits seem spatially correlated, their relationship is still poorly constrained.

2.3- LBMD history and geology

2.3.1- Mining history

The LBMD covers an area of ~50 km^2 in the southwestern corner of Monterey County, California, near Cape San Martin. The district lies principally within T 23 and 24 S, R 25 E of the Mount Diablo meridian (Hamilton, 1916) shown in **Figure 2-2**. Furthermore, early accounts suggest that most of the mining activities were confined within the drainages of Willow and Alder creek (**Figure 2-2**).

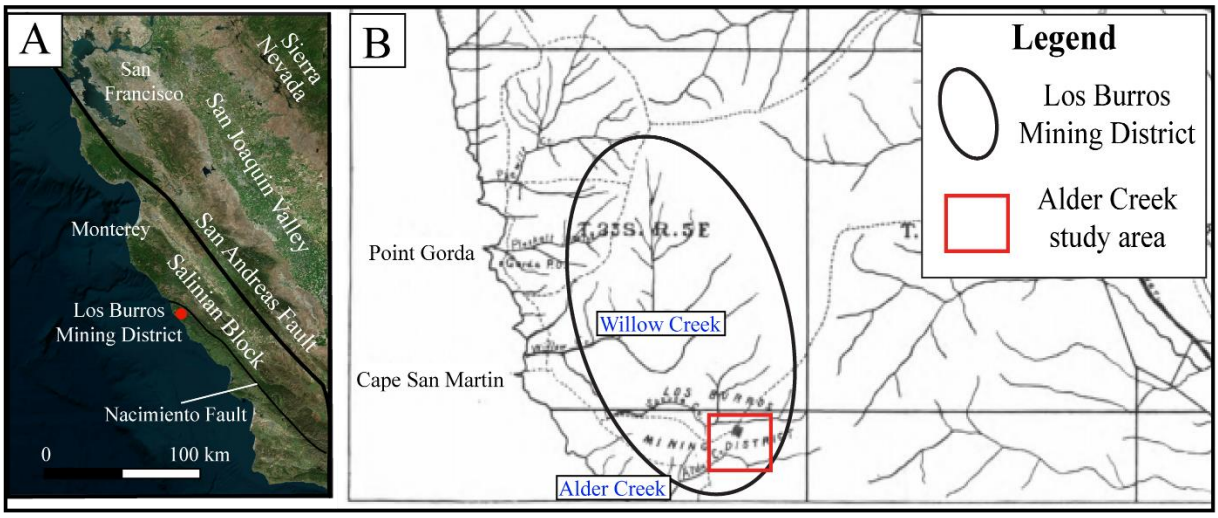

Figure 2-2. *Map showing the location of the LBMD. A) Google Earth image of the region. B) Location of the Alder Creek study area* (after Davis, 1912).

The first documented mining activities within the LBMD began in 1876 when the district was first incorporated (Trelan, 1888). Early mining activities were limited to placer mining of loose, raised gravel deposits and beach terraces (Hamilton, 1916). Little development and production in the region occurred until the discovery of the Last Chance (later renamed to Buclimo) deposit and adjoining properties within the Alder Creek drainage in 1887 (Hill, 1922). The Alder Creek properties were the focus of production until around 1902 when discoveries of nuggets and placers made on Spruce, Willow and Plaskett Creeks to the northwest led to the formation of the Gorda Mining Company (Hill, 1922). Production of modest tonnages of gold ore (~329 tons of ore from 1912 to 1914) were extracted until around 1921 (Hill, 1922). Total production value from recorded LBMD ore during this time was ~$90,000 (California State Mineralogist annual report, 1916) or nearly $2.2 million when adjusted for inflation as of 2017 when using the United States Department of Labor's CPI Inflation Calculator (https://data.bls.gov/cgi-bin/cpicalc.pl)

Early descriptions of the dominant units of the LBMD include dark, greenish-gray micaceous sandstones with fine conglomerate lenses, black shale, slate, and lenses of coarse arkosic sandstone. (Davis, 1912; Hamilton, 1916; Hill, 1922). This is in general agreement with modern accounts of regional lithology, which describe well-bedded turbidite sequences and deformed mélange deposits of sandstone and greywacke (Gilbert, 1973; Page, 1981; Hall, 1991; Graymer et al., 2014). Hill (1922) also reports the occurrence of two more-or-less continuous belts or dikes of serpentinite ~610 m apart with a west-northwest trend through the south-central part of the LBMD.

Of note is the association of gold and sulfide-bearing quartz and calcite veins with serpentinized units consisting of parallel sets of discontinuous veins, ranging from ~25 cm to ~1 m in width (Hamilton, 1916; Hill, 1922). Gold-bearing veins oriented N315°/35° are described as variably conformable or cross-cutting with respect to host shales near serpentinite (Hamilton, 1916). Mineralization within the Last Chance/Buclimo mine is characterized by native gold, pyrite, chromite, and mariposite within multiple quartz stringers ~1.2 to ~5 cm in width oriented N280-290°/60-85°, paralleling regional tectonic fabrics. Additional mineralization including arsenopyrite as well as minor chalcopyrite, sphalerite, and galena is reported throughout other properties within the LBMD (Davis, 1912; Hamilton, 1916; Hill, 1922).

2.3.2- Local lithology

Four lithological units are encountered within the study area (unit names adopted from Graymer et al., 2014). Lithologic units, in order from oldest to youngest, are: Serpentinite (Jsp), Chert (KJfc), Broken Formation (KJfb), and Mélange (Kfm).

Serpentinite (Jsp) is characterized by extensive serpentinization of mafic and ultramafic rocks, including the presence of serpentinized pillow basalts (shown in **Figure 4-1** B)**.** Jsp also

includes blue-gray serpentinite and glaucophane schist. The unit is interpreted to be a Jurassic-age member of the Coast Range ophiolite sequence (Graymer et al., 2014). Jsp is the most recognizable unit due to the presence of unique and easily identifiable mineral assemblages most commonly containing lizardite ± glaucophane ± wollastonite ± augite.

Chert (KJfc) occurs as ribbons, blocks, or lenses of chert embedded within shale or slate. Chert may crop out within units Kfm and KJfb where they have been tectonically emplaced within the mélange. Dating of radiolaria from this unit gives an age range from Middle Jurassic to Early Cretaceous (Seiders, 1989a, b). Although occasionally visible in outcrop, chert is locally discontinuous and commonly found as lenses within overlying units. It is not included as one of the three defining units shown in **Figure 4-10** and **Figure 4-11** for this reason, but this will be discussed in greater detail in a later section.

The Broken formation (KJfb) is comprised predominantly of greywacke, shale, metagraywacke and slate. Due to the intense deformation this formation has been structurally disrupted to include minor amounts of chert and basalt. The age of this chert is unclear (Graymer et al., 2014), but appears to be Cretaceous to possibly Late Jurassic.

The Mélange (Kfm) is the most structurally and lithologically complex unit observed and, as such, corresponds to a tectonic mélange. It is comprised of an argillic matrix enclosing blocks of comglomerate, greywacke, chert, serpentinite, and glaucophane schist (shown in **Figure 4-1** C). Dating of radiolarians from chert blocks within this unit indicate Late Triassic to Late Jurassic radiolarians (Graymer et al., 2014). Conglomerate cherts were found to contain Late Triassic to Late Jurassic radiolarians (Seiders, 1989a), while other chert blocks have revealed the presence of Early Jurassic to Early Cretaceous radiolarians. Detrital zircon grains

from some Santa Lucia Range greywackes have yielded Late Cretaceous ages corresponding to a maximum depositional age of 90 – 77 Ma (Morisani et al., 2005).

Chapter 3 - Methods

3.1- Mapping and sampling

All mapping and sampling of the Los Burros area was conducted during an eight-day field season in the summer of 2016. Measurements of structures, including bedding (S_0), schistosity (S_1), faults (F), and fold axes (A_0), were recorded and their locations marked using a UTM coordinate system. Coordinates were converted to decimal degrees to properly project them with basemaps acquired from the USGS (https://pubs.usgs.gov/of/2005/1305/). Detailed notes, sketches, and photos of structures and outcrops were made and these data, in conjunction with aerial photographs and pre-existing regional maps (Graymer et al., 2014), were used to create the study area maps depicted below.

Thirty-four samples were collected from various portions of the study area to provide an accurate representation of observed lithologies (shown later in **Table 4-1** and **Figure 4-1**). A minimum sample size requirement of $1dm^3$ was imposed to ensure that enough sample material was available for the creation of thin sections as well as illite crystallinity and bulk-rock XRD analyses. Representative samples were selected and field-trimmed to remove highly-weathered surfaces before being placed in separate, doubly-layered sample bags to minimize contamination. Field notes, along with hand sample and petrographic observations were combined with XRD analyses to assign sample lithologies.

3.2- XRD analyses

3.2.1- Bulk rock XRD

X-ray diffraction was systematically applied on both bulk-rock and clay fractions (see **section 3.2.2** for greater detail) from each sample to estimate the mineral assemblage. These

analyses were also conducted to corroborate and augment thin section observations concerning mineralogy and metamorphic facies. Twenty-nine samples were selected for XRD mineral identification analyses. Samples were first cut using a rock saw to produce fresh material or material with as much weathering or alteration removed as possible. Thin sections were then made for selected samples from the remaining, un-weathered rock with care to preserve quartz veins where applicable. 40 g of material were selected, and care was taken to preserve a minimum 25 g split for use in clay fraction XRD analyses.

Samples were first disaggregated using a steel mortar and pestle until they were no larger than 2 mm. A shatterbox with an alumina ceramic puck and assemblage was used to minimize sample contamination. A run-time of six minutes per sample was implemented to produce a fine, uniform powder. The puck and assemblage were both thoroughly rinsed and cleaned in between runs.

Samples were front-loaded into stainless steel disks using a scoopula to facilitate proper packing within the sample holder for XRD analysis. Pressure was applied with the help of a glass tile during the packing stage to ensure maximum compaction. Once all samples were properly prepared, bulk powders were analyzed using a PANalytical Empyrean XRD at 45 kV and 40 mA and CuKα radiation using a 0.04 rad Soller slit from 5°2θ to 70°2θ at a rate of 2.4°2θ/min.

3.2.2- Clay fraction and illite crystallinity

Illite crystallinity samples were prepared for clay separation via acid wash. Samples were exposed to a 10% hydrochloric acid attack to dissolve any carbonate material. This step was conducted under a fume-hood while samples were stirred periodically for 10 minutes to ensure that the acid and sample were thoroughly allowed to interact. Both sample and acid were then

poured into centrifuge bottles and weighed. DI water was added as necessary to normalize the weights of each centrifuge bottle.

Next, illite crystallinity values were recorded with the intention of comparison between published values by Underwood et al. (1995) as well as temperature estimates from the RSCM geothermometry method used in this study (as described in section 4.5). Sample material leftover from the XRD analyses were powdered using a steel mortar and pestle. Alteration of mineral structure due to mechanical processes during sample preparation could impact an assessment of illite crystallinity. Therefore, care was taken not to over-powder any samples to avoid perturbation of the less than 2 μm size fraction. Disaggregated splits of ~25 g for each of the sedimentary and metasedimentary samples (16 samples total) were prepared using a steel mortar and pestle. The mortar and pestle were washed with DI water and thoroughly cleaned between each sample.

Samples were placed in the centrifuge and run at 5000 rpm for ten minutes to ensure that all size fractions were compressed to the bottom of the centrifuge bottle. Care was taken to ensure there was no loss of sample from the bottom of the bottle. DI water was added once more to each bottle to normalize the weights and ensure an equal weight distribution. Each sample was then thoroughly shaken to dislodge sediment plated to the bottom before being placed back into the centrifuge again for ten minutes at 5000 rpm. This wash and rinse cycle was repeated until a pH of 7 was reached.

45 ml was then transferred into 50 ml Falcon centrifuge tubes and placed back in the centrifuge. Exact parameters for the next centrifugation process to separate out the less than 2 μm size fraction were calculated through manipulation of Stokes' Law (eq.1) (Moore and Reynolds, 1997).

$$V_T = g(d_p - d_1)D^2/18\eta \qquad \text{eq.1}$$

In this equation, V_T is terminal velocity, g is the force of gravity (in cm/sec^2), $d_p - d_1$ is the difference between particle and liquid density, D^2 is the diameter of the particle in cm^2 and η is the viscosity of the liquid through which the particle is settling. Modification of this equation to solve for settling time within a centrifuge cylinder was carried out for a given centrifuge speed of 1000 RPM. The parameters relevant to the final calculation of velocity and time were as follows: volume of sample to be extracted, radius to top of sample volume (R_1), and radius to the bottom of the desired volume to be sampled (R_2). For this study the volume was 10 ml, R_1 was 7 cm and R_2 was 10.5 cm. With these variables known, it was calculated that the centrifuge should be calibrated for a run-time of approximately 0.82 minutes or 49 seconds to produce an accumulation of the less than 2 μm size fraction within the uppermost 10 ml of the centrifuge tube. Additionally, the 2 μm to 16 μm size fraction was also isolated. This was accomplished by first shaking up the sample to put any settled material back into suspension before allowing the sample to settle normally under gravity settling. The time required for this size fraction to be concentrated within the uppermost 2 cm of the tube was calculated to be 1 minute and 17 seconds (Jackson, 1969).

10 ml of sample containing less than 2 μm fraction were extracted from each sample. The sample was then dropped over a glass slide using a pipette and allowed to dry overnight (Moore and Reynolds, 1997). This process was repeated once more to produce enough material to be conducive for quality XRD diffraction patterns. This method is preferable for the needs of this study, since the action of gravity settling due to the evaporating DI water is sufficient to align the particles in along the 001 crystallographic planes. The same slide mount method was employed for the 2 - 16 μm size fraction as well. Clay fraction splits for both the less than 2 μm and the 2 -

16 μm size fraction for each sample were analyzed using a PANalytical Empyrean XRD at 35 kV and 20 mA and CuKα radiation using a 0.04 rad Soller slit from 3.5°2θ to 50°2θ at a rate of 2.4°2θ/min.

Ethylene glycol solvation was applied to the less than 2 μm fraction prior to XRD analysis. Ethylene glycol was poured into the base of a desiccator to a depth of approximately 1 cm. Samples were placed on a shelf within the desiccator and exposed to the vapor for a minimum of 8 hours following a procedure prescribed by Moore and Reynolds (1997). Samples were then removed and analyzed using a PANalytical Empyrean XRD at 35 kV and 20 mA and CuKα radiation using a 0.04 rad Soller slit from 3.5°2θ to 50°2θ at a rate of 2.4°2θ/min.

Illite crystallinity was calculated for both the untreated and treated clay slides with MacDiff using the full-width-at-half-maximum (FWHM) for the 001 illite peak after Kübler (1964).

3.3- Petrography and fluid inclusion microscopy techniques

Thin sections were made of host rock and host rock-and-vein where applicable. Thin sections of samples deemed to be representative in terms of composition were selected and analyzed to augment bulk-rock analyses and provide insight into vein mineralogy and growth. Samples were professionally made by National Petrographic Service, Inc. Twelve samples were selected for analyses including: petrography, fluid inclusion microthermometry and Raman microscopy. Three of these samples (LB16-08a, LB16-21, and LB16-24) contained quartz veins and were selected for fluid inclusion microscopy; they therefore, required doubly-polished sections with a thickness of ~100μm. Doubly-polished thick sections are preferred for this method of analysis as the above average thickness allows for the preservation of a greater

number of fluid inclusions. The polishing on both sides helps to promote greater optical purity throughout the sample regardless of whether it is viewed from the top or the bottom. The remaining nine samples were examined to aid with sample identification and the construction of a modal mineralogy by sample.

Thin and thick sections were inspected using a Nikon Eclipse E600 POL microscope. Petrographic inspection and description of each thin section was carried out (see Appendix) to identify mineral assemblages indicative of regional metamorphic facies: prehnite-pumpellyite facies (characterized by prehnite + pumpellyite ± chlorite ± albite ± quartz) and blueschist facies (variably characterized by minerals such as glaucophane ± lawsonite ± chlorite ± epidote ± omphacite) (Ernst, 1980; Blatt & Tracy, 1995). Samples containing quartz veins were also scrutinized to determine vein composition and principal growth direction.

Fluid inclusion assemblages (FIAs) observed in quartz veins both proximal (samples LB16-21 and LB16-24) and distal (sample LB16-08a) to noted mine locations (see **Figure 4-3**) were identified using a Nikon Eclipse LV100N POL microscope. Fluid inclusions are a valuable geothermometric tool since liquid, vapor, and solid phases within an inclusion were once in equilibrium in the fluid phase prior to entrapment. Heating to a certain, critical temperature will result in the re-equilibration of any disparate phases within the inclusion. This critical temperature is termed the homogenization temperature (T_h). Therefore, this property provides a useful tool with which to bracket the minimum temperature of the primary fluid prior to entrapment. Fluid inclusion studies are also typically conducted with a measurement of the melting temperature (T_m) to estimate salinity/vapor phase composition based on the depression of the freezing/melting point from that of pure H_2O. Deviation of T_m from that of pure H_2O can be converted to an equivalent NaCl wt% as a measure of primary fluid salinity. Salinity was

calculated in this way using the procedure outlined by Bodnar (1980) and compared with reference values provided by Frezotti et al. (2012).

The logic behind this procedure is two-fold. Conducting a measurement of T_h first prevents potential elastic deformation which may occur if a measurement of melting temperature (T_m) is carried out first instead. This is due to expansion caused by the freezing of liquid (generally close to pure H_2O) required for T_m determination. Fluid inclusion expansion produces artificially biased T_h measurements, because it invalidates the assumption that the fluid inclusion as an isochoric system (i.e. a constant-volume state) (Goldstein and Reynolds, 1994, Roedder and Bodnar, 1980). Fluid inclusion expansion is exaggerated when an inclusion with a small vapor to liquid ratio is frozen (Roedder and Bodnar, 1980).

The second reason is that by measuring the lowest T_h inclusions first one can obtain valid data without the risk of inclusion decrepitation. This decrepitaion can be caused by over-pressurization caused by excessive heating. Differences between the homogenization temperatures of different populations of fluid inclusions can be quite significant. If a fluid inclusion which equilibrated at a lower temperature is subjected to too much heating, it can lead to sufficient pressure build-up within the inclusion to cause it to rupture (Goldstein and Reynolds, 1994). For this reason, all inclusions which equilibrated within the same temperature range were sought out first within each zone before obtaining higher T_h measurements.

Two-phase liquid and vapor fluid inclusions comprised the majority of FIAs. FIAs were analyzed using a Linkam THSMG600 heating and cooling stage. Analysis of fluid inclusions and fluid inclusion assemblages (FIAs) for this study follow the methods defined by Roedder (1984) and Goldstein and Reynolds (1994). A total of one hundred and seventy fluid inclusions from eight zones of interest were analyzed (See reference tables in Appendix B, **Table B-1** to **Table**

B-4). Measurement of the homogenization temperature (T_h) of fluid inclusions was determined in accordance with the procedure of Goldstein and Reynolds (1994). Samples were gradually heated at a rate of 10˚C/s to 5˚C/s to a temperature where the vapor bubble was no longer visible. The sample was then cooled slowly back to the temperature where the bubble was last visible. Incremental temperature increase coupled with a subsequent cooling period, a process termed cycling, was repeated until the bubble no longer re-appeared at its last visible temperature (Roedder, 1984; Goldstein and Reynolds, 1994). Each fluid inclusion was then allowed to undercool by 20˚C to 30˚C to see whether the bubble continued to remain absent. This was done to ensure that the vapor phase did not reach a point of metastability and that the recorded temperature was in fact representative of T_h. Repeated cycling steps were carried out at gradually increasing temperatures for each inclusion to bracket T_h within a ± 0.5˚C margin.

Collection of melting temperature data involved the gradual cooling of samples at a rate of 10˚C/s to 5˚C/s and eventually at 1˚C/s from -35˚C to -45˚C to observe the temperature at which the inclusion was observed to solidify. This temperature is noted as the freezing temperature (T_f). Once the freezing temperature was met, samples were further cooled to -100˚C to ensure the complete freezing of all phases. Heating of samples occurred until -20˚C, where the heating rate was slowed. The rate was lowered from 5˚C/s to 1˚C/s to observe a temperature of first ice-melt (T_{mi}). First ice-melt temperatures were difficult to observe due to the small size (less than 20 µm) of many observed fluid inclusions. Thus, successful T_{mi} determinations were only recorded for a subset of the fluid inclusion microthermometry data. T_m, corresponding to the last ice-melt temperature, was considerably easier to observe as the inclusion could be seen to suddenly, and dramatically, return to an all liquid or liquid + vapor state.

3.4- Raman microscopy

Raman microscopy was conducted with two goals in mind: 1) to aid in fluid inclusion liquid and vapor phase identification and 2) calculation of temperature based on the structural deformation of carbonaceous material. A Renishaw InVia Raman microscope was used to analyze the composition of both fluid and gas phases from representative fluid inclusions and inclusions which contained otherwise unidentifiable phases. A 532 nm Ar-laser was focused on the sample by a Leica microscope with a 100x objective. Beam power was limited to a maximum of 10% (corresponding to ~2mW) to minimize the risk of inclusion decrepitation due to beam exposure. Furthermore, exposure time was limited to a maximum of three seconds for each of three accumulations. Spectra for characteristic fluid inclusions from multiple FIAs within each sample were collected. Identification of liquid and vapor phases was aided by the criteria and spectral references provided by Frezzotti et al (2012) and the RRUFF database (Lafuente et al., 2015).

Raman spectroscopy of carbonaceous material (RSCM) was conducted on twelve carbonaceous-rich sediments (**Table 4-3**). Beam intensity was kept below 10% beam power for these analyses to prevent burning of carbonaceous material and to avoid biasing of spectra used in the RSCM calibration method of Lahfid et al. (2010) (Lünsdorf, et al., 2014). At least fifteen carbonaceous material spectra were collected from each thin section, up to a maximum of thirty-three spectra for the most carbonaceous samples.

Data processing, such as background correction and peak-fitting, was carried out using the Wire4.3 software associated with the Renishaw InVia Raman microscope. Scans were conducted over the range of 700 to 2000 relative wavenumbers to accurately constrain the baseline, mirroring the procedure of Lahfid et al. (2010). Background corrections, a potential

source for significant error and biasing in RSCM calculations (Lunsdorf, et al., 2014), were carefully executed and a Lorentzian curve-fitting profile was used to best replicate the carbonaceous material spectra.

RA1, a parameter used in assessing carbonaceous material deformation within the temperature range of 200°C to 350°C (Lahfid, et al., 2010), was calculated by measuring the area of the D4 and D1 bands against the total area as defined by the areal sum of the D4, D1, D3, G s.s., and D2 bands (see **Figure 3-1**). The G s.s. band corresponds to the expected peak position of graphite while the D1, D2, D3, and D4 bands are theorized to represent defects within the structure of the carbonaceous material (Lahfid et al., 2010). Area calculations were carried out using the curve-fitting algorithms within the Wire4.3 software and corroborated using similar calculations carried out using Fityk (http://fityk.nieto.pl/) curve-fitting software (Lunsdorf et al., 2014).

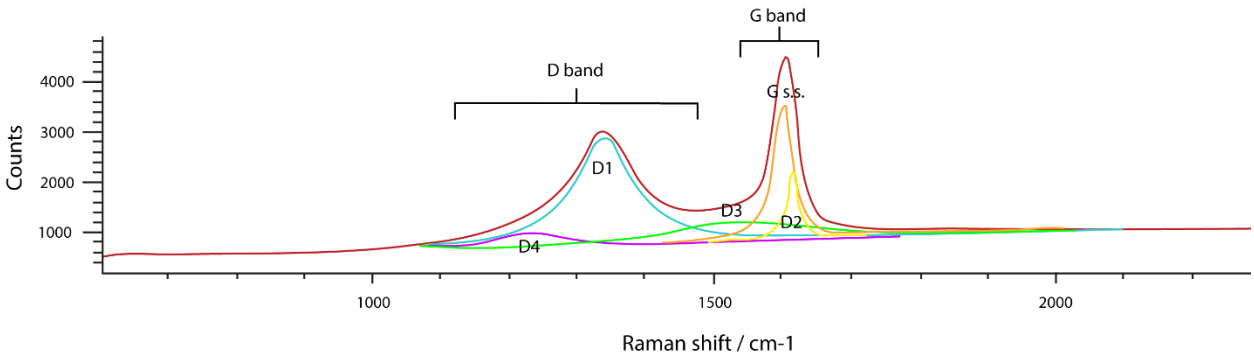

Figure 3-1. *Representative spectra from LB16-25d depicting idealized D and G bands along with their components*

Chapter 4 - Results

4.1- Petrographic descriptions

Each of the 18 prepared thin sections were examined under a petrographic microscope. **Figure 4-1** highlights a few notable sampling locations and structures. Rudimentary petrographic descriptions were carried out on each thin section to assist with unit classification to create the geologic map shown in **Figure 4-8**. Point counts were not carried out for modal estimates since determining a highly accurate modal mineralogy by sample was not required for the purposes of this research. Please see Appendix B along with **Figures B-1** through **B-17** for descriptions and photographs of each thin section.

Figure 4-1. *Field photos. A) Abandoned mine shaft within a fold hinge. B) Pillow basalt boulder. C) Flysch clast within Kfm mélange. D)Myolinitic fabric exposed along Alder creek.*

4.2- Structural analyses

Structural trends to the west of Alder Peak have an attitude of N310-290°/20-60° before taking on an attitude of N315°/65-70° toward the Nacimiento River to the east (Hill, 1922). Hill (1922) also describes three major faults proximal to the region, noting fault scarps along the Nacimiento River to the east and a coastal scarp both trending ~N320°, as well as a major fault in the southern portion of Willow Canyon striking N290°. Measured structural features such as faults, S_0, S_1, fold axes, are shown in **Figure 4-2** alongside abandoned mine workings observed within the Alder Creek study area. Examples of tectonic fabrics (S_0, S_1, A_0) measured at different locations (**Figure 4-3**) are presented in **Figure 4-4**.

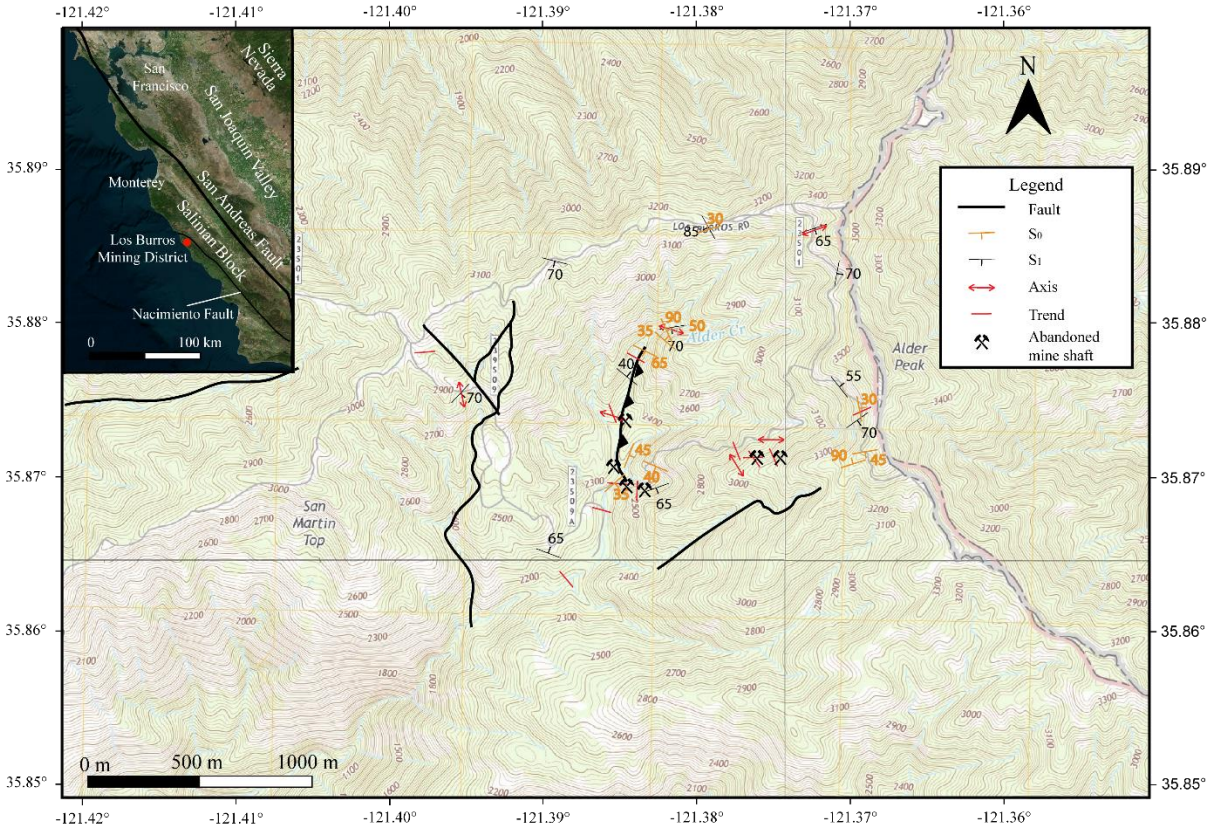

Figure 4-2. *Measured structures and abandoned mine shaft locations within the Alder Creek study area.*

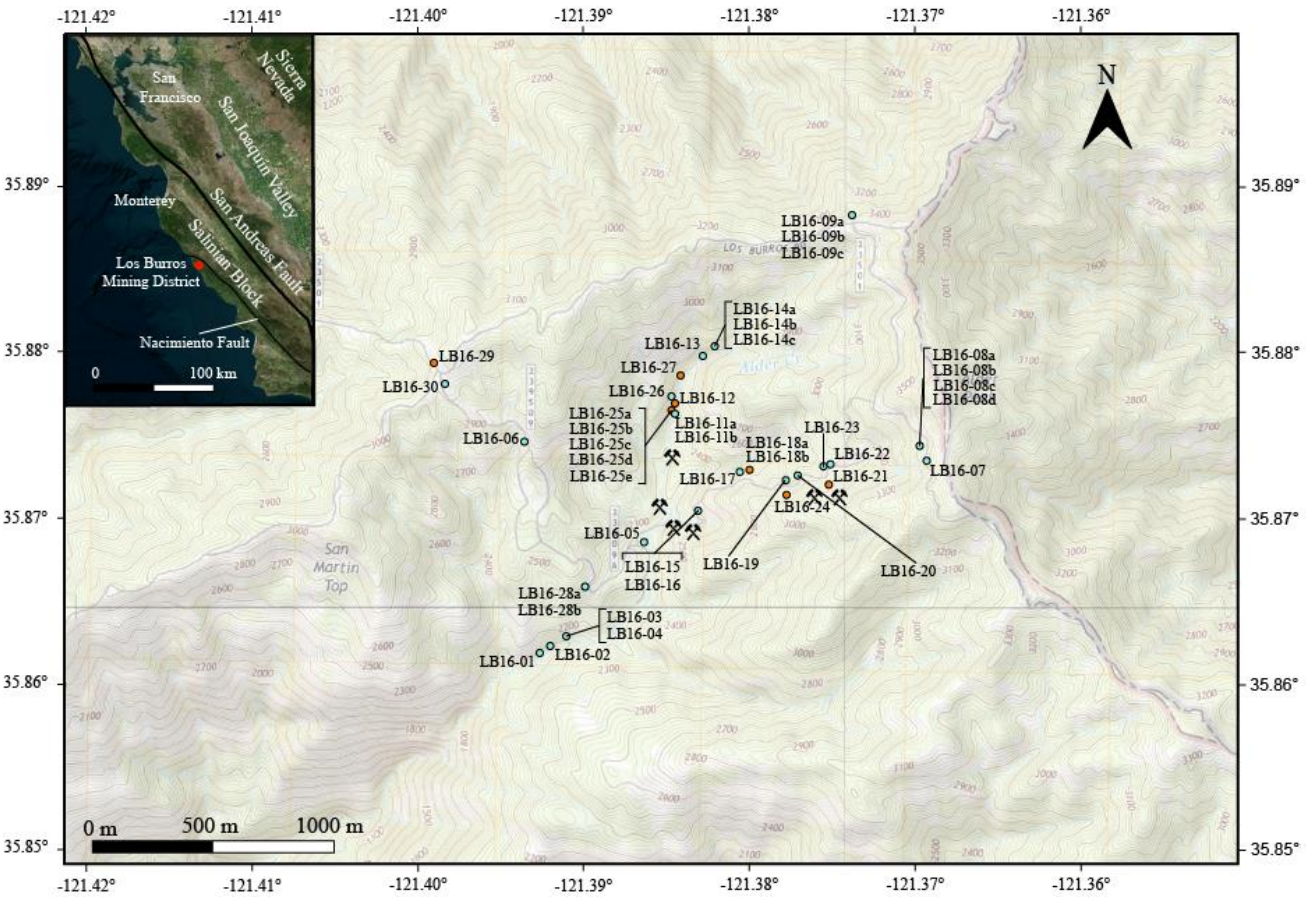

Figure 4-3. *Sample locations within the Alder Creek study area.* Orange dots signify samples which were also used for RSCM analyses.

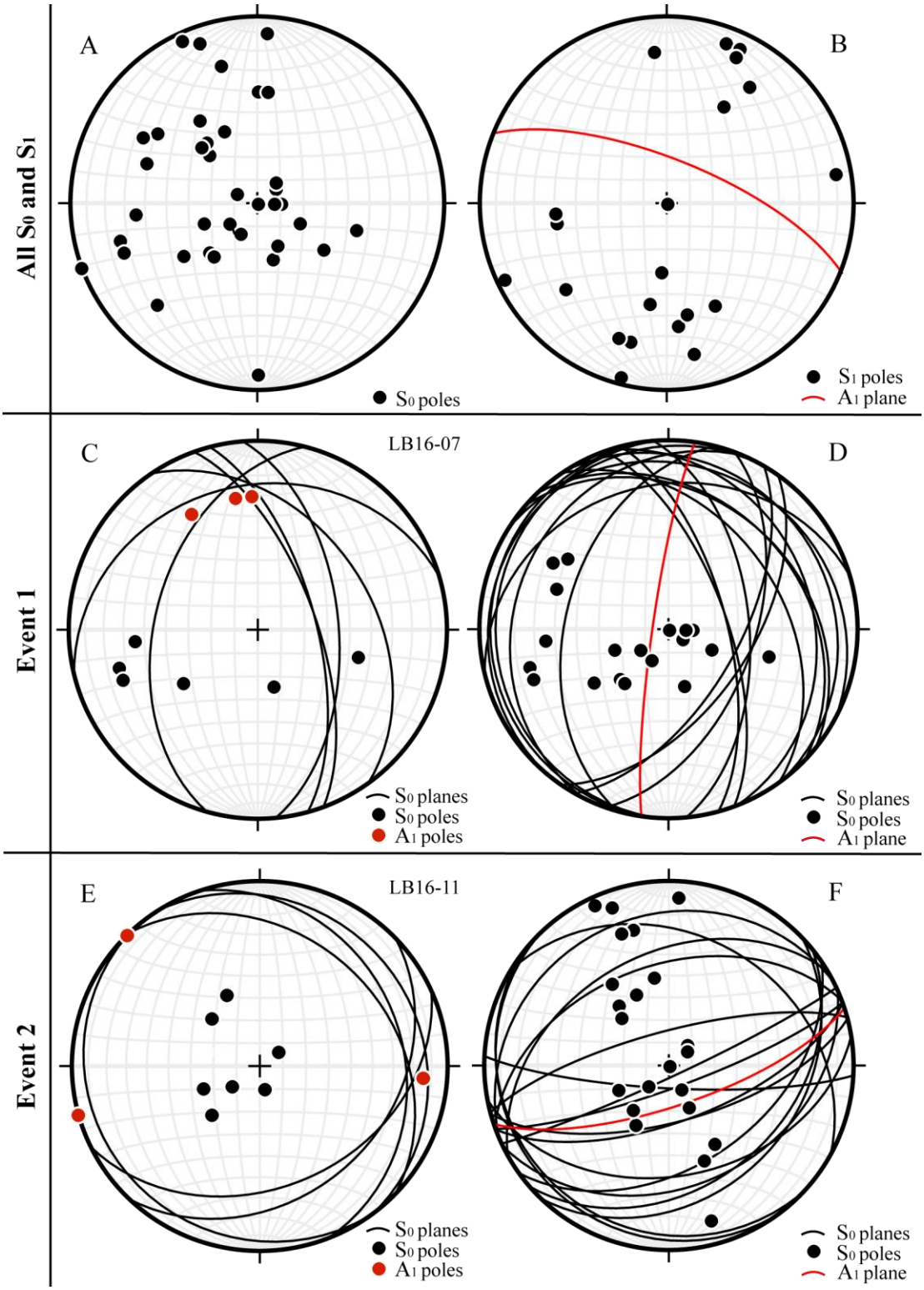

Figure 4-4. *Deconvolution of primary deformational events affecting the Alder Creek study area.*

Overall, the poles to S_0 (**Figure 4-4** A) are randomly distributed, suggesting a polyphased tectonic environment associated with multiple instances of fold interference. This is confirmed by plotting the schistosity (**Figure 4-4** B), which implies net folding oriented N292. A tectonic deconvolution highlighting only one component in select outcrops is applied in **Figure 4-4** C and **Figure 4-4** E to refine the different tectonic events that affected the area. Two broad deformational events, termed Event 1 (E1) and Event 2 (E2), responsible for the regional fabric of the Alder Creek study area, are interpreted from these data.

Event 1 (E1) is exemplified at location LB16-07 and is characterized by a fold oriented N350°/30° (**Figure 4-4** C). All measured values for S_0 oriented within a tolerance of ± 30° of N350° are shown in **Figure 4-4** D. Based on these data, it is apparent that E1 resulted in fold axis orientations which were roughly N-S. The axial plane of the folded chert shown in **Figure 4-5** displays this near N-S orientation connected to E1 deformation. Maximum principal stress during E1 is, therefore, concluded to be perpendicular to this subduction margin (similar to the subduction margin shown in **Figure 4-8**) with an orientation that is nearly E-W. This fold direction is hypothesized a product of regional compression and metamorphism associated with subduction and accretion of the sediments of the Nacimiento block.

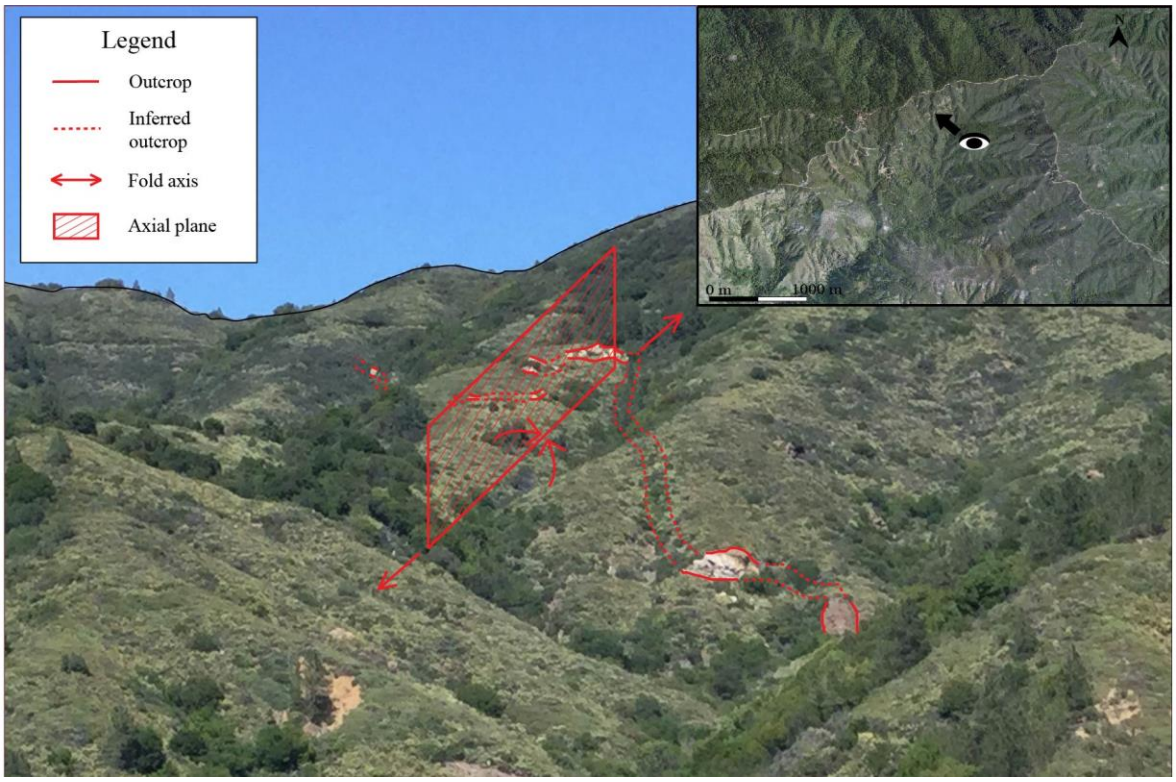

Figure 4-5. *Anticlinal axial plane inferred from chert outcrop observed in the field.*

Figure 4-4 E shows the tectonic fabrics measured at location LB16-11. All measured S_0 are scattered along a π-plane suggesting a fold oriented ~N255, representative of reorientation tied to Event 2 (E2). From these data E2 deformation can be seen to produce fold axes oriented roughly east-west. **Figure 4-6** displays this E2 trend observed in another chert outcrop.

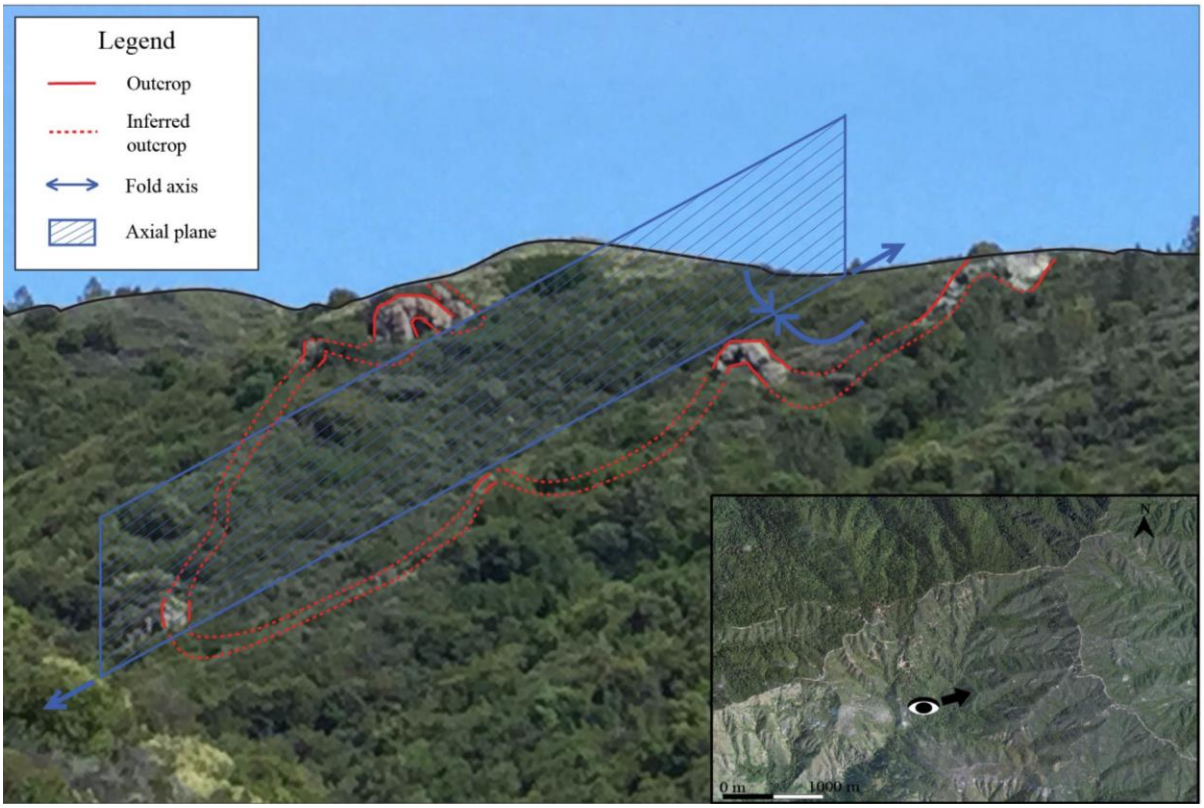

Figure 4-6. *Synclinal axial plane inferred from chert outcrop observed in the field.*

The average S_1 orientation is roughly N275°/65°, which is consistent with E2 fold reorientation. All Alder Creek S_1 may be plotted on an axial plane, which is roughly N290°/80° (**Figure 4-4** B). The absolute direction of σ_1 cannot be inferred from these data due to polyphase deformation from E1 and E2. However, discrepancies between the two values indicate that a composite between E2 and E1 principal stresses is most likely to form the regional fabric observed within the Alder Creek study area (**Figure 4-7**).

Figure 4-9 provides a schematic map of the local geology. Field observations along with lithologic and structural data were used to construct two principal cross-sections: one running approximately east to west across Alder Creek valley (**Figure 4-10**) and the other running approximately perpendicular to structures observed in the study area (**Figure 4-11**).

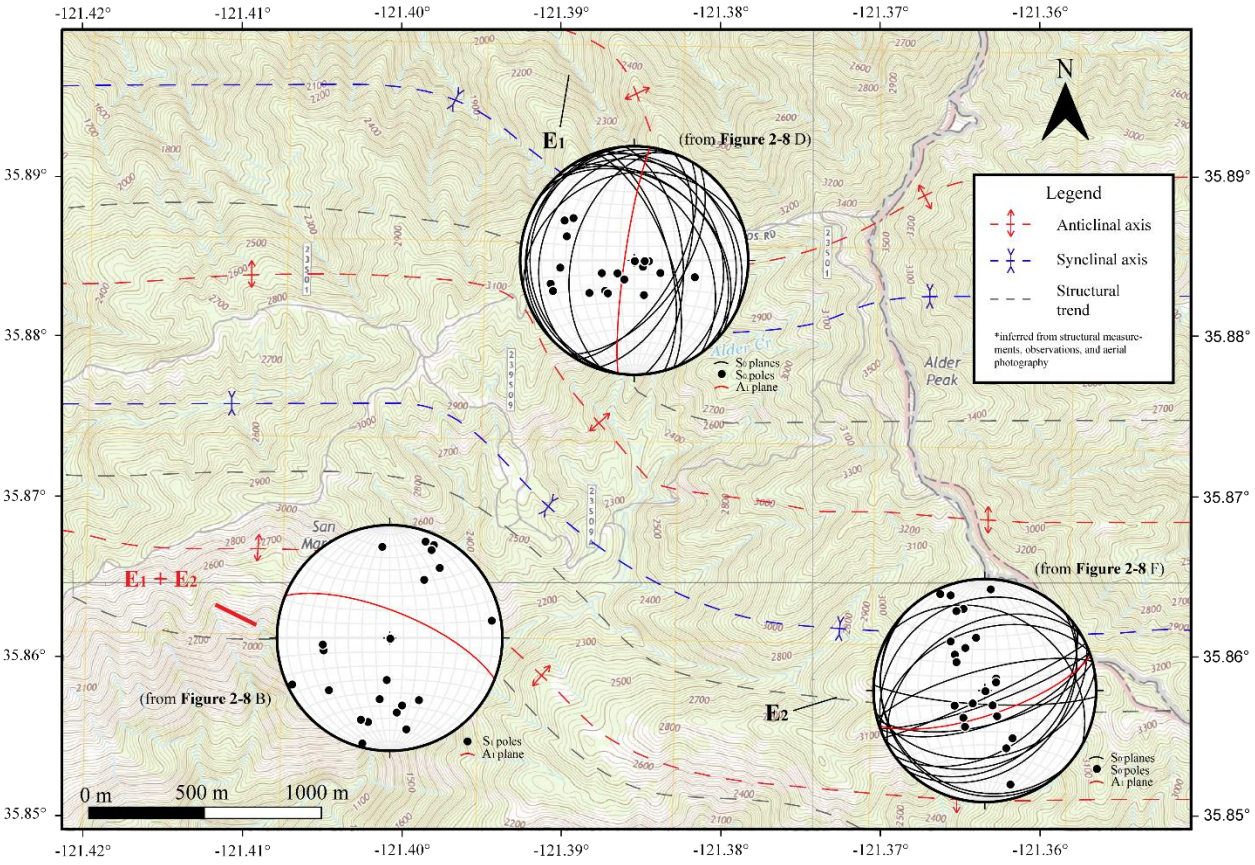

Figure 4-7. *Inferred regional stresses and net stresses due to deformation from Event 1 and Event 2 (E_1 and E_2 respectively).*

This structural analysis shows that the investigated area is marked by a complex tectonic history where most of the bedding was affected by two fold events. The first fold event, E1, is characterized by the formation of folds oriented north-south, likely associated with the main compressive deformation contemporaneous with the regional metamorphism (Ersnt, 1984). The second deformation event, E2, is local and associated with the reorientation of folds and axial plane schistosity along an E-W trend. This schistosity is more closely in line with rotation caused by translation movement along the San Andreas fault system (shown in **Figure 4-8**).

Figure 4-8. *Regional map showing some prominent tectonic features of the U.S. West Coast.* (modified from a figure published by Stoffer, 2006)

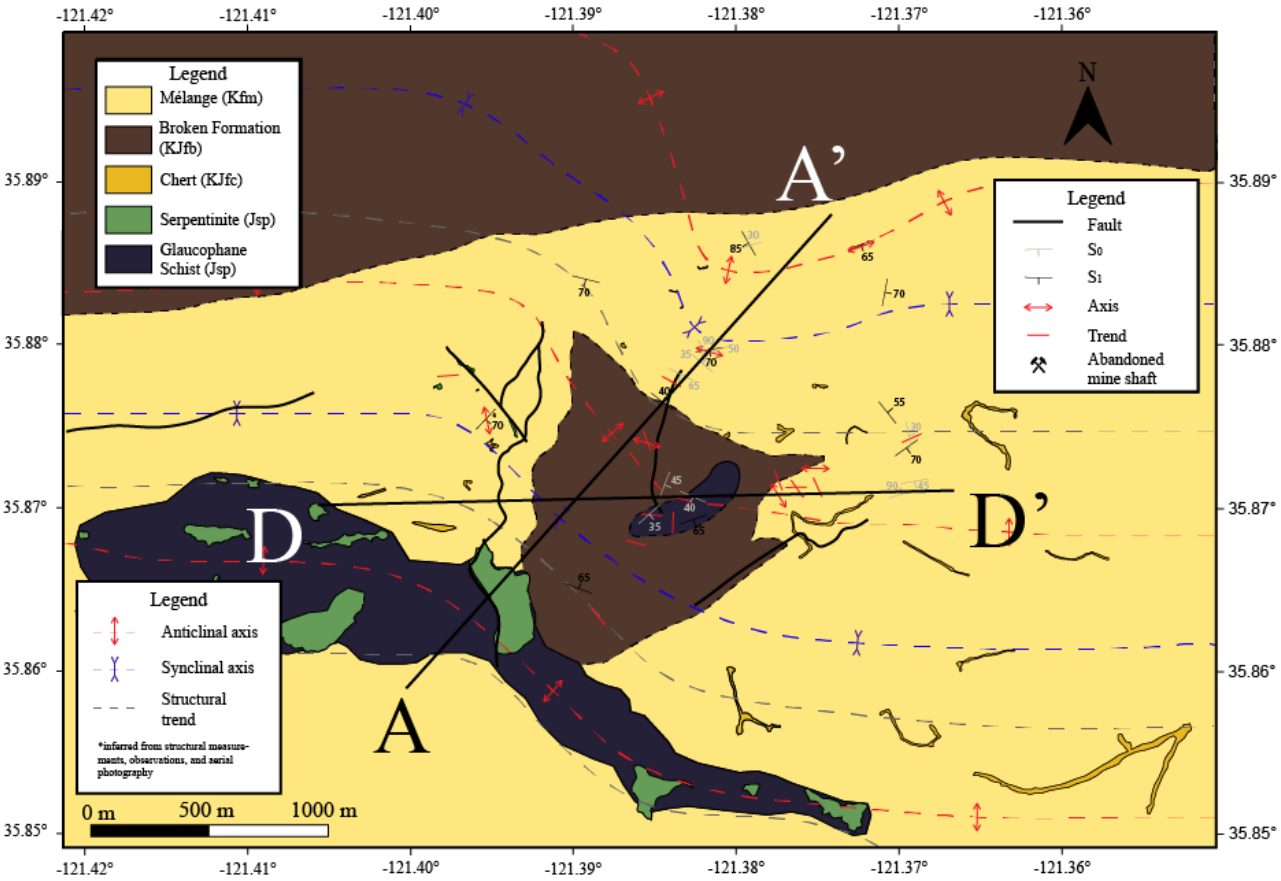

Figure 4-9. *Geologic map of the Alder Creek study area.*

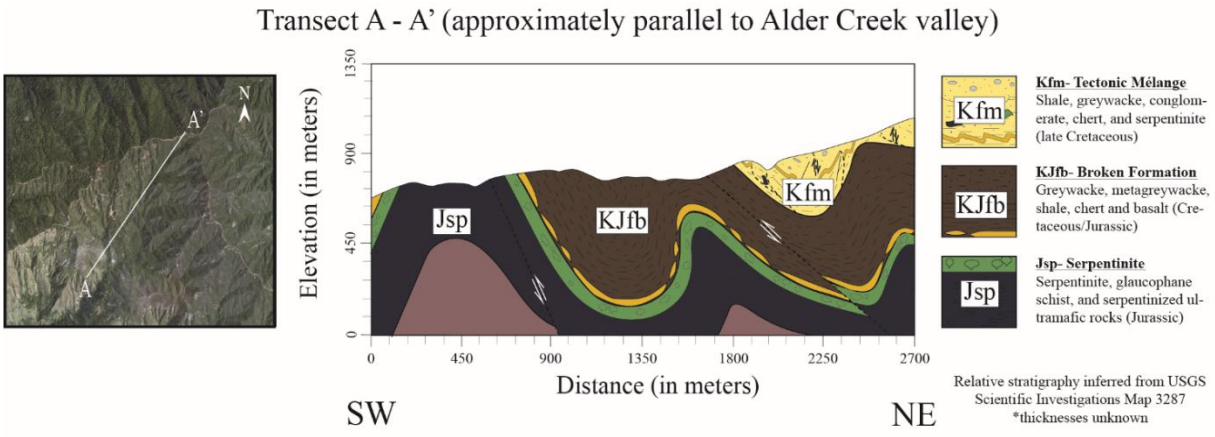

Figure 4-10. *Inferred cross-section parallel to regional structure.*

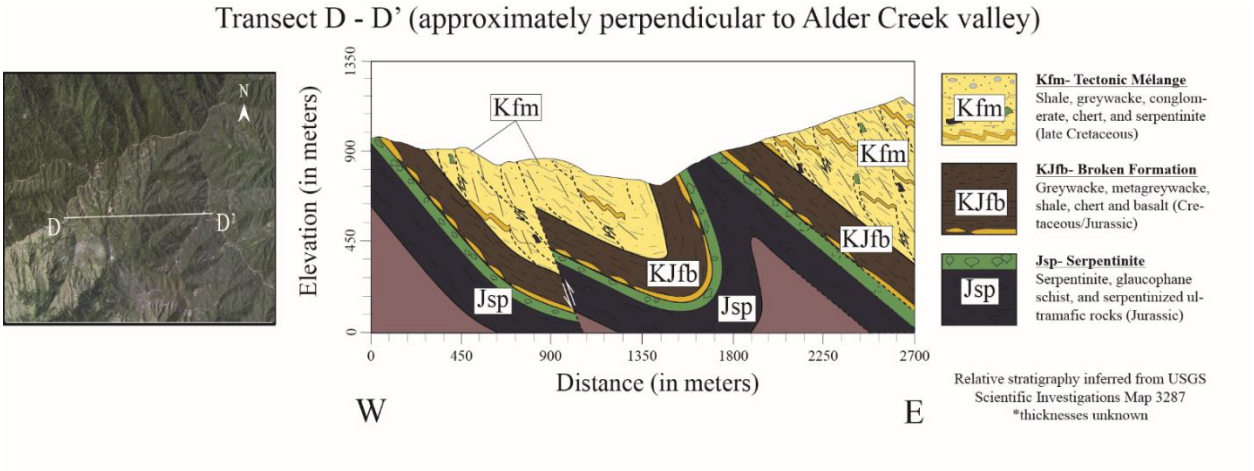

Figure 4-11. *Inferred cross-section perpendicular to regional structure.*

4.3- Bulk-rock mineralogy

A summary table of sample mineralogy using petrographic and XRD analyses is included in **Table 4-1**. The information obtained via XRD analyses, petrography, and hand sample identification were used to categorize the lithology of each sample. These lithologies were compared with the units proposed by Graymer et al (2014). Samples were then categorized into one of three prevailing units (Serpentinite- Jsp, Broken Formation- KJfb, and Melange- Kfm) based on similarity to the lithologic descriptions presented in section **2.3**. Unit classification by sample may be found in **Table 4-2** alongside sample location and lithologic classification.

Sample	Dolomite	Quartz	Albite	Prehnite	Pumpellyite	Illite	Smectite	Kaolinite	Vermiculite	Lizardite	Glaucophane	Augite	Wollastonite	Lawsonite
LB16-01	-	-	-	-	-	-	X	X	X	XXX	-	X	X	-
LB16-02	-	-	-	-	-	-	X	X	-	XXX	-	-	X	-
LB16-03	-	-	-	-	-	-	-	XX	-	-	XXX	X	X	X
LB16-04	-	-	-	-	-	-	-	XX	X	-	XXX	-	-	-
LB16-05	-	-	-	-	X	X	-	XX	-	-	XXX	-	X	-
LB16-07	-	XXX	XX	-	-	X	-	-	X	-	-	-	-	X
LB16-08a	-	XXX	X	-	-	XX	-	-	-	-	-	-	-	XX
LB16-08b	X	-	-	-	XX	-	-	-	-	-	XXX	-	-	X
LB16-08c	-	XXX	-	-	-	X	-	-	XX	X	XX	-	-	X
LB16-09a	-	XXX	XX	-	-	XX	-	-	-	X	-	-	X	-
LB16-09b	-	XXX	X	-	-	XX	-	XX	X	-	-	-	X	X
LB16-11a	-	XXX	-	-	-	-	-	XX	X	X	-	-	-	XX
LB16-11b	-	XXX	XX	-	-	X	-	X	X	X	-	-	-	X
LB16-12	-	XXX	XX	-	-	X	X	XX	-	X	-	-	-	X
LB16-13	-	XXX	-	-	-	-	-	-	-	-	-	-	-	-
LB16-14a	-	XXX	-	-	-	XX	XX	X	X	-	-	-	-	X
LB16-14b	-	XXX	XX	-	-	X	-	X	X	X	-	-	-	X
LB16-14c	-	XXX	X	-	-	-	-	X	-	X	-	-	-	X
LB16-15	-	XXX	XXX	X	-	X	XX	X	X	X	-	-	-	X
LB16-16	-	XX	-	-	-	XX	-	-	X	-	XXX	-	-	X
LB16-17	X	-	-	X	X	-	-	-	X	X	XXX	-	-	XX
LB16-18a	-	XXX	XX	-	-	X	-	XX	-	X	-	-	-	X
LB16-18b	XX	XXX	XX	-	-	X	-	X	X	-	-	-	-	X
LB16-19	XX	XXX	-	-	X	X	XX	XX	X	-	-	-	-	X
LB16-21	XX	XXX	-	-	X	XX	-	-	X	-	-	-	-	-
Lb16-22	-	XXX	XXX	-	-	X	-	X	X	X	-	-	-	X
LB16-23	-	XXX	XXX	-	-	XX	-	-	X	X	-	-	-	X
LB16-24	XX	XXX	-	-	-	-	-	-	-	-	-	-	-	X
LB16-25	-	XXX	XX	-	-	X	-	-	X	-	-	-	-	-
LB16-26	-	XXX	XX	-	-	X	-	XX	X	-	-	-	-	-
LB16-27	-	XX	XXX	X	-	X	XX	XX	X	-	-	-	X	X
LB16-28	-	XXX	X	-	-	X	-	XX	X	-	-	-	-	X
LB16-30	-	XXX	-	-	-	-	X	X	-	XXX	-	X	X	-

Table 4-1. *Summary table of sample mineralogy as concluded from petrography and powdered bulk rock XRD analyses*. The number of Xs indicates relative abundance with one X corresponding to very minor, two Xs corresponding to minor, and three Xs corresponding to major abundances.

Sample	Latitude	Longitude	Lithology	Map unit
LB16-01	35.873	-121.392	Serpentinite	Jsp
LB16-02	35.873	-121.391	Serpentinite	Jsp
LB16-03	35.873	-121.390	Glaucophane schist	Jsp
LB16-04	35.873	-121.390	Mica schist	Kfm
LB16-05	35.878	-121.386	Glaucophane schist	Jsp
LB16-06	35.882	-121.392	Serpentinite	Jsp
LB16-07	35.881	-121.371	Greywacke	Kfm
LB16-08a	35.882	-121.371	Quartz vein	Kfm
LB16-08b	35.882	-121.371	Glaucophane schist	Kfm
LB16-08c	35.882	-121.371	Glaucophane schist	Kfm
LB16-08d	35.882	-121.371	Quartz vein	Kfm
LB16-09a	35.892	-121.375	Sandstone	Kfm
LB16-09b	35.892	-121.375	Shale	Kfm
LB16-09c	35.892	-121.375	Shale	Kfm
LB16-11a	35.883	-121.384	Metagreywacke	KJfb
LB16-11b	35.883	-121.384	Greywacke	Kfm
LB16-12	35.884	-121.384	Greywacke	Kfm
LB16-13	35.886	-121.383	Quartz vein	Kfm
LB16-14a	35.886	-121.382	Metagreywacke	KJfb
LB16-14b	35.886	-121.382	Sandstone	KJfb
LB16-14c	35.886	-121.382	Sandstone	KJfb
LB16-15	35.879	-121.383	Sandstone	KJfb
LB16-16	35.879	-121.381	Glaucophane schist	Jsp
LB16-17	35.881	-121.381	Glaucophane schist	Jsp
LB16-18a	35.881	-121.381	Siltstone	KJfb
LB16-18b	35.881	-121.381	Metagreywacke	KJfb
LB16-19	35.880	-121.378	Graphititc metagreywacke	KJfb
LB16-21	35.880	-121.377	Graphitic slate	Kfm
LB16-22	35.881	-121.376	Sandstone	KJfb
LB16-23	35.881	-121.376	Sandstone	KJfb
LB16-24	35.880	-121.378	Graphitic slate	Kfm
LB16-25a	35.883	-121.384	Graphitic slate	KJfb
LB16-25b	35.883	-121.384	Metagreywacke	KJfb
LB16-25c	35.883	-121.384	Metagreywacke	KJfb
LB16-25d	35.883	-121.384	Sandstone	Kfm
LB16-25e	35.883	-121.384	Sandstone	Kfm
LB16-26	35.884	-121.384	Greywacke	Kfm
LB16-27	35.885	-121.384	Greywacke	Kfm
LB16-28	35.876	-121.389	Metagreywacke	KJfb
LB16-29	35.885	-121.397	Graphitic slate	Kfm
LB16-30	35.884	-121.397	Serpentinite	Jsp

Table 4-2. *Sample location, lithology, and identified map unit.* Sample locations given in decimal degrees.

Jsp sample mineralogy is shown in **Table 4-**1. These samples are dominantly constituted by glaucophane along with minor (less than 5% modal composition) augite and wollastonite. Kaolinite ranges from low to moderate (greater than 5%, but less than 25%) abundance within the Jsp samples except in samples LB16-07, LB16-16, and LB16-17 where minor amounts of vermiculite are present instead. Jsp samples were found to be quartz-poor with the exception of LB16-16, which shows the presence of quartz in a notable amount. Samples LB16-01, LB16-02, and LB16-03 record high intensity lizardite peaks, confirming hand sample and field observations of high-degree serpentinization at these localities. Notable accessory phases identified through bulk-rock XRD analyses of Jsp samples include: spinel, magnetite, chromite, franklinite, ilmenite, marcasite, pyrrhotite, and enargite.

Serpentinite (Jsp) is interpreted to be a Jurassic-age member of the Coast Range ophiolite sequence (Graymer et al., 2014). The presence of pyroxenes and pyroxenoids such as augite and wollastonite within Jsp samples further reinforces the mafic/ultramafic interpretation of this unit. Relict two-pyroxene assemblages, dominantly augite and enstatite, are observed in Jsp thin sections, though in low modal abundances generally below 5% (**Table 4-1**). Samples LB16-16 and LB16-17 lack these distinct phases. LB16-16 and LB16-17 differ mineralogically from other Jsp samples as evidenced by a moderate abundance of quartz and illite in LB16-16 and the presence of dolomite in LB16-17. However, lithologic similarity in hand sample and thin section coupled with field observations appear to support the structural repetition of unit Jsp within the area.

Samples from units KJfb and Kfm (see **Table 4-1**) are both predominantly comprised of shale and greywacke members with varying amounts of lithologic and structural variation, as discussed in Chapter 2.3. The heterogeneity inherent to both KJfb and Kfm complicates the

observation of distinct mineralogical patterns in these bulk-rock XRD data. However, samples from both units exhibit high proportions of quartz and moderate to high proportions of albite. Dolomite is observed in moderate to minor abundance within five of these samples. Illite and kaolinite are the most abundant and prolific clay minerals, whereas vermiculite is present in minor amounts in most KJfb and Kfm samples. Smectite is largely absent in these samples apart from KJfb samples LB16-14a, LB16-15, and LB16-19 and Kfm samples LB16-12 and LB16-27 where it is estimated to occur in moderate modal abundances (estimated between 15% and 25% modal abundance based on petrographic observation and relative XRD peak intensity).

XRD analyses indicate minor amounts of lizardite in KJfb samples: LB16-11a, LB16-14b, LB16-14c, LB16-15, LB16-18a, LB16-22, and LB16-23 and Kfm samples: LB16-08c, LB16-09a, LB16-11b, and LB16-12. The presence of lizardite may reflect some degree of hydrothermal alteration of olivine and/or pyroxene, tectonic reworking of underlying Jsp containing primary lizardite, or some combination thereof. As mentioned earlier, glaucophane is observed in Kfm samples LB16-04, LB16-08b, and LB16-08c, where it is present in moderate to high abundance (as evidenced by estimated modal abundances). Minor amounts of wollastonite are also observed in KJfb samples LB16-11a and LB16-11b, as well as Kfm sample LB16-27. The appearance of these mafic and other related phases appears to be an exception; glaucophane, augite, and wollastonite are absent from the majority of KJfb and Kfm samples.

Lawsonite was observed in minor to moderate abundance in samples across all three units, although it was only present in Jsp samples LB16-16 and LB16-17. Trace amounts of montmorillonite, along with various phyllosilicates—particularly paragonite, phlogopite, chamosite, pyrophyllite, glauconite, and chloritoid—are ubiquitous. Also of note is the presence

of trace amounts of sulfides such as pyrite, arsenopyrite, and in some cases chalcopyrite in all samples.

4.4- Clay fraction and illite crystallinity

Results from the clay slide-mount procedure (after Goldstein and Reynolds, 1994) are presented in **Table 4-2**. Illite crystallinity values are reported in terms of Δ°2θ.

Sample	Untreated	Treated
LB16-07	0.175	0.259
LB16-09a	0.214	0.279
LB16-09b	0.359	0.291
LB16-11b	0.241	0.183
LB16-14b	0.167	0.186
LB16-14c	0.240	0.191
LB16-15	0.127	0.133
LB16-16	0.169	0.097
LB16-18a	0.271	0.233
LB16-18b	0.235	0.204
LB16-19	0.270	0.266
LB16-21	0.374	0.255
LB16-22	0.263	0.138
LB16-23	0.201	0.247
LB16-25	0.297	0.307
LB16-27	0.234	0.296

Table 4-3. *Illite crystallinity values for both the untreated and ethylene glycol treated clay slides.* Values reported in Δ°2θ.

The untreated clay fraction samples are ranging from 0.359 Δ°2θ to 0.127 Δ°2θ. The average value for untreated samples was approximately 0.240 Δ°2θ. The ethylene glycol treated clay fraction displays a range of 0.210 Δ°2θ from a maximum of 0.307 Δ°2θ to a minimum value

of 0.097 Δ°2θ. The average value for the treated samples was approximately 0.223 Δ°2θ. Based on the illite crystallinity values reported in **Table 4-2,** samples range from low anchizone to high anchizone (using the classification chart presented in **Figure 4-12**) with average values for both treated and untreated samples firmly within the High Anchizone.

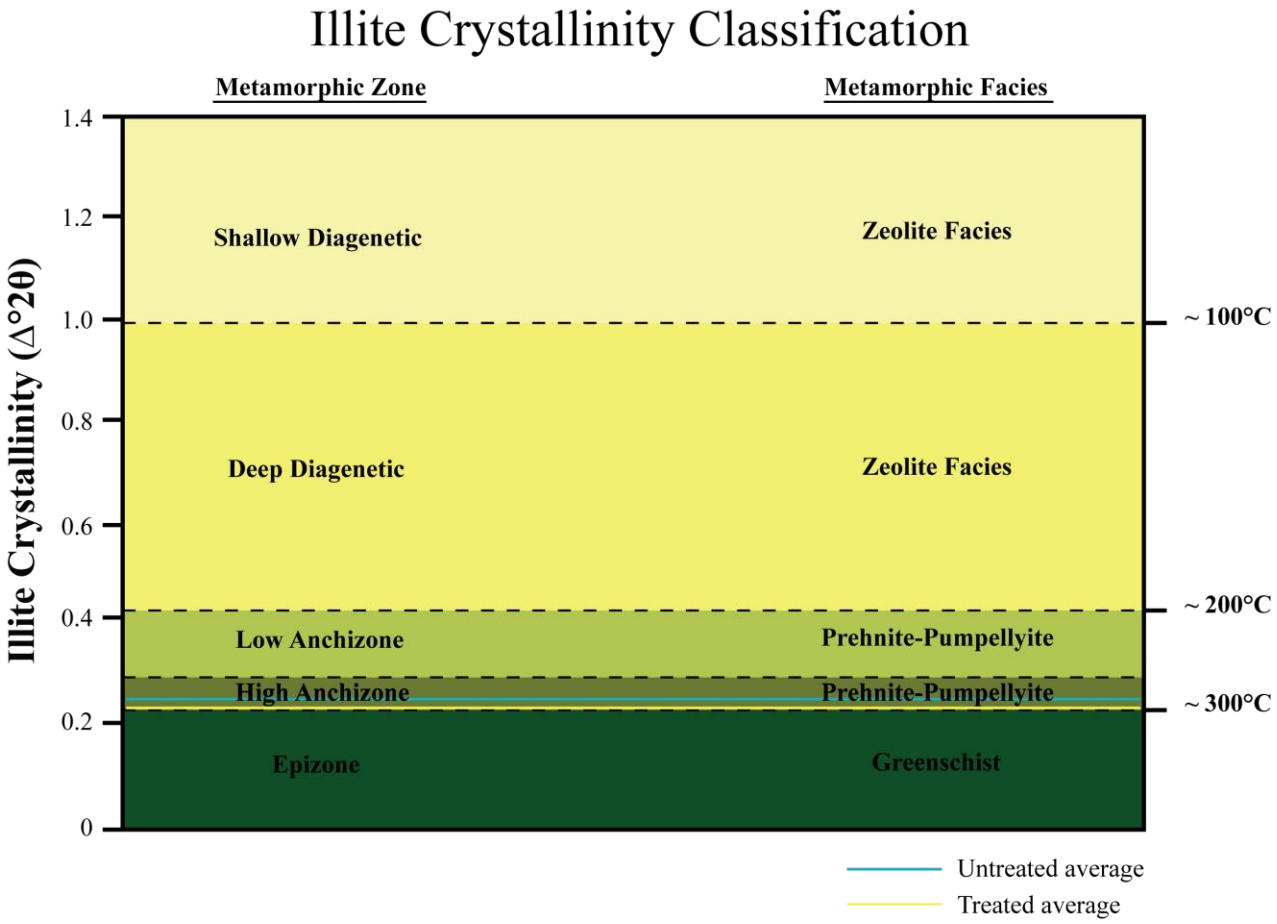

Figure 4-12. *Reference figure comparing illite crystallinity to approximate metamorphic facies and temperature*. Modified from Verdel et al. (2012).

4.5- Fluid inclusion microthermometry

4.5.1- Microthermometry

Fluid inclusion microthermometry was carried out on quartz-vein hosted fluid inclusion assemblages from three samples discussed previously: LB16-08a, LB16-21, and LB16-24. These

samples contained fluid inclusions hosted within quartz veins. Sample location with respect to mine galleries for each of these three samples is shown in **Figure 4-3**. Reference figures for each sample are included (see **Figure 4-13**, **Figure 4-17**, and **Figure 4-20** respectively) and detail the location of each fluid inclusion zone, though results will be presented by sample rather than zone.

In the context of this study a 'zone' refers to the distinct area of each sample containing fluid inclusion assemblages of interest (see the corresponding numbered insets on **Figure 4-13**, **Figure 4-17**, and **Figure 4-20**). The letters within each inset correspond to an individual fluid inclusion while the lines represent the approximate center and orientation of a given fluid inclusion array. Attention may be called to specific zones where appropriate to illustrate the larger picture as presented by the data. Specific information, such as the vapor/liquid ratio, salinity, T_h, T_m, and calculated concentration of gas phases (where applicable) may be found in Appendix B in **Tables B-1** through **B-4.** A summary table of calculated salinity and T_h (along with the standard error for each) by zone is provided in **Table B-5**.

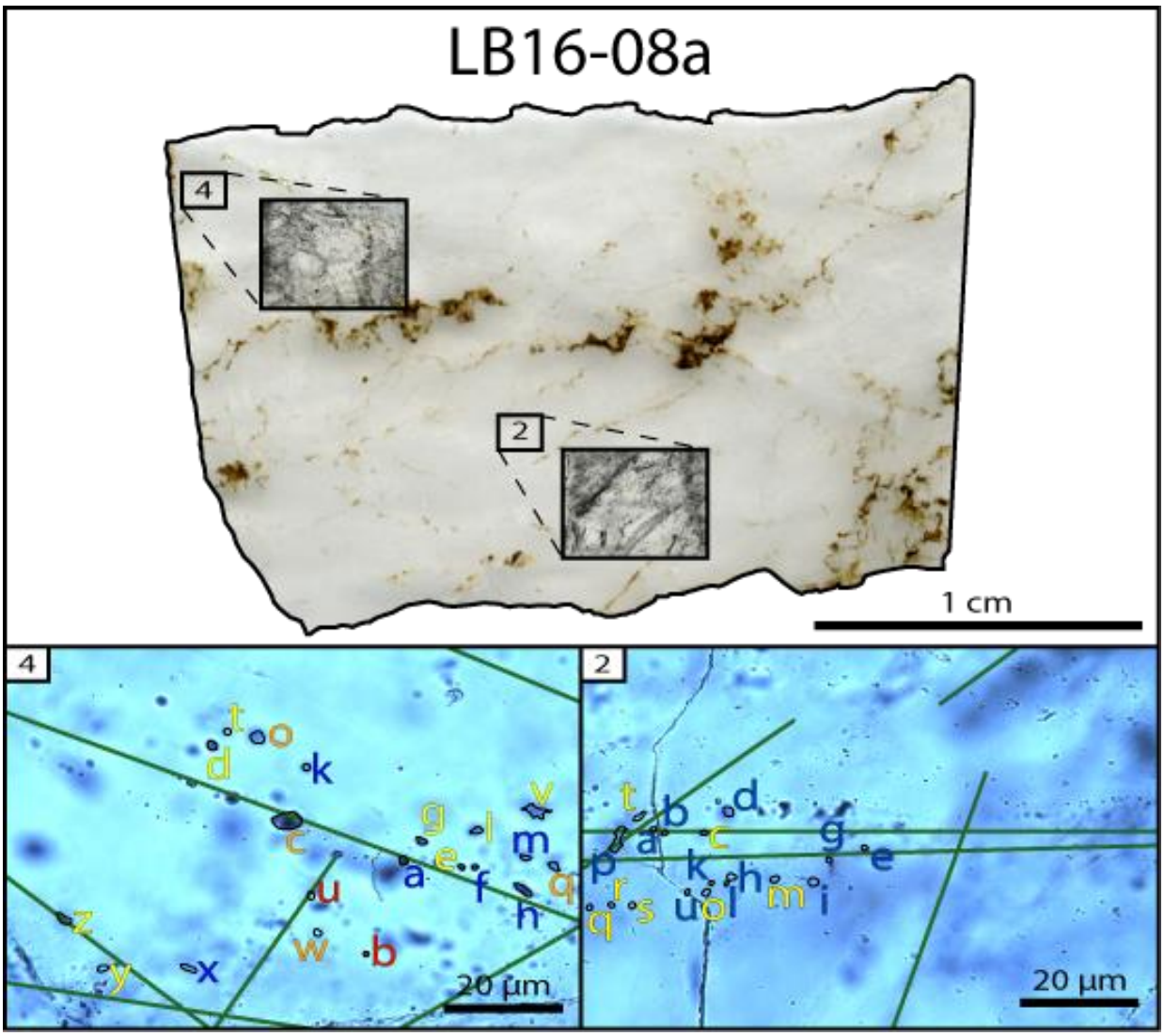

Figure 4-13. *Location and spatial arrangements of FIAs within zones 2 and 4 (insets 2 and 4, respectively) of sample LB16-08a.*

LB16-08a fluid inclusions were observed to be dominantly two-phase, liquid-vapor fluid inclusions. Thirty-eight total fluid inclusions were analyzed from eight distinct FIAs within the sample. FIAs ranged from intragranular (i.e. observed to cross-cut grain boundaries) to wholly-intergranular (contained within well-defined grain boundaries). Vapor volume percentages were estimated (after Taberner et al., 2012) for LB16-08a fluid inclusions. The volume percentage of vapor was found to range between 5 and 15% of total fluid inclusion volume. One inclusion from

this sample demonstrated a vapor volume percentage of approximately 50%, however. Tables containing vapor volume percentage and additional qualities such as T_m and T_h are provided in **Table B-1** through **Table B-4**.

Many FIAs within LB16-08a are observed to be roughly parallel with one another (see **Figure 4-14**). **Figure 4-14** also demonstrates inclusions with trails spanning from intragranular (consistent across grain boundaries) to intragranular without terminating at grain boundaries. Many of these FIAs are aligned along microfracture patterns, suggesting a secondary origin. Furthermore, there appear to be multiple sets of secondary fluid inclusions as inferred by the intersection of microfracture sets. Intersection angles between these inclusion trails vary from ~30° to ~45°.

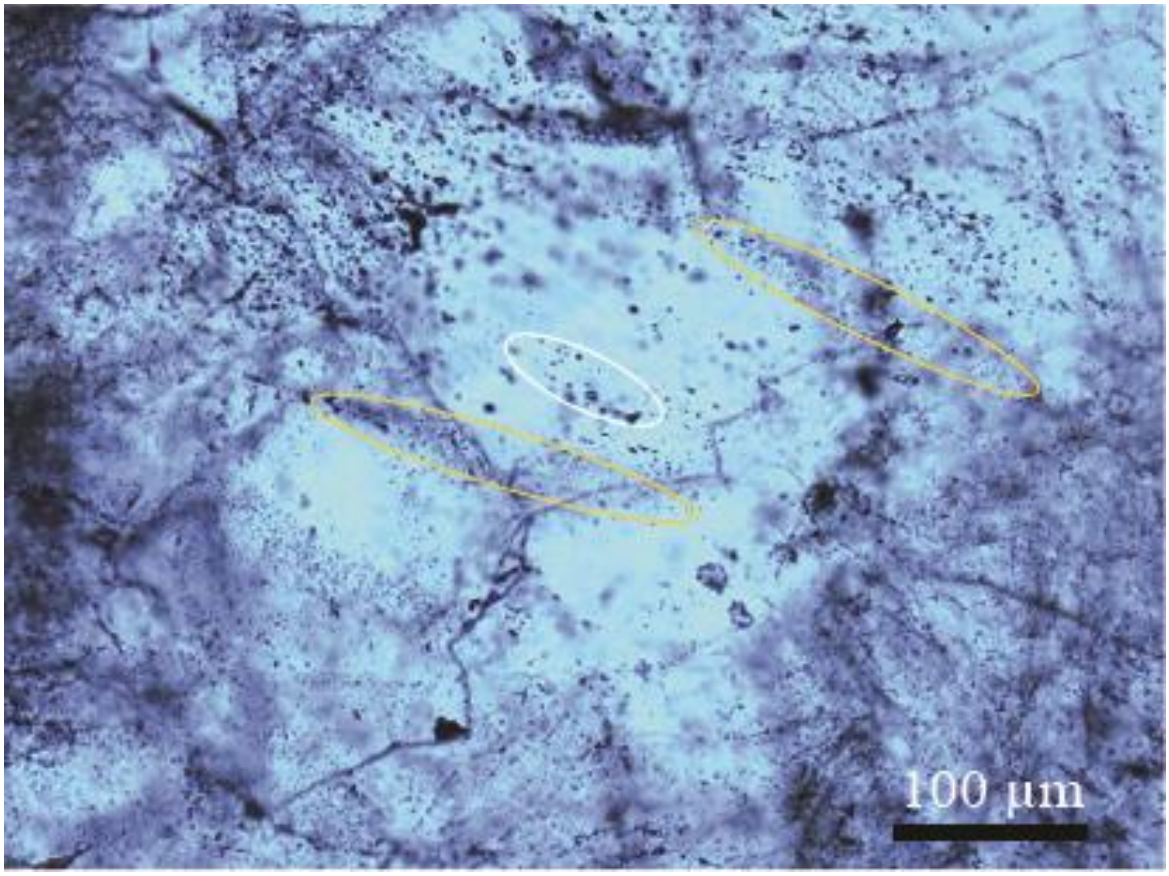

Figure 4-14. *Representative photomicrograph of LB16-08a FIAs showing both intragranular FIAs (in orange) and intergranular FIAs (in white).*

Zone 4 may also record the presence of two primary fluid inclusions, i.e. inclusions that occur parallel to crystal growth or not associated with any other nearby FIAs. These two inclusions record homogenization temperatures significantly greater than other LB16-08a inclusions and, in fact, give the highest T_h temperatures (> 280°C) in this study. This represents a ~50°C increase from the next highest T_h recorded for sample LB16-08a (see **Table B-1**). **Figure 4-15** and **Figure 4-16** provide further insight into homogenization temperature distribution and calculated salinity for LB16-08a fluid inclusions.

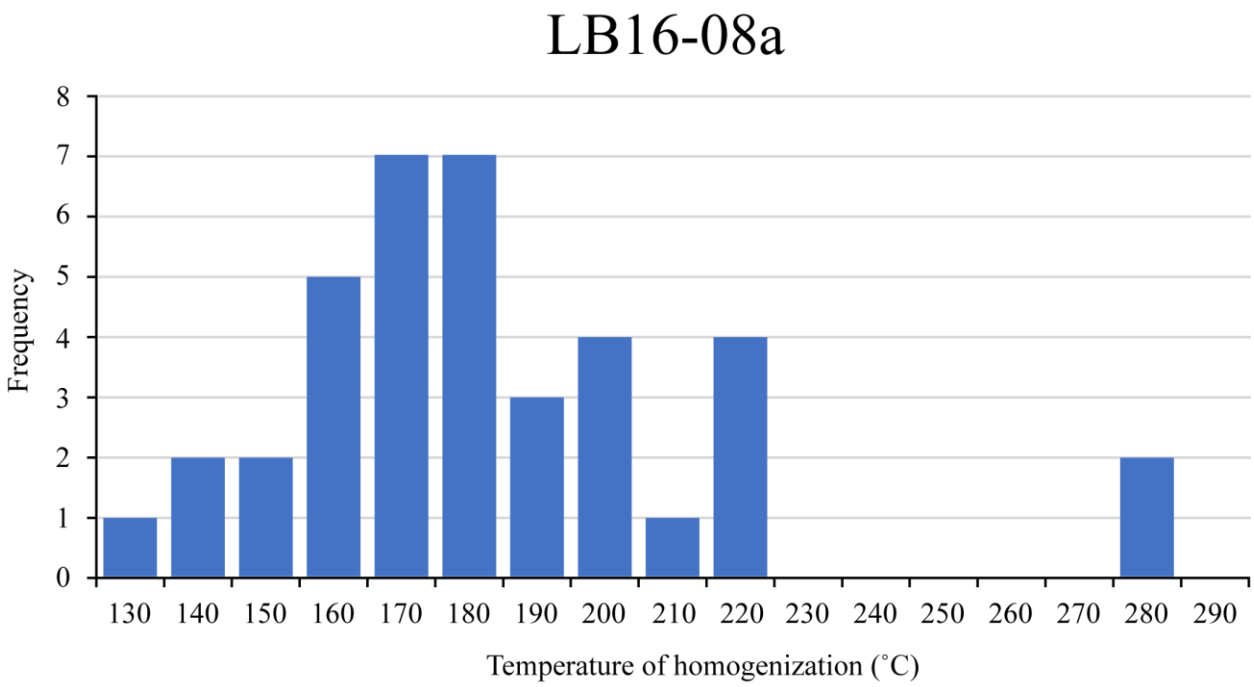

Figure 4-15. *Histogram of all LB16-08a fluid inclusion homogenization temperatures.*

LB16-08a fluid inclusions cover a wide T_h range from 135°C to 285.6°C. Most of the inclusions (14 out of 38) yield T_h values of 170°C to 180°C (**Figure 4-15**). Zone 2 fluid inclusions are more tightly clustered within a T_h range from 135°C to 210°C (**Figure 4-16)**.

Additionally, salinity values of inclusions within zone 2 are narrowly distributed (+/- 0.5 wt% NaCl equivalent) around an average salinity of 2.1 wt% NaCl equivalent (see **Figure 4-16**).

In zone 4 T_h ranges from 145°C to 285.6°C (**Figure 4-16**), though as noted previously there is a large T_h gap between the inferred secondary and primary inclusions. Salinity also displays a large degree of variance between 3.06 wt% NaCl equivalent and 7.97 wt% NaCl equivalent. This range of salinity is due in large part to one significant outlier (**Figure 4-16**). Removal of this outlier results in an average salinity of 3.69 wt% NaCl equivalent, though zone 4 still demonstrates a higher average salinity (~1.5 wt% NaCl difference) and greater salinity variability than the other, secondary inclusions of zone 2.

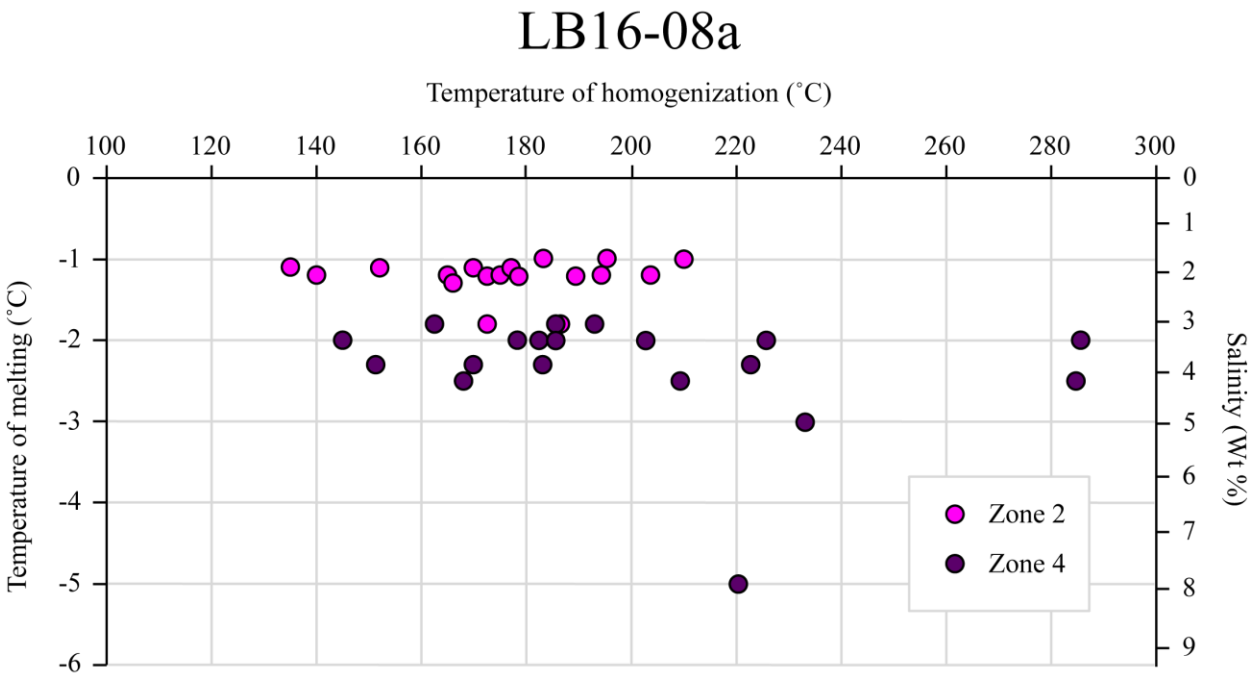

Figure 4-16. *Scatterplot comparing LB16-08a fluid inclusion homogenization temperatures to melting temperature and calculated salinity.* Salinity wt% calculated after Bodnar (1993).

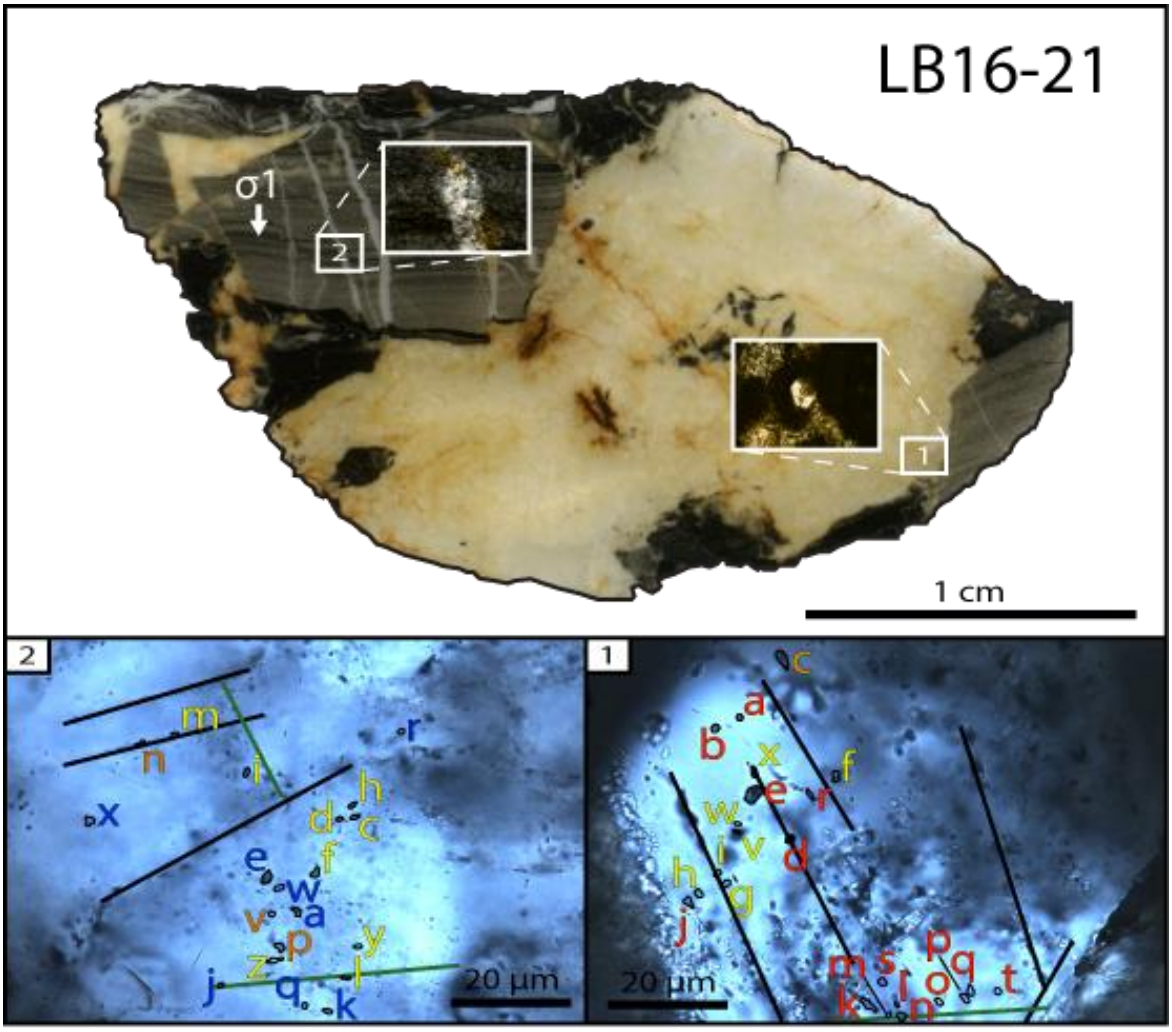

Figure 4-17. *Location and spatial arrangements of FIAs within zones 1 and 2 (insets 1 and 2 respectively) of sample LB16-21.*

Fluid inclusions in sample LB16-21. FIAs (insets 1 and 2 of **Figure 4-17,** respectively) are dominantly two-phase, liquid-vapor fluid inclusions. However, CO_2 vapor-only inclusions were also noted, though in low abundance. Estimated vapor volume percentage for LB16-21 fluid inclusions range between 10 and 30% of total fluid inclusion volume.

Intragranular FIA trails predominate, as all recorded FIAs are contained entirely within grain boundaries. They are inferred to be almost entirely primary judging by orientations that directly parallel observed grain boundaries. Inclusion assemblages which transected grain

boundaries were also noted within the sample. These inclusions were determined to be secondary in nature since they were observed to be perpendicular to the principal growth direction. **Figure 4-18 and Figure 4-19** provide further insight into T_h distribution and calculated salinities between zones 1 and 2.

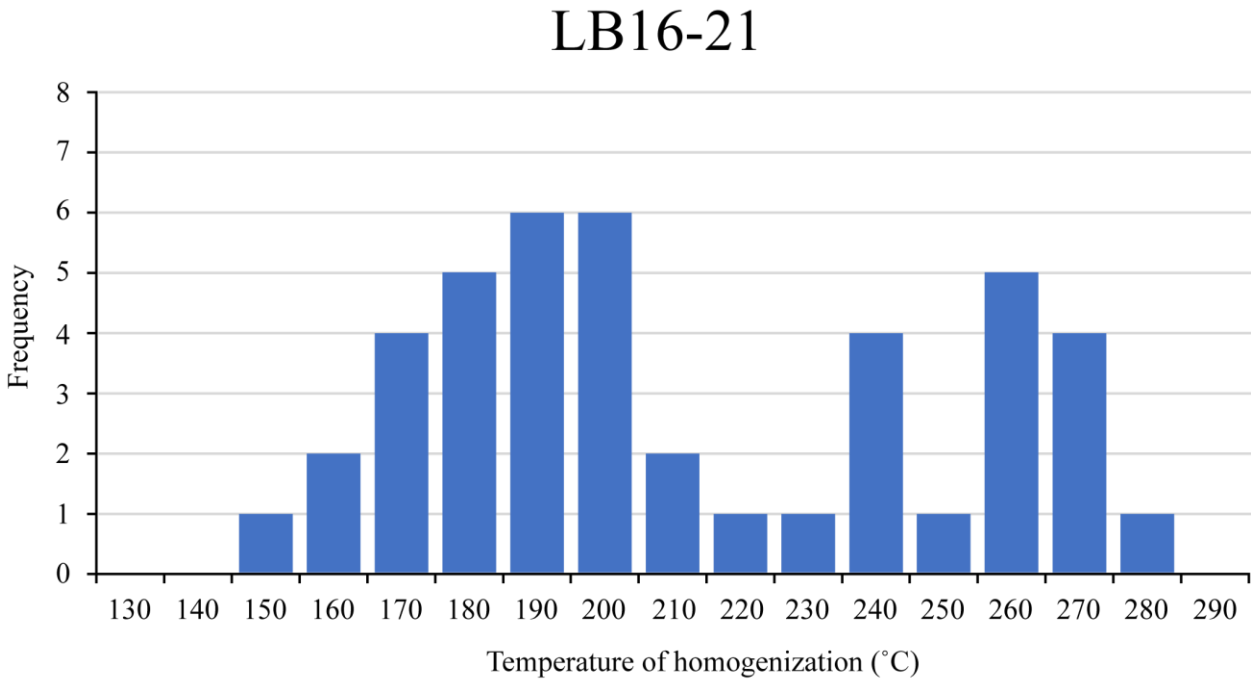

Figure 4-18. *Histogram of all LB16-21 fluid inclusion homogenization temperatures.*

LB16-21 fluid inclusions display a bimodal distribution with T_h peaks at 190 - 210°C and 260 - 280°C (**Figure 4-18**). Also of note is a small cluster of fluid inclusions with T_h between 240°C and 250°C. T_h for all LB16-21 inclusions range between 135°C and 285°C. Salinity values have a narrow distribution around an average salinity of 2.13 wt% (**Figure 4-19**). This average excludes inclusions containing an appreciable amount of CO_2 clathrate inferred via T_m measurements. The presence of these clathrates obscured T_m measurements, distorting salinity calculations (to values up to -15.30 wt% NaCl equivalent). Removal of clathrates for salinity

calculations resulted in a maximum calculated value of 5.41 wt% NaCl equivalent and a minimum of 0.70 wt% NaCl equivalent.

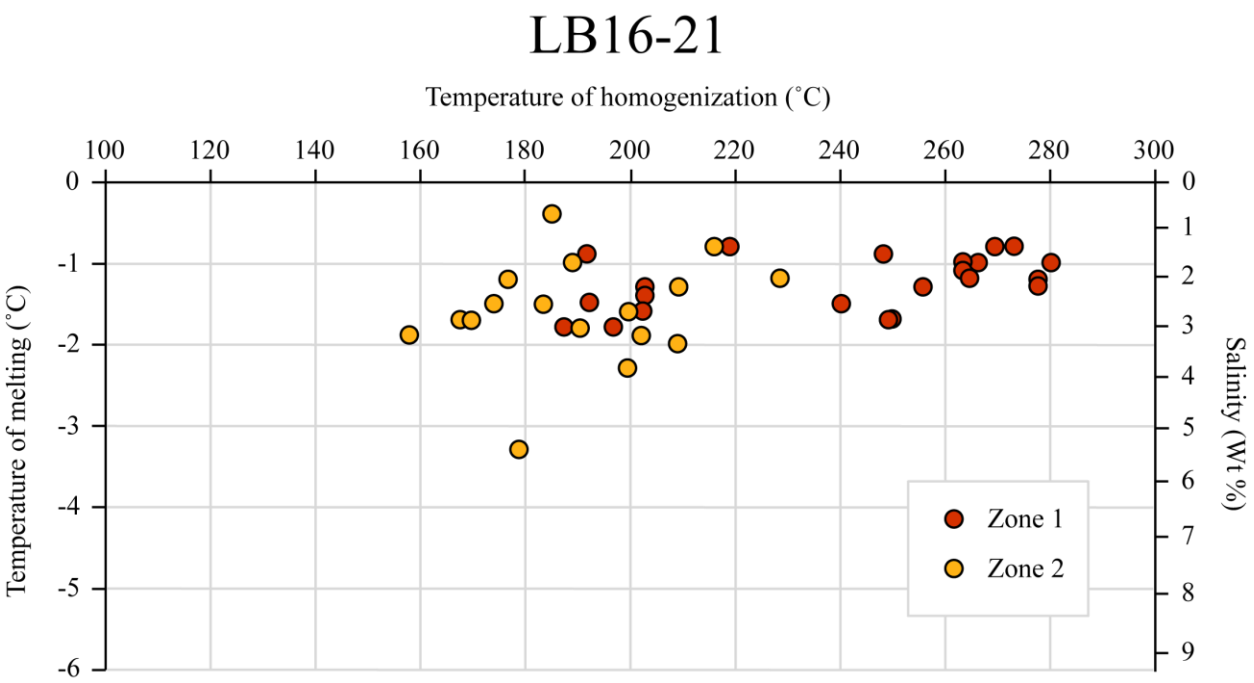

Figure 4-19. *Scatterplot comparing LB16-21 fluid inclusion homogenization temperatures to melting temperature and calculated salinity.* Salinity wt% calculated after Bodnar (1993).

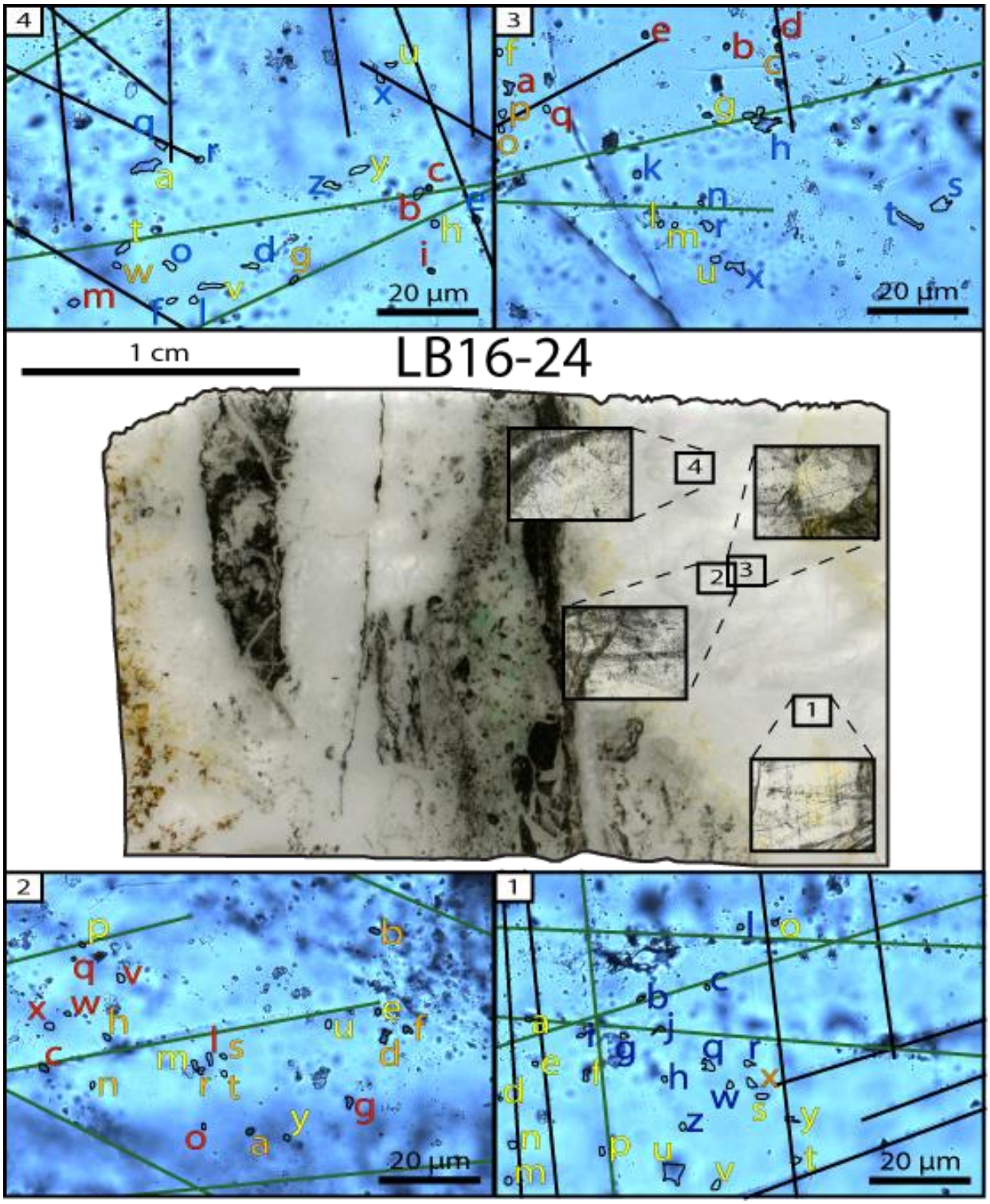

Figure 4-20. *Location and spatial arrangements of FIAs within zones 1, 2, 3, and 4 (insets 1 through 4 respectively) of sample LB16-24.*

LB16-24 fluid inclusions were observed to be dominantly two-phase, liquid-vapor fluid inclusions. Eighty-nine total fluid inclusions were analyzed from 15 distinct FIAs within the sample. Estimated vapor volume percentage for LB16-24 fluid inclusions range between 5 and 25% of total fluid inclusion volume.

LB16-24 fluid inclusions cover a T_h range from 162.5°C to 265.5°C (**Figure 4-21**). T_h displays a distribution which is somewhat bimodal. The 170 - 190°C range accounts for the highest abundance of observed fluid inclusions. Another cluster of inclusions is observed within the narrow range of 220 - 230°C. Lastly, there is a slight increase in the number of inclusions beginning around 240°C before declining near 260°C.

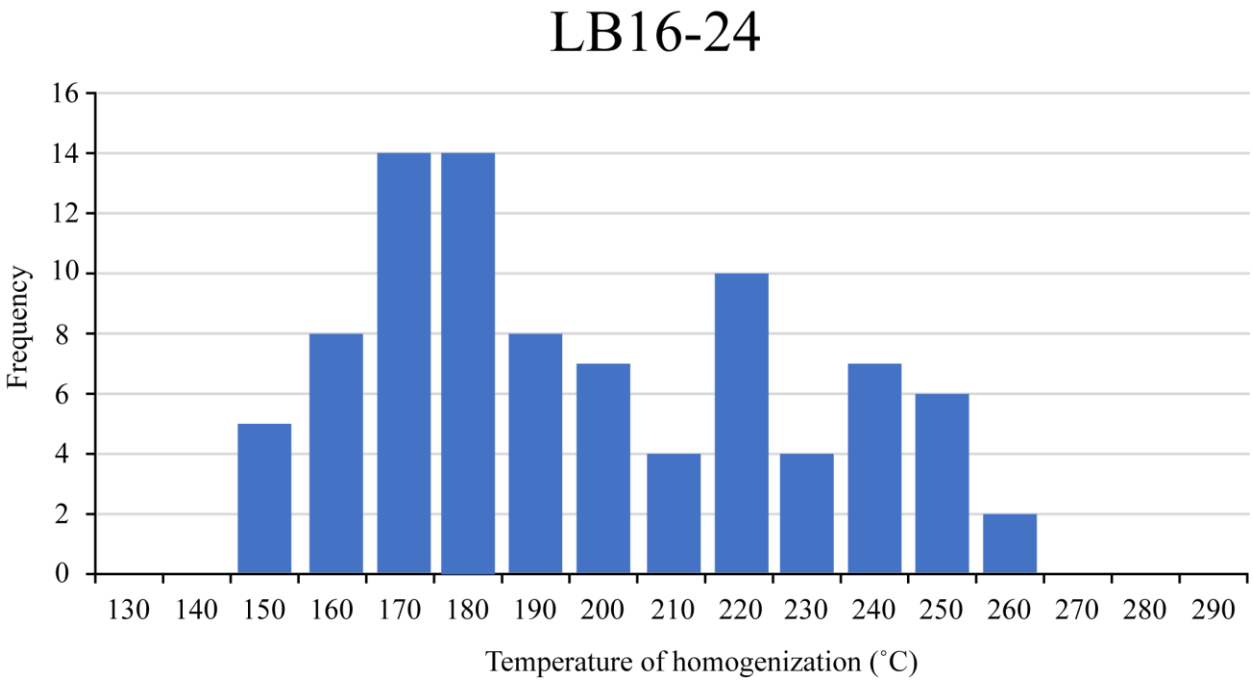

Figure 4-21. *Histogram of all LB16-24 fluid inclusion homogenization temperatures.*

The four FIA zones analyzed for sample LB16-24 contain a mixture of both primary and secondary inclusions as inferred from orientation with respect to principal crystal growth and

microfracture patterns. Within LB1-24, zones 2 and 3 record a higher proportion of primary inclusions, while zones 1 and 4 contain more secondary inclusions. T_h varies from 153.1°C to 265.5°C (**Figure 4-22**). This temperature range is consistent across all samples with the exception of zone 1, where the temperature range is restricted about 160°C to 225°C. Salinity values are also consistent with an average of 2.92 wt% NaCl equivalent, though exhibit a wide range from 0 to 4.96 wt% NaCl equivalent. Again, like in LB16-08a the presence of clathrates inferred from T_m measurements within zone 1 led to six outliers that yielded unrealistic calculated salinity values (-49.5 wt% NaCl equivalent) which were excluded. FIAs within LB16-24 zones 1 and 2 (and to a lesser degree, some within zones 3 and 4) follow two trends that intersect at a near constant angle of 40°, similar to the relationship displayed in both zones 2 and 4 from LB16-08a.

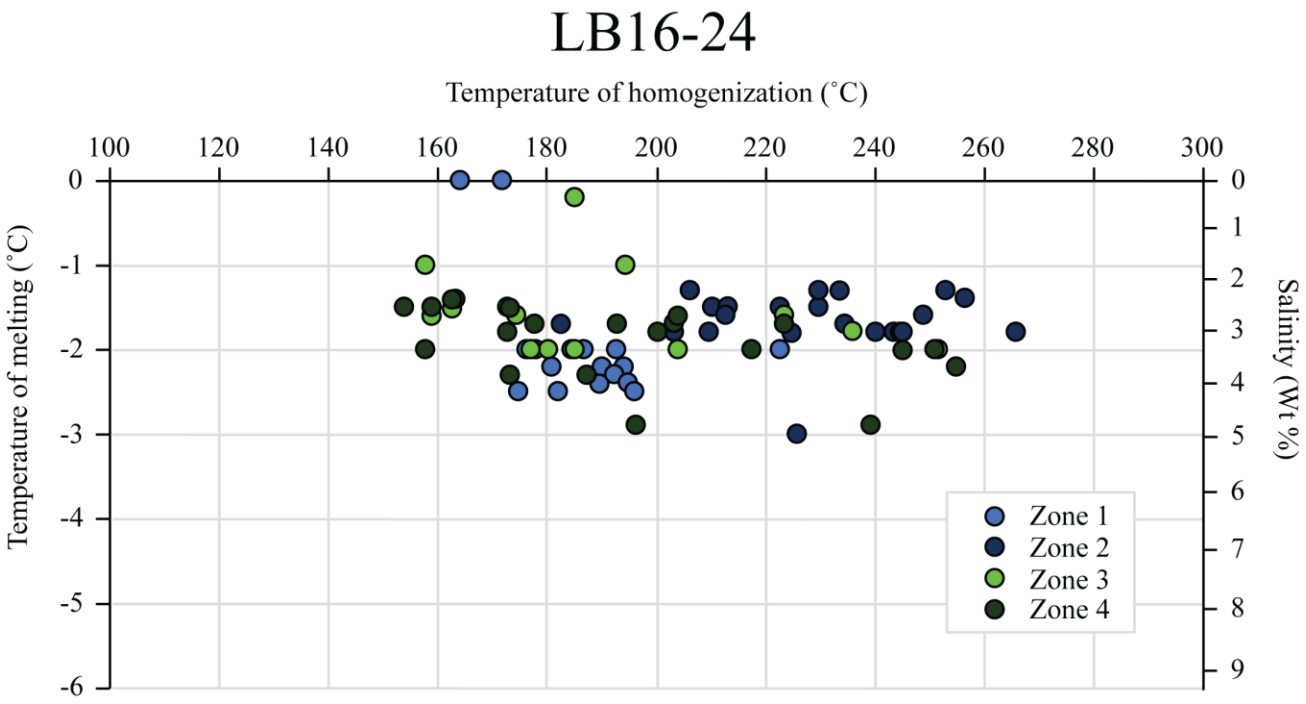

Figure 4-22. *Scatterplot comparing LB16-24 fluid inclusion homogenization temperatures to melting temperature and calculated salinity.* Salinity wt% calculated after Bodnar (1993).

4.5.2- Raman characterization of gases in fluid inclusion assemblages

Fluid inclusions were analyzed using Raman microscopy to aid in the identification and quantification of gaseous phases present within the vapor bubble. A total of 52 $CH_4 \pm CO_2$-bearing inclusions was identified. Example spectra from characteristic inclusions highlighting the presence of CO_2 and CH_4 are shown in **Figure 4-23** and **Figure 4-24,** respectively. The data derived from the collection of Raman spectra are presented in **Table 4-3**. For a complete list of fluid inclusion liquid and vapor phase composition please see **Table B-1** through **B-4**. Only two inclusions from the entirety of LB16-08a inclusions were found to contain appreciable amounts of CH_4, while CO_2 was conspicuously absent from any LB16-08a inclusions. An effort has been made to approximate CH_4 gas concentration using the method of Guillaume (2003).

LB16-21 zone 1 presented H_2O-CH_4 inclusions as well as the most H_2O-CH_4-CO_2 inclusions recorded within a single zone (7 total). H_2O-CH_4-CO_2 inclusions within this zone were linked with the highest homogenization temperatures, spanning a range from 218°C to 280°C with all but one above 248°C.

LB16-21 zone 2 is dominated by CH_4-bearing inclusions, with the presence of only one pure CH_4 inclusion noted. CH_4-bearing inclusions are associated with previously identified primary inclusions. Homogenization temperatures for the CH_4-bearing inclusions display no differences in T_h or T_{mi} from other inclusions within the zone.

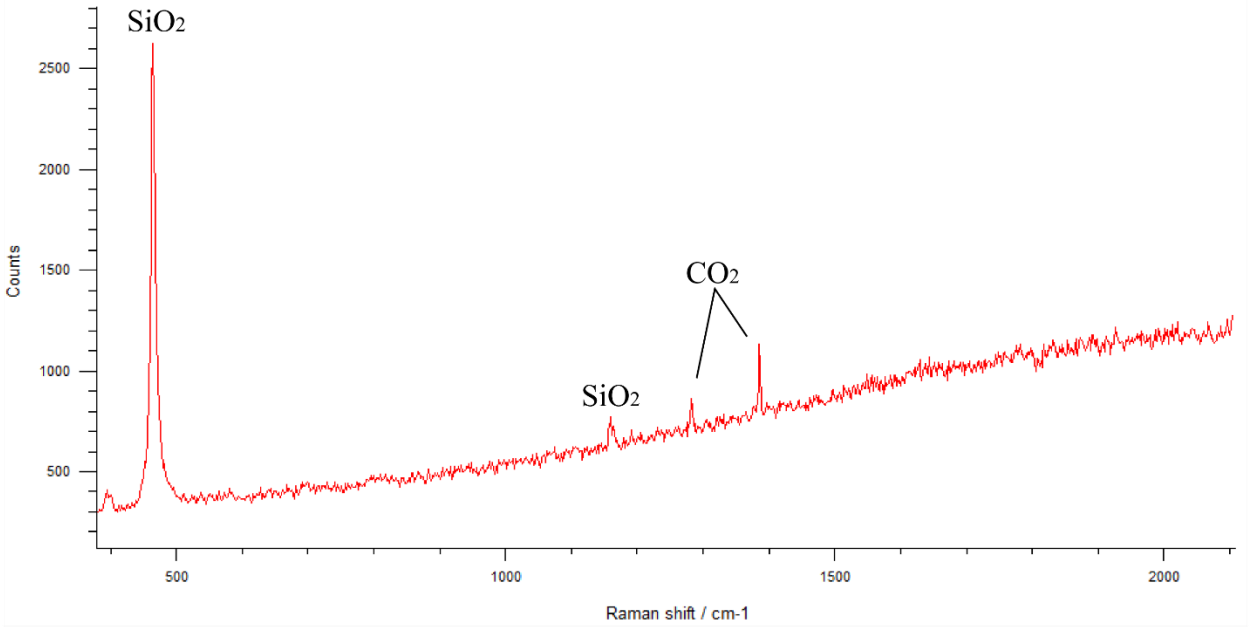

Figure 4-23. *Example spectra showing the presence of CO_2 within LB16-21 zone 1.*

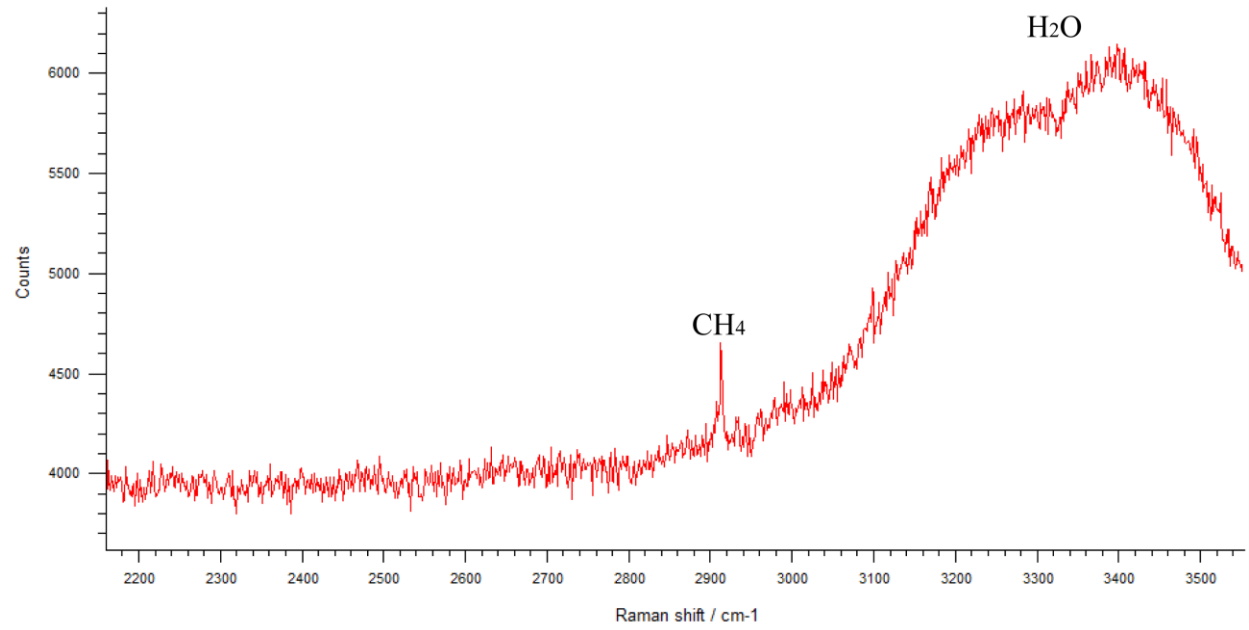

Figure 4-24. *Example spectra showing the presence of CH_4 within LB16-24 zone 4.*

LB16-24 zones contain CH_4, CO_2, and H_2O-CH_4-CO_2-bearing inclusions. CH_4 inclusions are observed within both primary and secondary FIAs. Complex FIA and microfracture set geometries make assessment of spatial relationships between CH_4 and CH_4-CO_2-bearing

inclusions difficult, but across all four zones CH_4-CO_2 inclusions appear to be primary in origin (see **Figure B-18**). Homogenization temperatures for CH_4-CO_2 inclusions range from 194°C to 251°C with no significant T_h difference for CH_4 inclusions as compared to non-CH_4 ± CO_2-bearing inclusions.

4.6- Raman spectroscopy on carbonaceous material

Spectra were collected from 12 samples with greater than 30% modal carbonaceous material from within the Alder Creek study area (orange dots in **Figure 4-3** and **Figure 5-6**). Average temperature calculated via the RSCM geothermometer developed by Lahfid et al. (2010) for each of these samples is presented in **Table 4-4**. Kfm samples account for most of the spectra due to the high abundance of carbonaceous material observed within select samples. Only three KJfb samples: LB16-18b, LB16-25a, and LB16-25b displayed enough carbonaceous material to be deemed suitable for RSCM analyses. Temperature calculations indicate that peak temperatures experienced within the Alder Creek study area and outlying areas cover a wide range from 160 °C up to 381 °C. The average maximum temperature experienced within the area is 267 °C.

Sample	Total Spectra	Average RA1	Standard Deviation	Temperature (°C)	Temperature Std. Dev.
LB16-12	25	0.591	0.065	269	87
LB16-18b	25	0.504	0.066	160	82
LB16-21	15	0.583	0.023	259	29
LB16-24	16	0.576	0.037	254	45
LB16-25a	28	0.594	0.041	273	51
LB16-25b	26	0.594	0.021	272	26
LB16-25d	25	0.554	0.079	223	45
LB16-27	32	0.589	0.029	266	32
LB16-29	15	0.593	0.026	271	36
BG16-57	27	0.681	0.035	381	43
BG16-58	13	0.599	0.035	278	43
BG16-61	29	0.617	0.050	301	61

Table 4-4. *Summary table of average RA1 and corresponding temperature values per sample.*

Chapter 5 - Discussion

5.1- Structural and lithologic controls on Alder Creek gold deposition

Polyphase folding present in the Alder Creek valley of the LBMD (**Figure 4-4**) indicates that the area was subjected to reorientation of the structures contemporaneous to the regional metamorphism. These events have been previously defined in this study as E_1 and E_2, respectively. E_1, which produced folds oriented ~N350° (**Figure 4-4** D), is inferred to be the product of regional compression and metamorphism associated with subduction and accretion of the sediments of the Nacimiento block during the Jurassic period (Chapman et al., 2016).

Reoriented fold axes during E_2 trend ~N070° (**Figure 4-4** F). The origin for this structural reorientation is likely tied to dextral fault motion of nearby fault systems. A combination of compressional E_1 deformation with E_2 strike-slip offset is seen in the inferred regional fabric (**Figure 4-7**). As a result, the local fabric displays a sinistral sense of shear seemingly contradictory to the dextral motion associated with the major bounding fault of the Nacimiento block, the Nacimiento fault. This discrepancy can be understood when one considers the LBMD and surrounding region as an interfault block residing between the San Gregorio-San Simeon-Hosgri fault system to the west and the Nacimiento fault to the east (**Figure 2-1**) within the larger, regional tectonic setting depicted in **Figure 4-8**. Motion within this interfault block is subsequently sinistral to accommodate the relative displacement along the bounding, dextral faults.

Given the compressional and translational stresses applied to the region, the hypothesis advanced here is that the LBMD lies within a minor, transpressional flower structure. The presence of a flower structure within the Alder Creek study area would potentially explain the hypothesized presence of reverse faults, as shown in the cross-sections in **Figure 4-10** and

Figure 4-11. While reverse faulting would explain the presence of structurally lower KJfb units noted within the center of the study area (**Figure 4-10**), it is worth noting that folding within the study area, and even Alder Creek stream erosion may also play a role in the observed exposure. While one can also cast doubt on the interpretation of a flower structure by pointing to difficulties in unit identification due to lithologic similarity between units KJfb and Kfm and complex tectonic fabrics, the evidence of myolinitic zones (**Figure 4-1** D) in and around outcrops such as LB16-25 within the central portion of the study area (**Figure 4-3**) is consistent with the presence of metagraywacke in descriptions of unit KJfb (Graymer et al., 2014). If this identification is correct, then upward displacement caused by transpressional stresses is likely accommodated by local faults and shearing (**Figure 4-2**). At present the amount of vertical offset is unknown, but is likely less than 160 m, as inferred from cross-sectional reconstructions (**Figure 4-10** and **Figure 4-11**).

Au mineralization within LBMD is associated with massive quartz-sulfide veins oriented N340˚ (**Figure 5-1**). Abandoned mine galleries are aligned approximately parallel to this trend, which corresponds with the maximum principal stress inferred during E_2 reorientation (**Figure 5-1**). This parallel alignment suggests that Au-deposit formed en-echelon vein arrays along fold limb during D_2 reorientation. Evidence of extension veins is also visible at the micro-scale in thin section, best exemplified in LB16-21 (**Figure 4-17**), where crystal growth is perpendicular to vein boundaries as well as at an angle to σ_1.

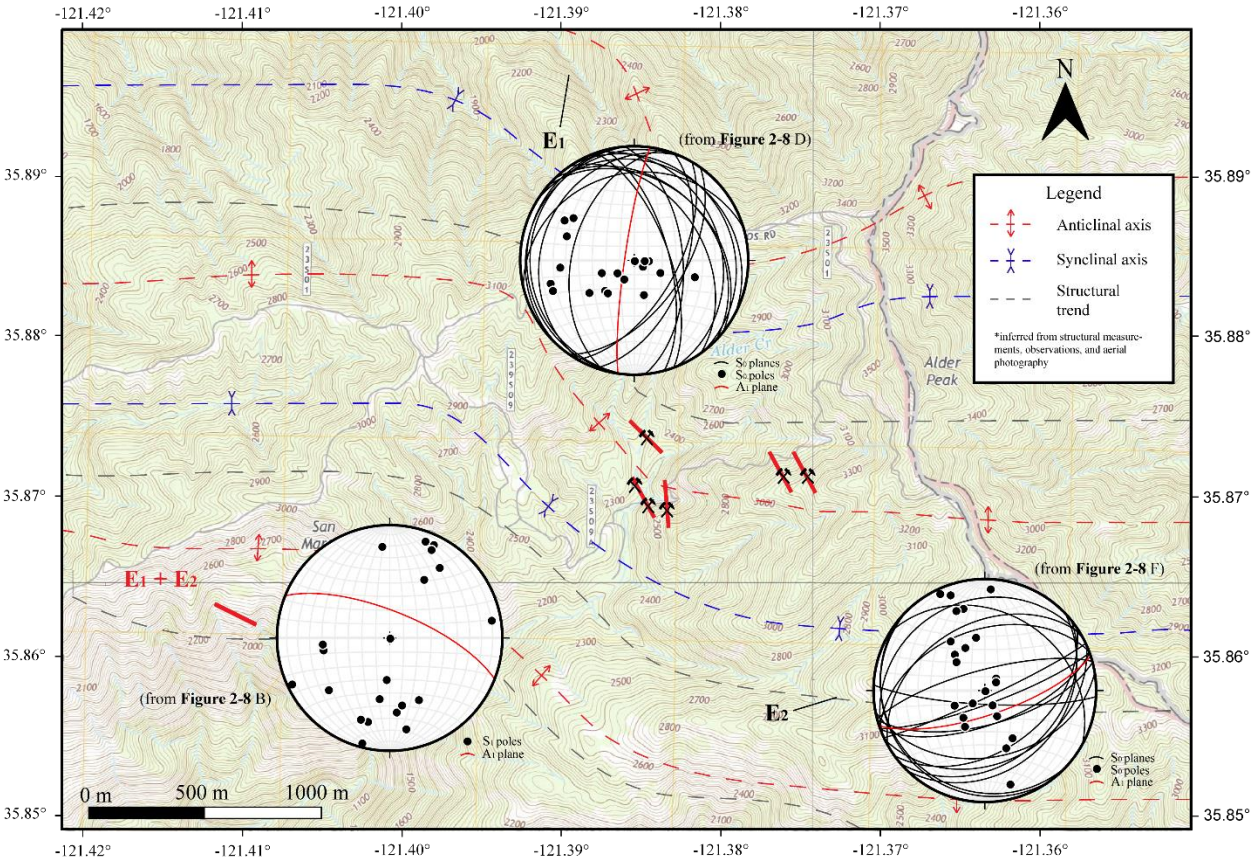

Figure 5-1. *Inferred regional stresses and deposit trends taken from the orientation of observed mine shafts.*

Furthermore, we hypothesize that Alder Creek gold emplacement is not governed solely by deformational event E_2 but may also be dependent upon host lithology. The serpentinite (Jsp) is the oldest and structurally lowest unit in the sequence found within the LBMD. The dense, altered mafic units of Jsp altered by serpentinization during deformation are less likely to strain. Serpentinite (Jsp) was found in a relatively restricted portion of the study area running approximately northeast to southwest (**Figure 4-9**). It is unlikely that this unit is competent enough to form extension veins.

Overlying units KJfb and Kfm are similar in that they both likely represent tectonically re-worked siliciclastic sediments (Graymer et al., 2014). Unit Kfm has a lower structural integrity than KJfb, since it is comprised of tectonically re-worked shales, mudstones, and

greywacke. In contrast to the less competent siliciclastic rocks, the thick sandstone units of KJfb are stiff and likely deformed in a brittle fashion. The veins collected from LB16-21 and LB16-24, which seem to be related to Au mineralization, came from these sandstone units within KJfb.

The inherent difference in competence between units KJfb and Kfm plays a role in controlling gold emplacement. During deformation, the shale matrix of the Kfm mélange deforms readily. This displacement is magnified at the contact between Kfm and KJfb, likely providing an ideal fluid-flow pathway. Observations of KJfb indicate that relatively thick sandstone units within would provide an ideal host lithology, as it experiences enough deformation to accommodate veins during E_2, creating open fractures available for gold deposition. Rheological differences are naturally accentuated at the contact between KJfb and Kfm, leading to the highest amount of displacement, particularly along fold hinges, and providing the greatest accommodation for the emplacement of en-echelon veins within KJfb at the base of the contact. The largest and most sulfide-rich galleries, located at LB16-21 and LB16-24 (**Figure 2-5**), were sunk within massive greywackes rich in carbonaceous material located close to the inferred contact. Graphitic slate tailings below these galleries and the carbon-rich greywacke described above are analogous to the black slates and dark sandstones described by Hill (1922). These units played host to some of the principal gold deposits in the area, such as the Buclimo (Last Chance) mine.

Proximity to carbon-rich Kfm units may also have played a role in controlling gold emplacement through alteration of the aqueous geochemistry of the source fluid. The presence of carbonaceous material in association with gold, and its role in sourcing/reducing gold in orogenic systems, is well-documented (Craw, 2002; Bierlein and Smith, 2003; Henne and Craw, 2012; Hu et al., 2015). While the Franciscan complex is defined by a unique tectonic setting, other carbon-

rich, turbidite-hosted deposits in various metamorphic conditions (Gao and Kwak, 2010; Haynes et al., 1986) are comparable to the style of gold deposition hypothesized for the LBMD. This suggests that the links between carbonaceous material and gold deposition are largely unaffected by varying P/T conditions. Carbonaceous material can provide favorable conditions for gold deposition through 1) the reduction of gold in solution, and 2) the destabilization of Au-sulfides and ligands (Seward, 1973; Hu et al, 2015; Kribek et al, 2015).

A likely scenario for gold deposition within the LBMD revolves around the interaction of a reducing, gold-bearing hydrothermal fluid (possibly the product of metamorphic de-watering) with a much cooler, oxidizing meteoric fluid. Destabilization of gold colloids and ligands may occur as a result of changes in oxygen fugacity, temperature, and pH. In the scenario described above one might expect a reaction similar to the following equation (after Southam and Saunders, 2005) in which gold is released during the oxidation of seafloor sediments rich in arsenopyrite:

$$2FeAsS[Au] + 7O_2 + 2H_2O + H_2SO_4 \rightarrow Fe_2(SO_4)_3 + 2H_3AsO_4 + [Au]$$

Eq. 2

This type of reaction may be accentuated within particularly carbon-rich horizons, such as those observed within the rocks of the Franciscan complex. Such carbon-rich materials present within the Alder Creek study area suggest that the primary depositional conditions were particularly organic-rich and highly reducing. This, coupled with the known proximity to igneous activity, as indicated by the presence of pillow basalts within Jsp, provides ample context for interactions between gold (likely present as inclusions within sulfide mineral phases) and organic material.

Gold, being a noble metal, is not soluble in water, except under extremely acidic conditions, but may be transported under more neutral pH conditions common in groundwater by forming colloids and ligands (Reith et al, 2007). Formation of these compounds may occur via oxidation reactions as in the following equation (after Alymore and Muir, 2001):

$$Au + ¼\ O_2 + H^+ + 2S_2O_3^{2-} \rightarrow [Au(S_2O_3)_2^{3-}] + ½\ H2O$$

Eq. 3

Metamorphic de-watering likely occurred as a result of the elevated temperatures and pressures experienced during deformation and reorientation. This, coupled with formation of en-echelon extension veins during E_2, would have provided an avenue for the remobilization of the gold. Furthermore, the need for minor amounts of oxygen as indicated by Eq. 3 and the demonstrably lower salinities observed in sample LB16-08a FIAs suggests the involvement of an oxygenating, low-salinity fluid, typical for meteoric water. Meteoric water likely percolated through fault and fracture systems following E_2 reorientation.

5.2- Source fluid characterization

Based on the histograms and scatterplots presented in **Figure 5-2,** we can infer the existence of at least two, broad fluid populations recorded in FIAs hosted within sulfide-bearing quartz-calcite veins. The delineation of these populations comes from T_h distributions rather than salinity values. T_h values are strongly bimodal in samples LB16-21 and LB16-24, although this bimodality is less clear from LB16-08a. Salinity, on the other hand, lies within a well-defined range from 1 to 3 wt% NaCl equivalent across all samples, with only a few exceptions. Furthermore, there is no correlation between salinity and homogenization temperature, suggesting that fluid salinity was nearly constant during ore deposition.

The presence of two fluid populations is also supported by the type of gas present. On the histograms generated for each sample (**Figure 5-3**), most inclusions recorded in this study were observed to be gas-poor (blue curves), except for a relatively small subset from the higher T_h populations (See **Tables B-1** through **B-4**). Gas-bearing inclusions are comprised of CH_4-H_2O (blue and yellow curves) and CH_4-CO_2-H_2O (orange and red curves), as discussed previously, though the latter were observed significantly less with only 11 cases out of 170 total inclusions studied. Evidence for a high temperature, gas-rich population is supported by inclusions from LB16-21 and LB16-24, which record much higher average T_h and a greater abundance of $CH_4 \pm CO_2$ inclusions. **Table 5-1** compiled from the Raman characterization discussed in section **4.5.2** illustrates the link between higher relative temperature and gas content as observed in the LBMD samples described in this study. Sample LB16-08a did not show any CO_2-rich and/or CH_4-rich inclusions. T_h measurements are also uniformly lower than those of two other samples, suggesting vein formation during a post-ore stage.

Taken together, the histograms of LB16-08a, LB16-21 and LB16-24 and gas data presented in both section **4.5.2** and **Table 5-1** highlight the possibility of fluid inclusion population sub-divisions. This is based on the consistent clustering within T_h thresholds which has been marked by different colors (see **Figure 5-2**). Without additional data it is not possible to verify whether or not each cluster truly belongs to its own separate "sub-population" or merely represents a T_h continuum. Further work and data collection is necessary to either confirm or deny the potential presence of sub-populations delineated on the basis of both T_h and predominance of gas phases within each range.

Fluid CH_4 concentration was determined using the methods of Duan et al (1992) and Dubessy et al (2001) for determining concentration in a low-salinity H_2O system. Volumetric

calculations (see **Eq. 4** in Appendix B) were conducted assuming inclusions approximated an oblate spheroid with average equatorial and polar diameters of 20µm and 10µm respectively. The following equation was then used to calculate a volume, approximately $1.67E^{-8}$ cm^3:

$$0.523 \times A^2C$$

$$A = 2 \times \text{Equatorial Diameter}$$

$$C = 2 \times \text{Polar Diameter}$$

Eq. 4

The average concentration of these high-temperature, CH_4-bearing inclusions was found to be approximately 301 ppm (See **Table B-6**). CO_2 density calculations were also employed using procedures outlined by Wang et al (2011). These calculations produced an average CO_2 density of 0.15 g/cm^3, though the small sample size available, and concerns about minimal CO_2-gas bubble size, cast doubt on the validity of this result.

To conclude the fluid inclusion populations are instead inferred from homogenization temperature and informed by the presence or absence of inclusions containing small to moderate amounts of $CH_4 \pm CO_2$. The two major fluid populations identified in this study are 1) low temperature, gas-poor fluids and 2) high temperature, gas-rich fluids as supported by the Raman results (detailed in section **4.5.2)**.

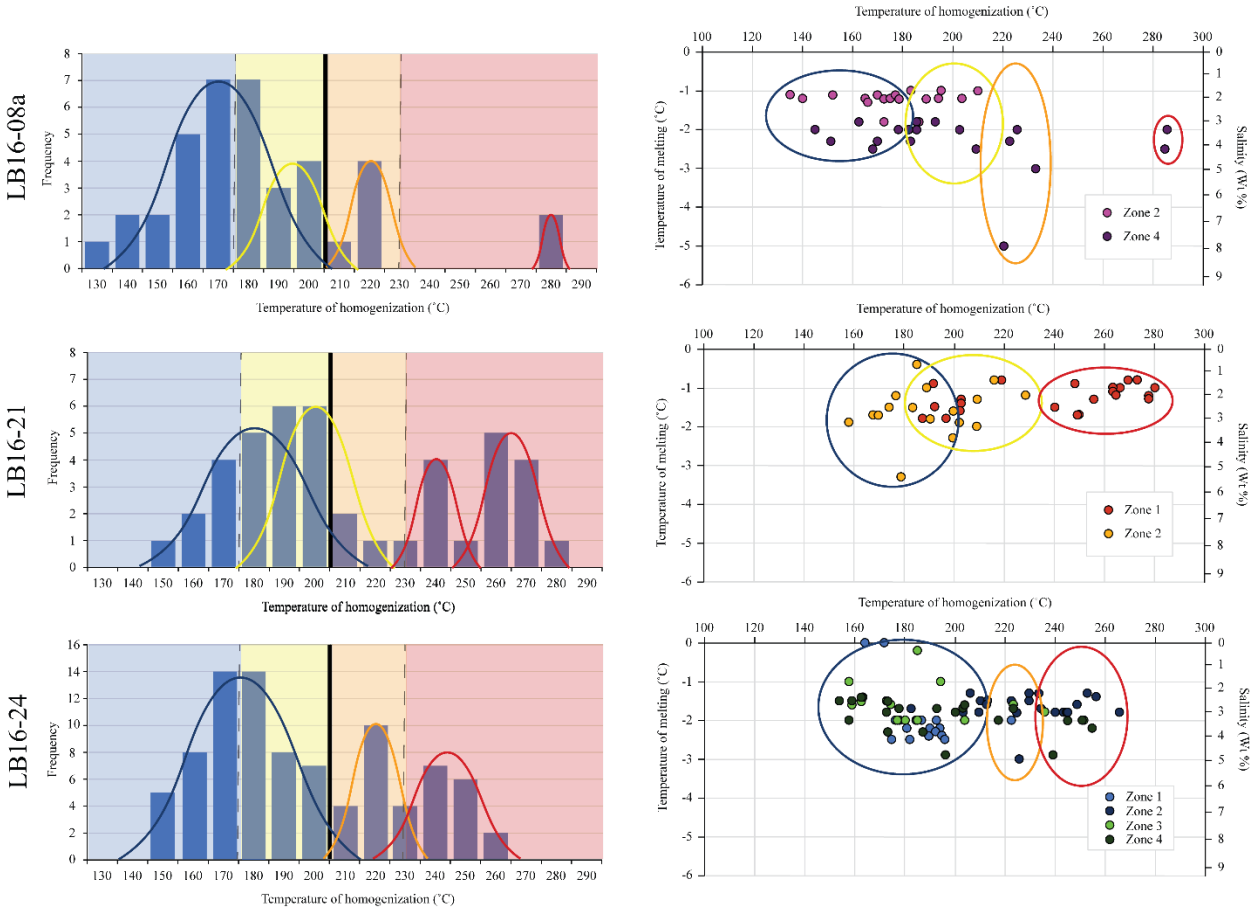

Figure 5-2. *Composite figure illustrating source fluid populations.* Highlights of blue, yellow, orange and red are used.

FI	FIA	Phase	V/L %	Tf	Tm	Th	Salinity wt%
24-2-g	p	LV*	15	-38	-1.6	248.6	2.74
24-3-a	p	LV*	25	-42.5	-2	251.3	3.39
24-3-b	p	LV*	7.5	-42	-1.8	235.7	3.06
21-1-a	p	LV +CO2	20	-41.9	-1.3	255.6	2.24
21-1-b	p	LV +CO2	25	-41.9	-1.3	277.5	2.24
21-1-c	p	LV*	15	-43	-0.8	218.8	1.40
21-1-e	4	LV+CO2	25	-41	-0.9	248	1.57
21-1-p	6	LV*	25	-40.4	-1	280	1.74
21-1-q	6	LV*	15	-40.8	-1.2	277.3	2.07
21-1-s	6	LV*	25	-43	-0.8	269.3	1.40
21-2-q	p	LV*	10	-43.8	3.2	178.6	-6.16

Table 5-1. *Table of CH_4+CO_2-bearing inclusions as determined by Raman analyses.*

5.3- P-T Condition of Au-deposition

Isochores were constructed for both low temperature, gas-poor populations and the high temperature, gas-rich populations (see **Figures B-19** to **B-20**). The isochoric system was assumed to be dominantly H_2O-NaCl since the overall concentration of gas in the system was observed to be low (below 1000 ppm) after Goldstein and Reynolds (1994). A pressure correction was not applied to the base H_2O-NaCl system since the assumptions required to account for the minor presence of both CH_4 and CO_2 into the system would introduce significant sources for error (after Goldstein and Reynolds, 1994).

A population of gas-bearing FIs homogenizing between 210°C and 235°C (composed of inclusions from both the yellow and orange curves from **Figure 5-2**) was selected for calculation of a representative isochore (**Figure 5-3**). Primary inclusions from this population were used because they contained the highest proportion of CH_4 and CO_2, were observed across all samples (particularly within LB16-24) and demonstrated a robust and narrow range of T_h. Selection of these FIAs was made following the criteria proposed by Goldstein and Reynolds (1994) in an effort to minimize potential sources of error such as decrepitation.

Average Raman spectroscopy of carbonaceous material temperature was used to represent a regional temperature maximum, since these temperatures demonstrated significant spatial variation (**Figure 5-5** and **Figure 5-6**). Both temperatures are plotted on **Figure 5-3**, since both thermometers ostensibly measure the temperature of the mineralizing fluid. It should be noted once again that temperatures derived from fluid inclusion microthermometry reflect minimum fluid entrapment temperatures, whereas temperatures observed via RSCM record a maximum temperature, since defects within the structure of the carbonaceous material are only over-written when subjected to higher temperatures and pressures. The average temperatures derived from fluid inclusion microthermometry and Raman Spectroscopy on Carbonaceous Material are remarkably similar, varying from an average of 257°C for the highest-temperature fluid inclusion population to an average RSCM temperature of 267.4°C. This was done to estimate pressure and geothermal gradient conditions for Au emplacement.

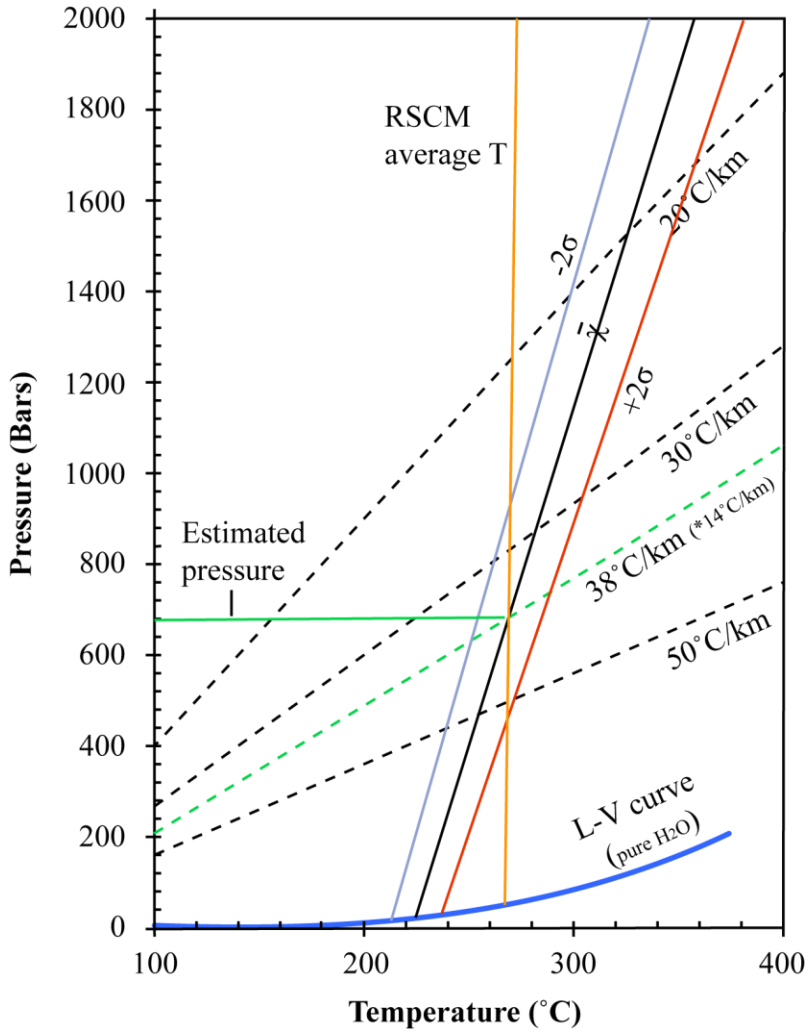

Figure 5-3. *Average RSCM temperature superimposed on the isochore (shown by the bold, black line) constructed from the highest recorded T_h population.* *Indicates approximate hydrostatic geothermal gradient.

The intersection of the T_{RSCM} with the fluid inclusion isochore provides a crude pressure estimate of 680 bars (**Figure 5-3**). A hypothetical geotherm was fitted to these data and calculated to represent an approximate lithostatic pressure of 38°C/km or a hydrostatic pressure of 14°C/km. Typical geothermal gradients within the Franciscan complex are 30°C/Km but can reach over 50°C/Km within some portions of Franciscan mélange subjected to elevated stress (Cloos, 1984). Since we are assuming the activity of a hydrothermal system acting at depth one

can assume that the pressure, as recorded by the fluid inclusion populations, must lie somewhere between true lithostatic and true hydrostatic regimes (the 38°C/km and 14°C/km line depicted in **Figure 5-3**).

The coupling of relatively high pressure at low temperature points to the action of fluid pressure locally altering the "normal" Franciscan geothermal gradient and also supports the assumption that metamorphically-derived hydrothermal fluids played a critical role in Los Burros gold deposition and, ultimately, the thermal anomaly reported by Underwood et al (1995).

5.3- RSCM geothermometry and relationship with Underwood's thermal anomaly

Underwood et al. (1995) demonstrated the existence of a thermal anomaly within the Lucia subterrane using illite crystallinity and vitrinite reflectance (**Figure 5-4**). Recent work (Lahfid et al., 2015; Lahfid et al., 2016) re-examined the thermal history of the Lucia subterrane using the RSCM geothermometer technique of Lahfid et al. (2010) (**Figure 5-5**). The results of these studies are largely in agreement with one another. Both maps indicate a thermal maximum centered on the LBMD, where the temperature difference is elevated by 100°C or more compared to more distal portions of the Lucia subterrane (**Figure 5-5**). There is also some degree of overlap in terms of the temperature contours suggested by these data, despite some discrepancies in the temperature range recorded in each study.

One of the principal goals of this study was to investigate this thermal maximum and provide higher resolution temperature data to better constrain the temperature gradient within the LBMD at the Alder Creek study location. The samples used for these analyses were KJfb and Kfm metasediments, rich in carbonaceous material, that are distributed throughout the study

area. **Figure 5-6** displays RSCM sample locations along with temperature contouring to illustrate an inferred temperature gradient within the LBMD. Data used to construct this map are presented in **Table 4-3**. Sample locations for all but samples BG16-57 and BG16-58 are also provided by the orange dots in **Figure 4-7**. This inferred gradient increases to the northwest. Notably, the temperature gradient is observed to increase again to the southwest in proximity to samples LB16-21 and LB16-24 collected near the most prolific mine galleries. This lends further credence to the notion of a hydrothermal over-print related to gold deposition.

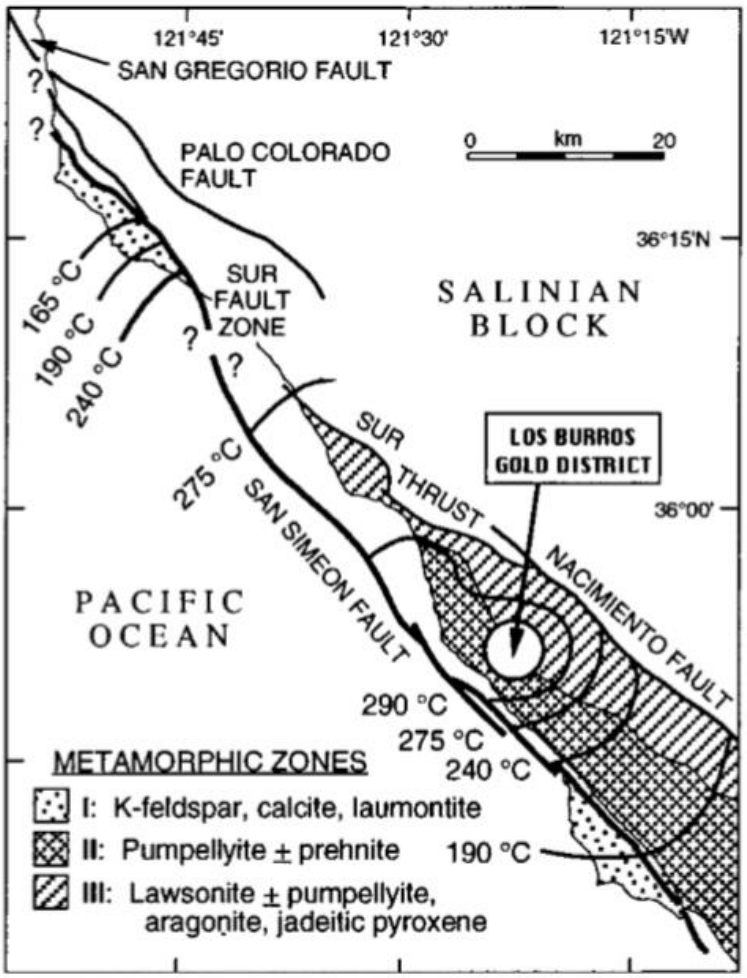

Figure 5-4. *Thermal contouring of the Lucia subterrane based on illite crystallinity and vitrinite reflectance data compiled by Underwood et al (1995).*

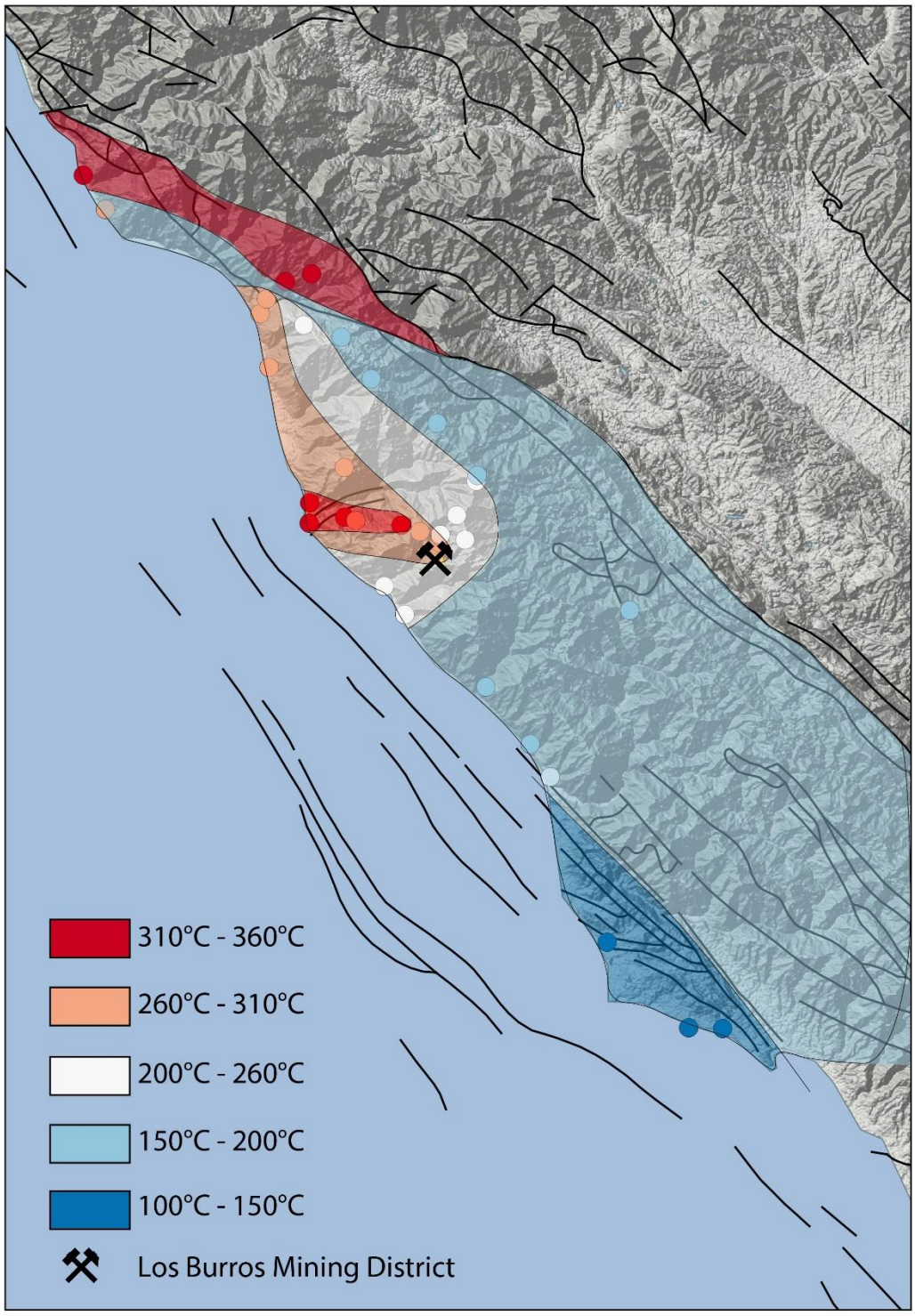

Figure 5-5. *RSCM thermometry temperature contours from the Lucia subterrane after Lahfid et al (2016).*

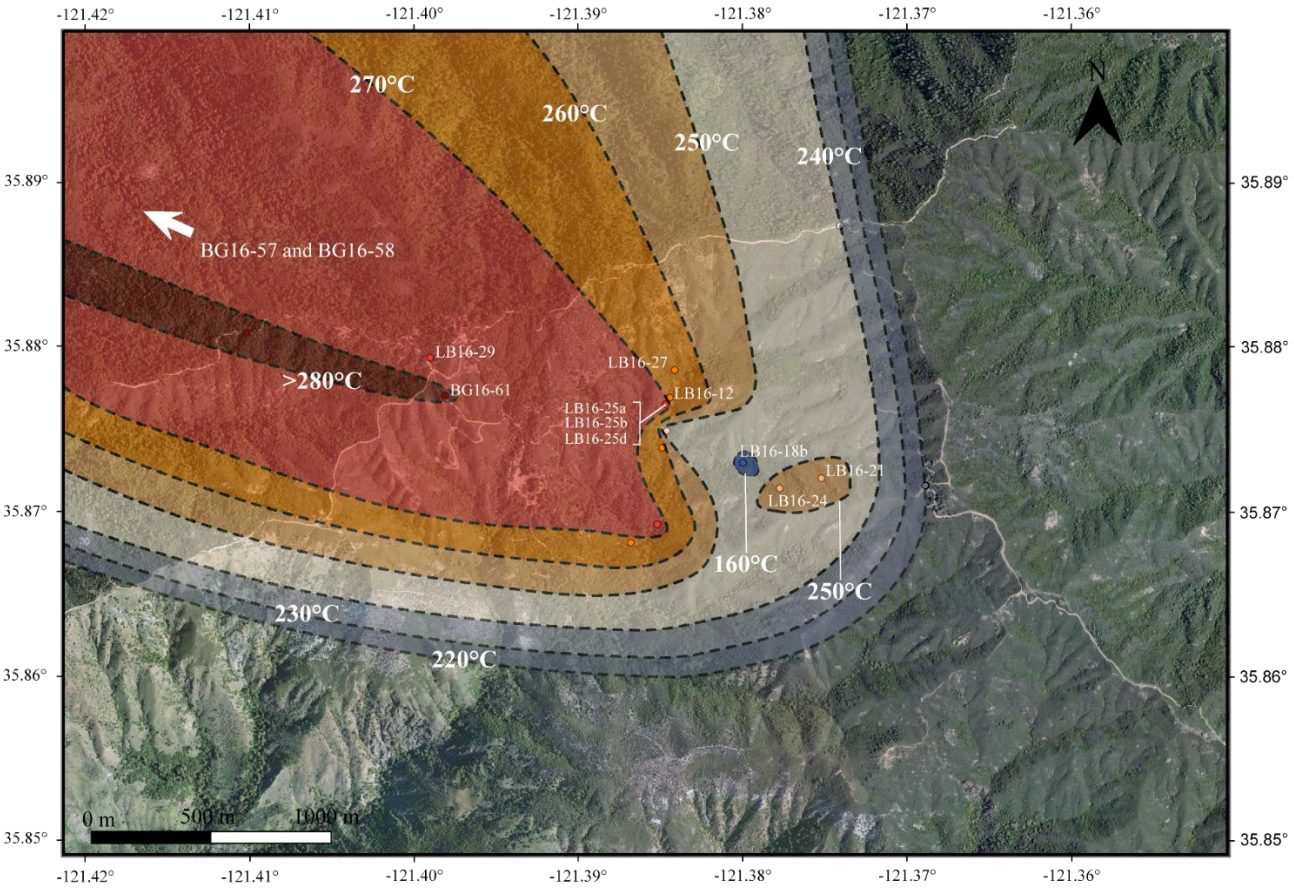

Figure 5-6. *Temperature contour map of RSCM temperatures within the Alder Creek study area.*

Interestingly, the locus of the thermal anomaly appears to be distal to the Alder Creek portion of the LBMD, as suggested by the work of Lahfid et al. (2016) as well as the results of this study. The true regional thermal maximum is likely northwest of Alder Creek within the Willow Creek basin. Furthermore, the highest temperature reported by of Lahfid et al. (2016) occurs proximal to mapped faults that coincide with the Willow Creek valley. The presence of faulting would promote local hydrothermal fluid-flow, potentially making it easier for the highest temperature source fluid to circulate and more completely affect the surrounding wall-rock. Alternatively, the presence of higher RSCM temperatures near fault-zones may indicate that an RSCM geothermometer is impacted by stress, which may alter the relative positions of the pertinent defect bands within the carbonaceous material (Lahfid et al., 2010). Ostensibly the

impact of stress on carbonaceous material within a high-pressure environment, such as the Franciscan complex, is less a question of plausibility and more a question of significance. We propose that carbonaceous material near fault and shear zones is likely to undergo significant strain, which may potentially bias thermometric calculations. This is a subject which will require more rigorous study. It is unclear whether the pressures expected within such a fault zone would be high enough to meaningfully impact RSCM measurements both directly next to the fault zone and significantly removed from it. Further study within the region and into the potential effects of stress on the RSCM geothermometer is warranted to verify the presence of faulting and elevated temperatures before attempting to credibly establish causality.

Chapter 6 - Conclusions

6.1- Emplacement model synthesis

Field observations within the study area support pre-existing accounts of LBMD gold occurrences (Davis, 1912; Hamilton, 1916; Hill, 1922). Even though no gold was encountered first-hand, the relative abundance of sulfide minerals such as pyrite, arsenopyrite, and chalcopyrite is encouraging, as is the presence of quartz in en-echelon veins both in and around abandoned mine shafts**.** Sulfide-bearing veins likely to have yielded gold were observed within host rocks ranging from light grey metagraywacke to dark graphitic slate. Veins appeared to be most abundant along the contact between these two lithologies. Field mapping and structural reconstructions based on measurements of S_0, S_1, and fold axes confirm the stratigraphy proposed by Graymer et al. (2014). It is, therefore, hypothesized that gold-bearing quartz veins were emplaced during E_2 by shear displacement of the lithological contacts between the metagreywackes of KJfb and the slate, shale, and mudrock mélange of Kfm.

Rheologic differences between KJfb and Kfm are accentuated by polyphase folding, which has been tied to compressional and transpressional stresses as summarized in **Figure 6-1**. **Figure 6-1** A depicts the onset of compressional forces within the LBMD (i.e. subduction of the Farallon plate). Deformation connected with this event (termed E_1) is associated with stresses oriented approximately east-west, which produced a generation of folds that are oriented approximately N350/30. Inset B of **Figure 6-1** shows the inception of this polyphase deformation through the dextral motion of the San Gregorio-San Simeon-Hosgri and Nacimiento fault systems. Inset C of **Figure 6-1** provides a representation of the hypothesized transpressional flower structure arising from crustal shortening and translational motion. Note the sinistral sense of shear also exhibited by the inferred fabric presented in **Figure 2-10** and **Figure 5-1**. This

sense of shear is likely due to motion by the interfault block to accommodate the dextral motion of the bounding fault systems. Deformation within this proposed flower structure, particularly at the KJfb-Kfm contact along fold axes, provided appropriate fluid flow pathways for gold emplacement. Vein growth patterns observed in thin sections of mineralized vein are best observed in **Figure 4-6.** These veins appear to have formed as extension or en echelon veins propagating via repeated crack-seal events within a pressure of about 680 bars based on calculations presented in **Figure 5-3.**

The source fluid for the LBMD gold deposits is likely derived from the metamorphic de-watering of organic-rich sediments, though a thorough analysis of hydrogen and oxygen isotopes from vein phyllosilicates and quartz respectively will be necessary to test this hypothesis. As outlined in chapter 5, gold may have been sourced as inclusions in pyrite/arsenopyrite. Carbonaceous source material may also be responsible for the presence of CH_4 (Seward, 1973; Hu et al, 2015; Kribek et al, 2015) and very minor amounts of CO_2 reported from fluid inclusion microthermometry and Raman analysis. Lastly, fracturing and faulting due to deformational events likely allowed for a large amount of mixing with meteoric water, as suggested by low salinity values (below 3%). Mixing with meteoric water would have changed the geochemistry of the fluid, most notably the oxygen fugacity and pH. Departures in these key parameters from those of the source fluid would affect gold solubility, leading to precipitation in a more oxic, pH neutral environment.

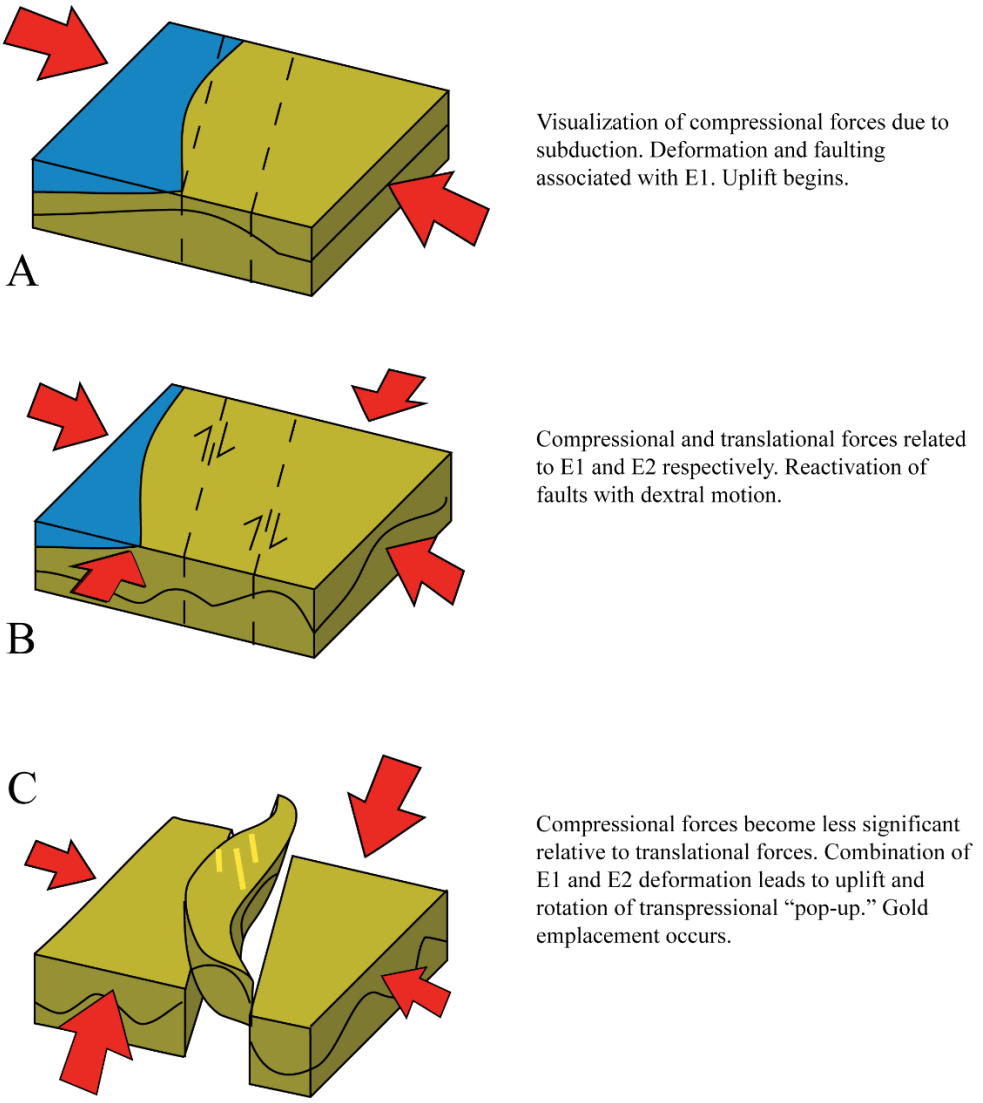

Figure 6-1. *Block diagram representing structural controls on LBMD gold deposition.*

6.2- Applications and future research

RSCM geothermometry results from this study are consistent with temperature calculations derived fluid inclusion microthermometry, illite crystallinity (conducted by Underwood et al., 1995) and regional RSCM calculations carried out by Lahfid et al. (2015) shown in **Figure 5-5**. This result is encouraging, as it shows that the RSCM method developed by Lahfid et al. (2010) may be employed in other geologic settings with some measure of confidence. Secondarily, application of the RSCM geothermometer in this way may prove

beneficial in future studies within hydrothermally active study areas as a relative quick, yet effective, measure of peak temperature. In this way, RSCM could help to quickly locate areas of higher or lower temperature that may be of interest to future researchers or prospectors. Additional research should also be conducted to verify whether subjecting carbonaceous material to extreme strain, such as along a shear zone, might bias the results of RSCM geothermometer calculations to ensure the accuracy of the results put forward by this study.

Further research into the character of the source fluid and the potential mechanisms for abiotic and/or biotic gold sources is also necessary to constrain conditions and augment the models proposed in Chapter 5. Isotopic analyses of vein quartz and gangue minerals such as chlorite surrounding the veins may provide a useful corollary to delineate the importance and/or proportion of metamorphic vs. magmatic vs. meteoric fluid.

Additionally, structural analyses seem to suggest that gold emplacement within the LBMD is, in part, a response to structural controls, namely the rheology of host lithologies and the folding and faulting associated with the inferred flower structure. Further research is necessary to corroborate whether this flower structure exists. This study of a localized orogenic gold deposit may also prove useful as a case-study for other minor deposits within the Franciscan complex by indicating likely host horizons, structures, and fluid characteristics to target for future research.

Chapter 7 - Appendix A: Methods

The centrifugation procedure described in **Section 3.2.2** did not require the measurement of exact weights into each bottle; only an equal weight distribution between the centrifuge bottles was necessary during the centrifugation process. The weight of each bottle was homogenized via the addition of DI water as needed such that all bottles were at equivalent weights to within a tolerance of 0.1 gram. Hydrochloric acid was carefully drained and disposed of following each wash cycle.

In preparation for fluid inclusion microthermometry the three samples of interest were placed in petri dishes, immersed in acetone, sealed to prevent acetone evaporation, and heated at 40˚C for twelve hours using a Fisher Scientific Isotemp oven. This was done to dissolve the cyanoacrylate adhesive to make the "thick section" easier to remove from the slide. Following this step samples were gently washed in DI water to remove any residuum and allowed to air-dry for a couple of hours. An X-Acto knife was used to cut out small chips (less than 1 cm^3) around zones of interest.

Chapter 8 - Appendix B: Data

	FI	FIA	Phase	V/L %	Tf	Tm	Th	Salinity wt%
8a-2	a	1	LV*	7.5	-44	-1.2	175	2.07
	b	1	LV*	12.5	-44	-1.2	165	2.07
	c	1	LV*	5	-44	-1.2	189.4	2.07
	d	1	LV* + N2	15	-44	-1.2	140	2.07
	e	1	LV*	5	-39	-1.1	177.5	1.91
	g	1	LV*	5	-39	-1.1	170	1.91
	h	3	LV*	5	-36	-1.2	178.5	2.07
	i	3	LV*	7.5	-38	-1.3	166	2.24
	m	3	LV*	7.5	-38	-1.2	194.2	2.07
	l	3	LV*	7.5	-36	-1.1	135	1.91
	k	3	LV*	7.5	-36	-1.1	152	1.91
	o	3	LV*	10	-42	-1.2	203.6	2.07
	u	3	LVH2O	5	-42	-1.2	172.5	2.07
	s	3	LV*	10	-36	-1	183.2	1.74
	r	3	LV*	10	-36	-1	210	1.74
	q	3	LV*	7.5	-36	-1	195.3	1.74
	t	4	LV*	7.5	-40	-1.8	185.6	3.06
	p	4	LV*	10	-40	-1.8	172.5	3.06
8a-4	a	1	LV*	7.5	-42	-2	145	3.39
	k	1	LV*	10	-39	-1.8	162.5	3.06
	e	1	LV*	7.5	-42	-2	182.4	3.39
	f	1	LV*	5	-44	-2	178.4	3.39
	c	1	LV*	15	-34	-2	225.7	3.39
	h	1	LV*	5	-44.5	-2.3	151.3	3.87
	l	1	LV*	10	-43.5	-2.3	183.1	3.87
	o	2	LCO2+VCO2	50	-44	-5	220.4	7.87
	m	2	LV*	10	-43.5	-2.3	169.9	3.87
	q	2	LV*	10	-43.5	-2.3	222.7	3.87
	v	2	LV*	15	-43.5	-2	202.7	3.39
	u	3	LV*	5	-45	-2.5	284.7	4.18
	g	4	LV*	7.5	-38	-2	185.6	3.39
	y	5	LV*	5	-45	-2.5	209.3	4.18
	z	5	LV*	5	-45	-2.5	209.3	4.18
	x	6	LV*	10	-36	-2.5	168	4.18
	b	p	LV*	15	-42	-2	285.6	3.39
	t	p	LV*	10	-44	-1.8	186.5	3.06
	w	p	LV*	7.5	-36	-3	233.1	4.96
	d	p	LV*	7.5	-42.5	-1.8	193	3.06

Table B-2. *Table containing fluid inclusion microthermometry measurements along with calculated salinity for all LB16-08a fluid inclusions.* The letter 'p' denotes inclusions which were determined to be primary whereas a number is used to signify an inclusion belonging to a secondary fluid inclusion array. * implies an inclusion comprised of liquid H_20 and CH_4 vapor.

	FI	FIA	Phase	V/L %	Tf	Tm	Th	Salinity wt%
21-1	a	p	LV +CO2	20	-41.9	-1.3	255.6	2.24
	b	p	LV +CO2	25	-41.9	-1.3	277.5	2.24
	c	p	LV*	15	-43	-0.8	218.8	1.40
	h	p	LV*	10	-43.3	-1.5	192	2.57
	j	p	LV*	30	-40.6	-1.5	240	2.57
	r	p	LV*	15	-47	-1.7	249	2.90
	w	p	LV*	15	-40.7	-1.3	202.4	2.24
	v	p	LV*	15	-40.7	-1.4	202.6	2.41
	i	3	LV*	10	-40.6	-1.6	202.2	2.74
	g	3	LV*	10	-40.6	-1.8	196.6	3.06
	d	p	LV*	15	-47	-1.7	249.4	2.90
	e	p	LV+CO2	25	-41	-0.9	248	1.57
	x	p	LV*	20	-41.3	-0.9	191.5	1.57
	f	p	LV*	15	-41.4	-1.8	187.2	3.06
	m	p	LV*	15	-42.7	-1	263.2	1.74
	k	p	LV*	20	-42.4	-1.1	263.2	1.91
	n	p	LV*	20	-44	-0.8	273	1.40
	o	p	LV*	15	-40.4	-1	266.1	1.74
	p	p	LV*	25	-40.4	-1	280	1.74
	q	p	LV*	15	-40.8	-1.2	277.3	2.07
	t	p	LV*	15	-40.2	-1.2	264.6	2.07
	l	p	LV*	10	-42.4	-0.8	272.9	1.40
	s	p	LV*	25	-43	-0.8	269.3	1.40
21-2	h	p	LV*	10	-40.5	-1.6	199.5	2.74
	d	p	LV*	15	-44.3	-1.8	190.4	3.06
	c	p	LV*	10	-43.7	-1	189	1.74
	x	p	LV*	25	-46.4	-1.9	157.7	3.23
	e	p	LV*	15	-44	-1.7	167.4	2.90
	f	p	LV*	20	-43.6	-1.3	209	2.24
	w	p	LV*	20	-44	-1.7	169.5	2.90
	k	p	LV*	10	-43	-3.3	178.6	5.41
	z	p	LV*	10	-43.9	-1.5	183.2	2.57
	v	p	LV*	10	-42	-1.2	228.3	2.07
	a	p	LV*	10	-42	-1.2	176.5	2.07
	y	p	LV*	10	-41.8	-1.9	201.9	3.23
	p	p	LV*	20	-42.9	7.2	230.1	-15.30
	q	p	LV*	10	-43.8	3.2	178.6	-6.16
	m	2	LV*	15	-46.8	-0.4	184.9	0.70
	n	2	LV*	20	-46.8	-0.8	215.8	1.40
	i	3	LV*	15	-45.7	-2	208.8	3.39
	r	4	LV*	10	-46.8	-1.5	173.8	2.57
	j	5	LV*	15	-43.8	7.2	182	-15.30
	l	5	LV*	10	-45.1	-2.3	199.3	0.00

Table B-3. *Table containing fluid inclusion microthermometry measurements along with calculated salinity for all LB16-21 fluid inclusions.* The letter 'p' denotes inclusions which were determined to be primary whereas a number is used to signify an inclusion belonging to a secondary fluid inclusion array. * implies an inclusion comprised of liquid H_20 and CH_4 vapor.

	FI	FIA	Phase	V/L %	Tf	Tm	Th	Salinity wt%
24-1	f	1	LV*	7.5	-43.5	-2.4	189.4	4.03
	i	1	LV*	7.5	-44	-2	179.4	3.39
	o	1	LV*	15	-44.5	-2.5	181.8	4.18
	p	1	LH2O+VH20	5	-44	-2.2	189.8	3.71
	a	p	LV*	10	-42	-2.5	196	4.18
	g	2	LV*	5	-44.5	1.8	162.5	-3.35
	j	2	LV*	7.5	-44.5	1	162.5	-1.82
	c	3	LV*	7.5	-44	0	171.7	0.00
	b	3	LV*	7.5	-44	0	164.1	0.00
	d	p	LV*	10	-44	-2.3	192.1	3.87
	e	p	LV*	5	-44	-2	185.7	3.39
	x	p	LV*	7.5	-44	-2	222.4	3.39
	q	p	LV*	5	-44	5	173	-10.07
	r	p	LV*	7.5	-42	8	178.8	-17.34
	w	p	LV*	10	-44	18	166.4	-49.54
	l	4	LV*	10	-44	-2.5	174.5	4.18
	n	p	LV*	15	-43.5	-2.4	188.8	4.03
	m	p	LV*	10	-43.5	-2.4	194.3	4.03
	s	p	LV*	20	-44	-2.2	180.6	3.71
	v	p	LV*	10	-43	-2	186.7	3.39
	u	p	LV*	7.5	-44	-2.2	193.8	3.71
	y	p	LV*	10	-43.5	-2	192.4	3.39
	z	p	LV*	5	-43.5	-2	176.3	3.39
	t	p	LV*	20	-43.5	-2	184.3	3.39
	h	p	LV*	5	-43	15	162.2	-38.48
24-2	a	p	LV*	10	-42	-3	225.5	4.96
	g	p	LV*	15	-38	-1.6	248.6	2.74
	h	p	LV*	10	-38	-1.6	212.4	2.74
	m	p	LV*	7.5	-42	-1.8	203	3.06
	n	p	LV*	10	-42	-1.8	224.5	3.06
	l	p	LV*	25	-42	-1.8	265.5	3.06
	o	p	LV*	10	-42	-1.8	265.5	3.06
	r	p	LV*	7.5	-40	-1.5	222.4	2.57
	s	p	LV*	7.5	-40	-1.5	229.4	2.57
	t	p	LV*	7.5	-40	-1.5	212.8	2.57
	v	p	LV*	10	-38	-1.8	244.1	3.06
	w	p	LV*	25	-38	-1.8	243.2	3.06
	x	p	LV*	10	-38	-1.8	240	3.06
	v	p	LV*	10	-38	-1.8	244.1	3.06
	d	1	LV*	25	-41.8	-1.3	229.5	2.24
	e	p	LV*	15	-41.8	-1.3	205.9	2.24
	f	1	LV*	25	-41.8	-1.3	233.3	2.24
	u	p	LV*	20	-39	-1.8	209.4	3.06
	c	1	LV*	10	-41.8	-1.3	252.7	2.24
	q	2	LV*	7.5	-41	-1.4	256.2	2.41
	b	4	LV*	10	-44	-1.7	234.2	2.90
	y	5	LV*	10	-39	-1.5	210	2.57

Table B-4. *Table containing fluid inclusion microthermometry measurements along with calculated salinity for LB16-24 fluid inclusions from zones 1 and 2.* The letter 'p' denotes inclusions which were determined to be primary whereas a number is used to signify an inclusion belonging to a secondary fluid inclusion array. * implies an inclusion comprised of liquid H_20 and CH_4 vapor.

	FI	FIA	Phase	V/L %	Tf	Tm	Th	Salinity wt%
24-3	a	p	LV*	25	-42.5	-2	251.3	3.39
	f	p	LV*	10	-42.5	-2	203.7	3.39
	b	p	LV*	7.5	-42	-1.8	235.7	3.06
	g	1	LH2O+VH2O	20	-42.4	-0.2	184.8	0.35
	h	1	LV*	15	-42	-2	177.5	3.39
	k	1	LV*	10	-43.6	-2	176.3	3.39
	l	1	LV*	7.5	-44	-2	186.1	3.39
	m	1	LV*	7.5	-44	-2	180.1	3.39
	r	1	LV*	15	-43.7	-1.6	174.2	2.74
	n	1	LV*	10	-43.7	-1.6	159	2.74
	s	p	LV*	10	-43.5	-1.5	162.4	2.57
	t	p	LV*	7.5	-43.5	-1.5	172.5	2.57
	x	p	LV*	10	-43	-1	157.5	1.74
	u	p	LV*	10	-43	-1	194	1.74
	e	p	LV*	15	-42	-1.8	244.4	3.06
	o	3	LV*	20	-42	0.5	223.7	-0.90
	p	p	LV*	20	-42	0.5	224.8	-0.90
	q	p	LV*	15	-42	0.5	250.4	-0.90
	c	4	LV*	7.5	-42	-1.6	223.1	2.74
	d	4	LV*	15	-42	-1.8	245.2	3.06
24-4	a	2	LV*	20	-42	-1.7	192.5	2.90
	u	p	LV*	21.5	-43	-1.8	200	3.06
	q	2	LV*	7.5	-42	-1.5	153.6	2.57
	r	2	LV*	7.5	-42	-1.5	158.7	2.57
	t	2	LV*	10	-42	-1.7	203	2.90
	o	2	LV*	10	-43.5	-1.7	177.5	2.90
	w	2	LV*	7.5	-43.5	-1.7	223.5	2.90
	f	2	LV*	20	-42	-2.3	173	3.87
	l	2	LV*	25	-43.5	-1.4	163	2.41
	v	2	LV*	15	-42	-2.3	187	3.87
	d	2	LV*	10	-43.5	-1.4	162.5	2.41
	y	p	LV*	10	-43	-1.6	203.8	2.74
	z	p	LV*	10	-43	-1.5	172.5	2.57
	x	p	LV*	10	-43	-1.8	172.5	3.06
	i	p	LV*	15	-38	-2.2	254.6	3.71
	m	p	LV*	5	-44	-2.9	239	4.81
	j	p	LV*	5	-44	-2.9	196	4.81
	e	1	LV*	7.5	-40	-2	157.5	3.39
	c	3	LV*	5	-38	-2	245	3.39
	b	4	LV*	5	-40	-2	251.5	3.39
	g	4	LV*	5	-38	-2	217.2	3.39
	h	4	LV*	15	-38	-2	185	3.39

Table B-5. *Table containing fluid inclusion microthermometry measurements along with calculated salinity for LB16-24 fluid inclusions from zones 3 and 4.* The letter 'p' denotes inclusions which were determined to be primary whereas a number is used to signify an inclusion belonging to a secondary fluid inclusion array. * implies an inclusion comprised of liquid H_20 and CH_4 vapor.

FI Zone	Average Salinity	Salinity Error	Average Th	Th Error
08a-2	2.10	0.37	176	19
08a-4	3.90	1.03	200	37
21-1	2.13	0.56	241	32
21-2	1.99	1.15	191	19
24-1	3.33	1.98	182	13
24-2	2.84	0.56	232	18
24-3	2.20	1.49	201	32
24-4	3.23	0.66	195	31

Table B-6. *Summary table for salinity (in wt% NaCl equivalent) and homogenization temperature (T_h- given in °C) along with their respective standard errors.*

Thin Section Descriptions

LB16-01- Metabasalt

The sample is dominated by a disordered, fine-grained plagioclase matrix (roughly 70% abundance). The sample is also highly fractured with hypothesized sericitization prominent, particularly in the more fractured portions of the thin section. Sericitization of muscovite (modal abundance of approximately 5%) appears to occur in the form of exsolution lamellae. Plagioclase phenocrysts appear to constitute roughly 15% of the modal mineralogy and exhibit rounding and resorption. Wollastonite characterized by a birefringeance of high second-order/low third order blues and greens are observed in close proximity to some of the larger plagioclase crystals. Minor amounts of orthopyroxene (less than 3%) are present as well bringing the total estimated amount of pyroxene within the sample to around 7%. Oxides, likely spinel and possibly magnetite, are prolific along fractures, but only comprise roughly 3% of the sample. Oxides are also noted as intergrowth within fine-grained plagioclase matrix.

LB16-03- Glaucophane Schist

Light blue to green (lavender in spots) glaucophane dominant (approximately 55%). The thin section displays foliation in spots, but is significantly disordered with angular clasts of glaucophane + biotite + plagioclase. Fracturing is present within the sample and is concentrated nearest a vein which is filled by quartz, plagioclase, as well as muscovite, and biotite. Additionally, a brown, platy chlorite variety is observed throughout the sample. Micas comprise a relatively high percentage of the sample with estimated values of 15% for biotite, 5% for muscovite, and 15% for chlorite. Muscovite and plagioclase (comprising approximately 5% of the sample) are observed together and are concentrated nearest the prominent vein which runs through the sample. Sericitization is also observed along this vein. Lastly, accessory oxides are observed in low abundance (approximately 3%) while resorbed two-pyroxene assemblages are also noted, though extremely minor (roughly 2%).

LB16-04- Muscovite Schist

Muscovite is dominant within this thin section, constituting nearly 60% of the estimated modal mineralogy. The muscovite is ordered around crenulations which include the presence of oxides, found within fold axes or along the limbs of crenulations. Oxides account for nearly 5% of the modal mineralogy of this sample. Mildly pleochroic chlorite is also noted intergrown within the muscovite. This chlorite has an overall abundance of roughly 10%. Very fine-grained plagioclase laths (making up 15% of the thin section) are present showing resorption features along with muscovite/sericite replacement and intergrowths. Sericitization of this sample is markedly less than that observed in samples LB16-01 and LB16-03. Quartz (5%) is observed in isolated veins typically defined by crenulation morphology. Orthopyroxene and minor wollastonite are also observed but display a high degree of fracturing and resorption. Oxides

occur along crenulation limbs and axes and range from rounded to blocky (less than 5% total abundance).

LB16-05- Glaucophane Schist

Glaucophane is dominant (nearly 55%) and occurs as blocky prisms. The sample displays a well-defined foliation which is highlighted by an abundance of mica (10% muscovite, 10% biotite, and 10% chlorite). Very minor clinopyroxene is present (less than 4%) and displays a high degree of fracturing and resorption. The thin section is fairly homogenous throughout sans the presence of highly altered fractures. Fractures contain minor quartz and plagioclase which display evidence of sericitization. Together, quartz and plagioclase comprise 10% of the sample. A rusty-red alteration is visible along fractured surfaces suggesting the presence of iron oxy-hydroxides (approximately 5% of sample modal mineralogy).

LB16-08a and LB16-08b- Quartz Vein

These samples are cut from a sample of massive quartz vein, which is reflected in their modal mineralogy. As expected, these samples are almost entirely quartz, though the optical purtiy of the quartz varies significantly between the samples and even within each sample. Significant portions of quartz from sample LB16-08b display a buff tan coloration in plain polarized light. This discoloration may be in response to weathering from micro-fractures which pervade the sample. LB16-08a contains the most optically pure quartz within which the presence of numerous fluid inclusion assemblages is noted. Micro-fractures are observed in both samples, though LB16-08a displays only one prominent fracture which traverses the sample, nearly bisecting it. Oxides range from rounded to sub-angular and account for less than 5% of the estimated modal mineralogy.

LB16-12- Metagreywacke

The sample is fairly homogeneous with microcrystalline quartz, microcline, and plagioclase dominant (modal abundances of 30%, 15% and 30% respectively). Angular quartz phenocrysts are also present. The sample is well-foliated with the foliation being defined by the presence of rounded oxide grains as well as dark lenses of carbonaceous material. This sample contains a slightly higher abundance of oxides than those discussed previously, estimated to be between 5% and 10% modal abundance. Microcrystalline mica in the form of sericite alteration is observed with respect to plagioclase. Mica is also present within the groundmass as muscovite (nearly 10% abundance) as well as chlorite, identifiable by anomalous blue interference colors.

LB16-16- Glaucophane Schist

This sample is notably 'clean' with a conspicuous absence of oxide phases and sericitization. The sample displays a strong foliation and is dominated by glaucophane (an estimated 60% abundance). Glaucophane from this sample is not as pleochroic as glaucophane in other glaucophane schists described previously. Quartz and muscovite (comprising roughly 20% modal abundance each) are observed throughout the sample. Muscovite, in tandem with glaucophane, defines the foliation present within this sample.

LB16-17- Glaucophane Schist

This sample represents a highly folded glaucophane schist. Once again, glaucophane is the most common mineral accounting for nearly 55% of the modal mineralogy. Quartz veins, while altered extensively by rusty, red-brown iron oxy-hydroxides intergrowths, are found to follow the foliation present within this sample. Oxides account for a relatively minor proportion of the samples modal mineralogy, however; under 5%. Muscovite and sericite (roughly 10% abundance each) are observed throughout the sample. Of note within this thin sample is the

preservation of folds and microstructure. Quartz veinlets may be seen to expand in width from less than 0.25 cm to 0.5 cm near fold hinges.

LB16-18- Metagreywacke

The sample is similar in texture and modal mineralogy to sample LB16-12. Quartz constitutes a plurality of the modal mineralogy (40%). Together with fine-grained plagioclase and microcline (35% abundance) these two minerals comprise the groundmass which appears to display only minor foliation. Plagioclase phenocrysts up to 0.25 cm in size are present, but in very low amounts (less than 3% abundance). Isolated occurrences of carbonaceous material and oxides are strewn throughout the groundmass, with the carbonaceous material serving to define the limited foliation. A 0.5 cm wide swathe of carbonaceous material may be seen forming a semi-continuous band across the sample. In total, carbonaceous material comprises approximately 20% of the sample. Sericite replacement may be seen along some microcline. Lastly, a minor amount of chlorite (less than 3%) is observed within the groundmass.

LB16-21- Quartz Vein

This sample was taken from a portion of quartz vein relatively close to an abandoned mine shaft (see **Figure 4-3**). The sample is divided into a quartz vein (75%) and rock fragment (25%). The rock fragment contained within the thin section is well-foliated with the foliation being defined by quartz within a clayey, carbonaceous-rich matrix. Secondary quartz veins (approximately 0.25 cm in width) cross-cut this foliation. Carbonaceous material is concentrated around the intersection of the rock fragment with the main vein and is observed around the edges of the thin section. The quartz constituting the vein is optically pure in some portions and a number of fluid inclusion assemblages are visible.

LB16-24a and LB16-24b- Quartz Vein

These two samples provide a bit of quartz vein hosted within metagraywacke (similar to sample LB16-18 and LB16-12) found in float near an abandoned mine gallery (see **Figure 4-3**). Nearly one half of the thin section for LB16-24b is composed of this metagraywacke. The sample is well-laminated with laminations principally defined by carbonaceous material (10% modal abundance). Rounded oxides (less than 5% abundance) are found as intergrowths within a predominantly quartz and microcline-rich matrix similar to that described in sample LB16-18. The quartz vein exposed in sample LB16-24b is somewhat cloudy, making the identification of fluid inclusion assemblages difficult. Carbonaceous material is observed in bands from 0.25 cm to 0.5 cm in width within the vein. The carbonaceous material is observed in proximity to altered microcline and clay minerals. The thin section for LB16-24a contains much more optically pure quartz which comprised approximately 75% of the sample. In plain polarized light a green mineral is visible in the middle of the thin section and may be highly oxidized copper sulfides. Epidote alteration is common throughout both samples, found mostly near bands of carbonaceous material.

LB16-25a- Carbonaceous shale

This sample contains an extremely high amount of carbonaceous material (approximately 45% modal abundance) occurring in continuous bands with thicknesses greater than 0.5 cm. The sample displays a high degree of deformation but preserves some foliation and intricate micro-folds within the carbonaceous material. Interlayered between bands of carbonaceous material one can see approximately 0.5 cm thick bands of re-crystallized quartz (accounting for nearly 45% modal abundance). Minor amounts of plagioclase and microcline are also found within these bands (approximately 5% total). Oxides are irregularly shaped and elongate parallel to quartz-rich layers and carbonaceous-rich bands.

LB16-25b- Carbonaceous Metagreywacke

Sample LB16-25b is similar to LB16-25a in that they both possess a high amount of carbonaceous material (corresponding to nearly 25% modal abundance in the case of LB16-25b). Foliation is better preserved within this sample by bands of carbonaceous material less than 0.25 cm in width. Quartz grains constitute a greater proportion of the sample (roughly 55%) with plagioclase and, to a lesser degree, microcline comprising the groundmass (15% total). Very little alteration is present and oxides within the sample account for less than 2% of the estimated total modal mineralogy.

LB16-25c- Metagreywacke

Sample LB16-25c is texturally similar to other metagreywackes described in the descriptions of LB16-12 and LB16-18, though with less developed foliation. Quartz and microcline grains are dominant (combining for nearly 70% of the estimated modal mineralogy) with fine-grained plagioclase occurring in minor amounts in the groundmass (5% to 10%). Carbonaceous material is present throughout, representing nearly 15% of the sample, and occurs in rounded lenses. Accessory muscovite (less than 5% abundance) can be seen along the weak foliation. Lastly, the thin section contains one prominent vein of calcite (with some dolomite) which cross-cuts the foliation.

LB16-25d- Metagreywacke

This sample is similar to LB16-25c only more altered and lacking any calcite/dolomite. Quartz grains are abundant along with some plagioclase and altered microcline. Quartz constitutes approximately 45% of the sample while the feldspars combine for roughly 40%. Isolated patches of carbonaceous material occur throughout and comprise approximately 5% of

the sample. Rusty, red-brown iron oxy-hydroxides are seen in low abundance (less than 5%) throughout the sample, particularly along a fracture spanning the width of the thin section.

LB16-25e- Carbonaceous Metagreywacke

Coarse-grained quartz makes up roughly 60% to 70% of the modal mineralogy of this sample, significantly higher than other metagraywackes discussed previously. Plagioclase and microcline occur in very low abundance (nearly 5% total). As is the case in the other LB16-25 samples, LB16-25e contains a relatively high amount of carbonaceous material (nearly 10%). Carbonaceous material within this sample is split between interstitial lenses within three-quarters of the sample, and very thin laminations in the remaining quarter. These carbonaceous laminations are hosted within a dark, clayey matrix which has an abrupt contact between it and the quartz-rich portion of the sample.

LB16-27- Carbonaceous Metagreywacke

Approximately two-thirds of this sample is similar to the homogeneous metagreywackes described previously in the petrographic descriptions for LB16-12 and LB16-18. The modal mineralogy of this portion of the thin section mimics that which is previously described as well: quartz constituting nearly 40%, plagioclase at 25%, and microcline at 15% along with a minor amount of muscovite (less than 5%). Carbonaceous material is abundant in this sample as well (modal abundance of approximately 15%), occurring as both isolated lenses along foliation and semi-continuous bands. This portion of the thin section also contains a couple prominent veins which are dominated by re-crystallized quartz and microcline throughout. The remaining third of this sample consists of a very dark, clayey matrix with a high content of carbonaceous material and demonstrates very fine lamination.

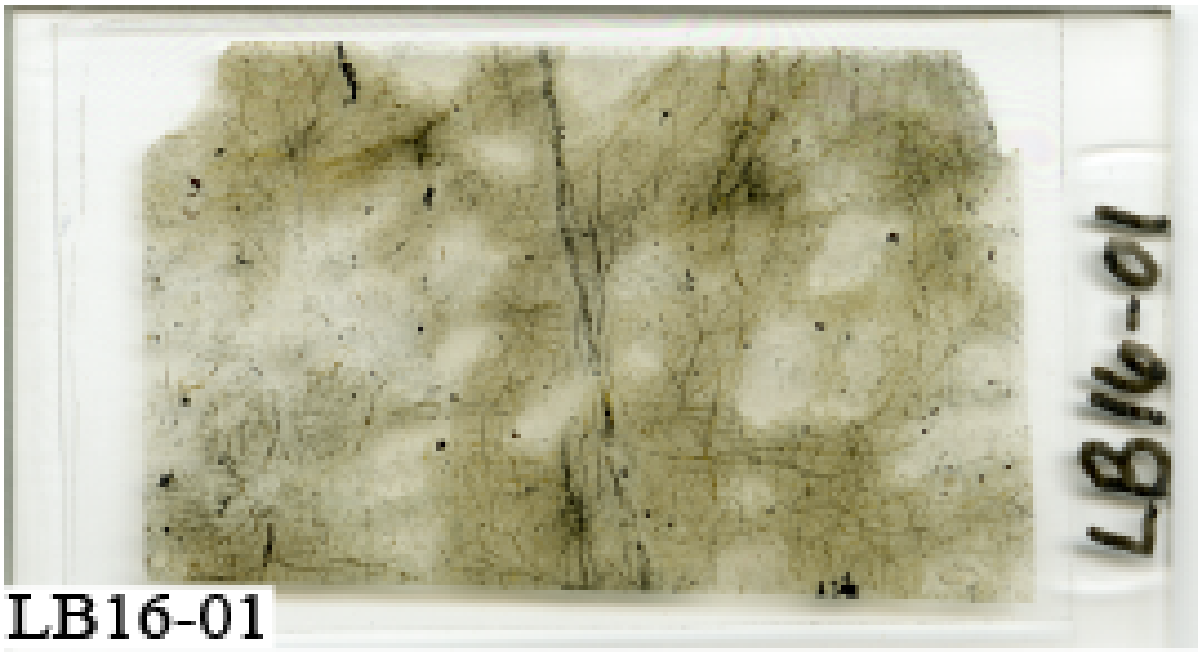

Figure B-1. *Scan of sample LB16-01 thin section.*

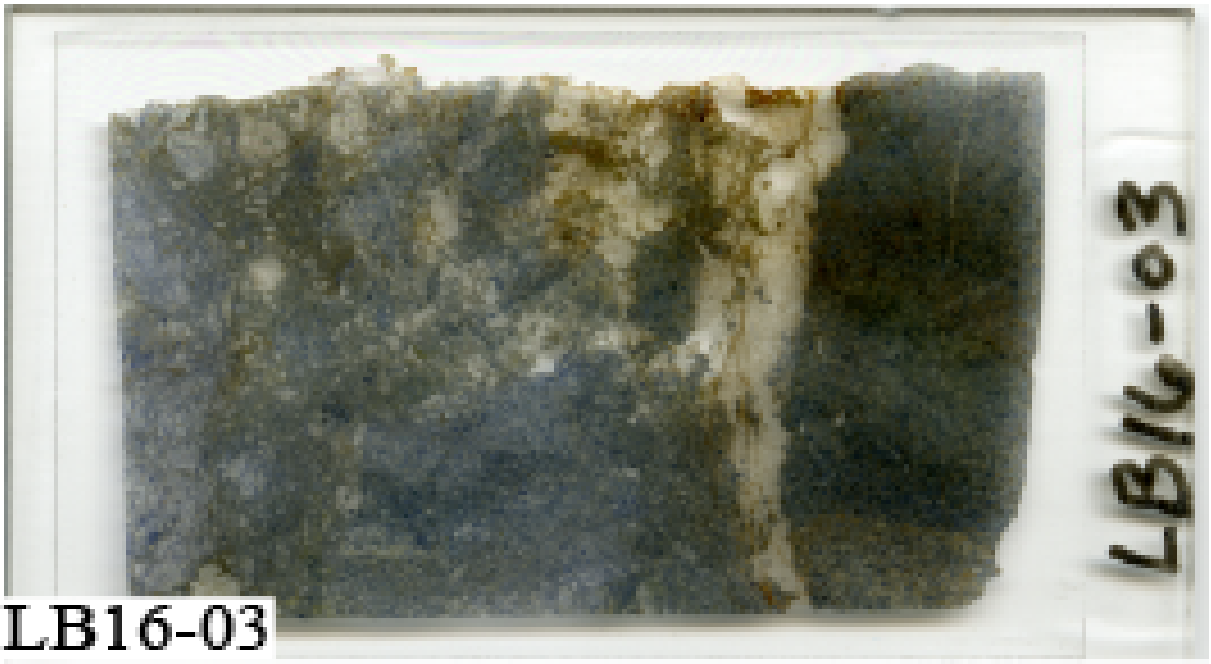

Figure B-2. *Scan of sample LB16-03 thin section.*

Figure B-3. *Scan of sample LB16-03 thin section.*

Figure B-4. *Scan of sample LB16-05 thin section.*

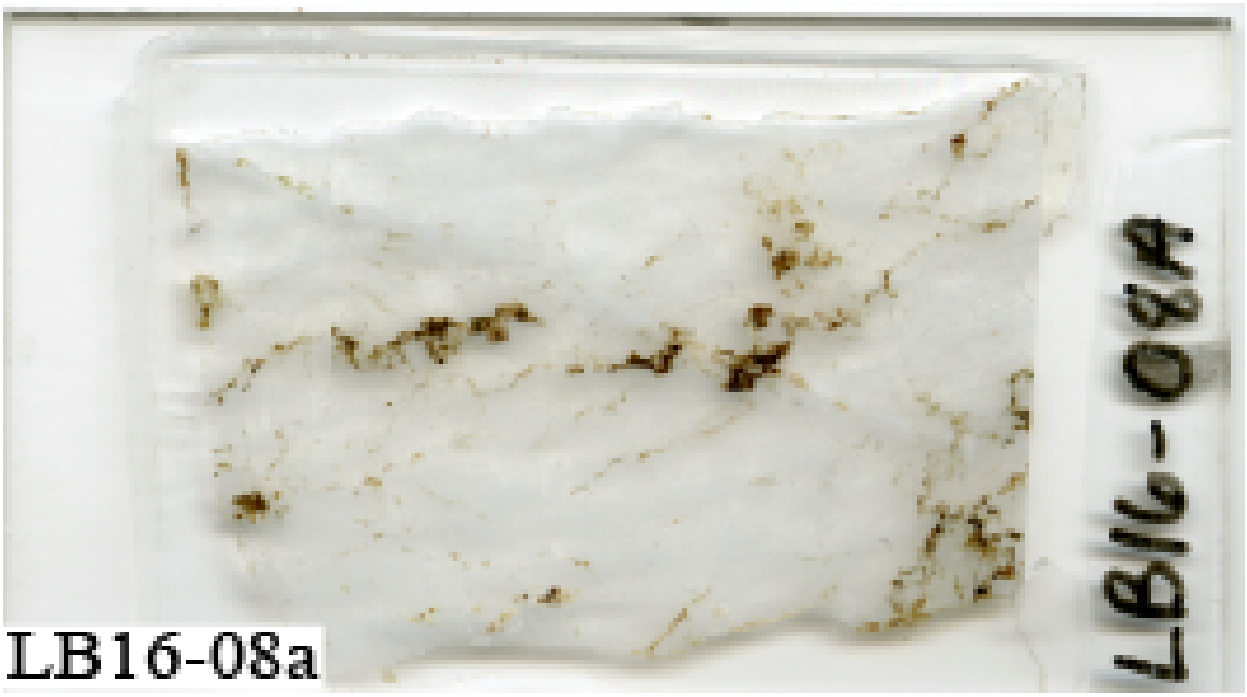

Figure B-5. *Scan of sample LB16-08a thin section.*

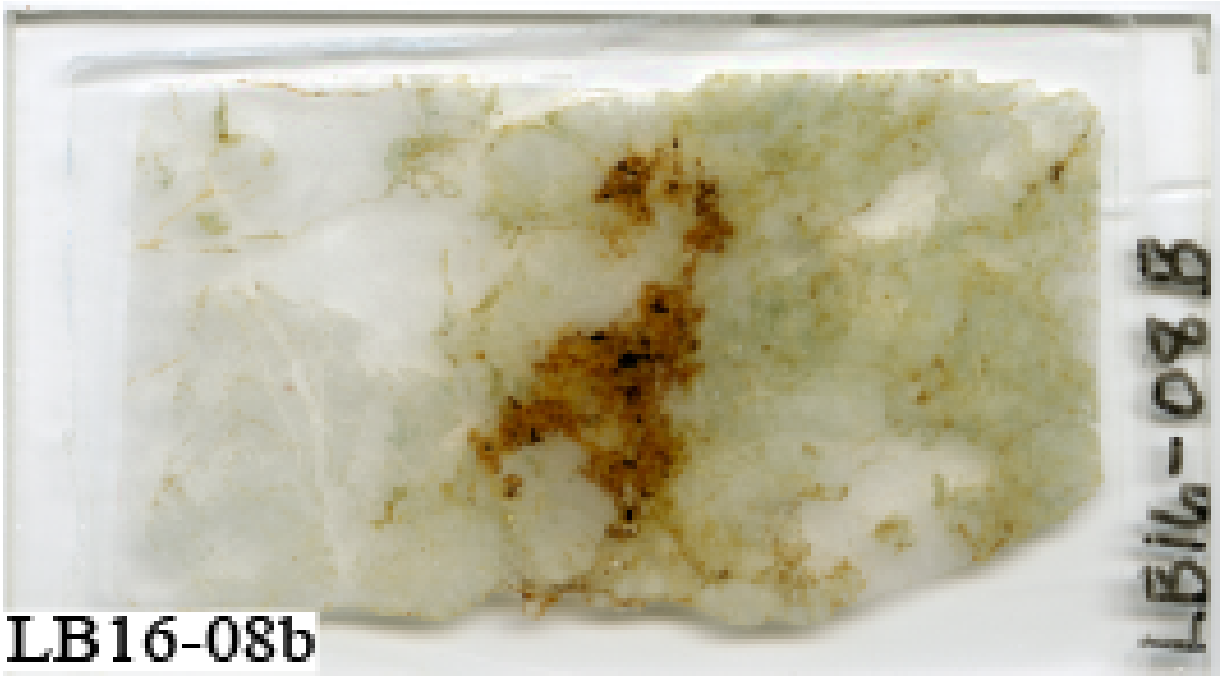

Figure B-6. *Scan of sample LB16-08b thin section.*

Figure B-7. *Scan of sample LB16-12 thin section.*

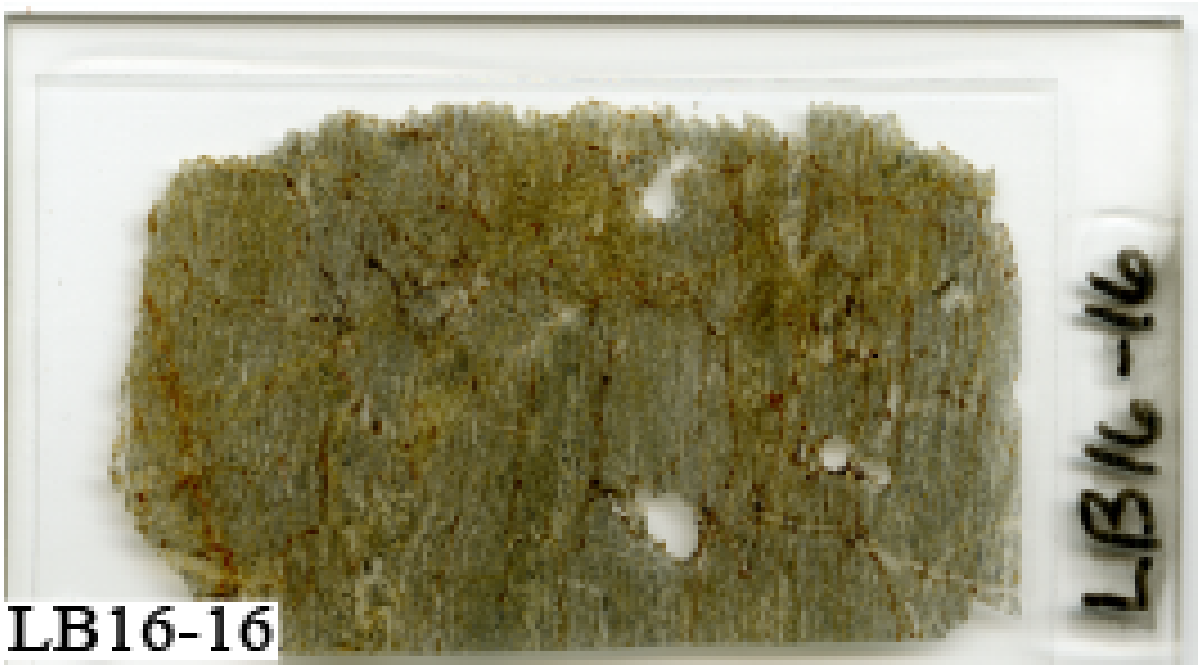

Figure B-8. *Scan of sample LB16-16 thin section.*

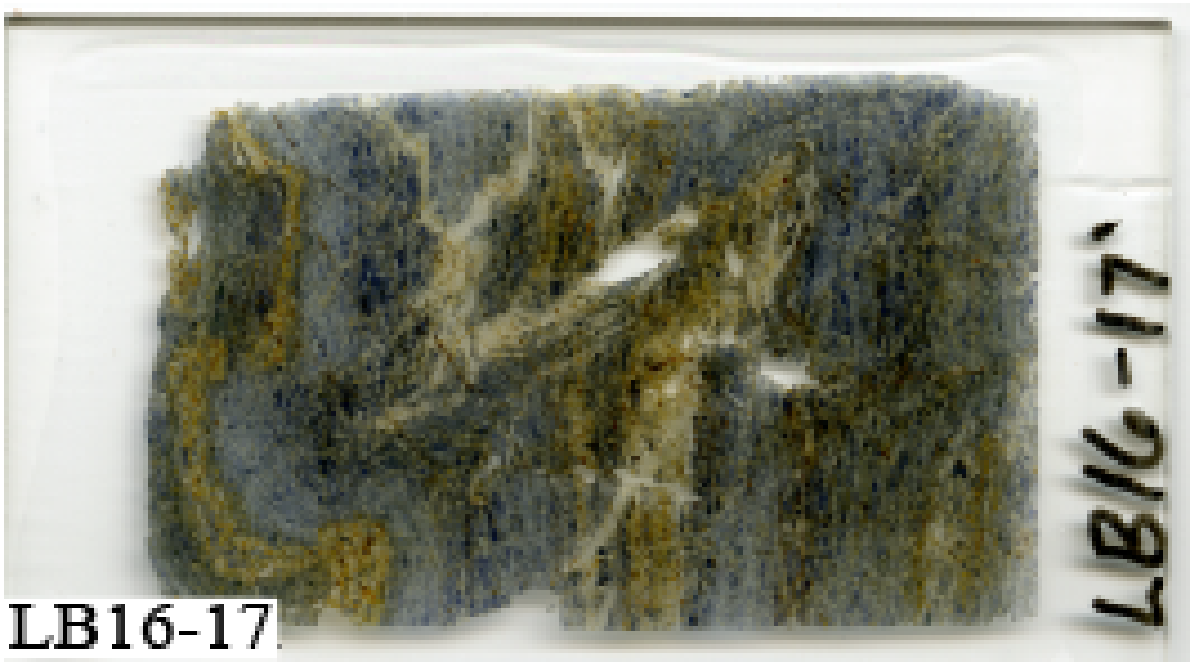

Figure B-9. *Scan of sample LB16-17 thin section.*

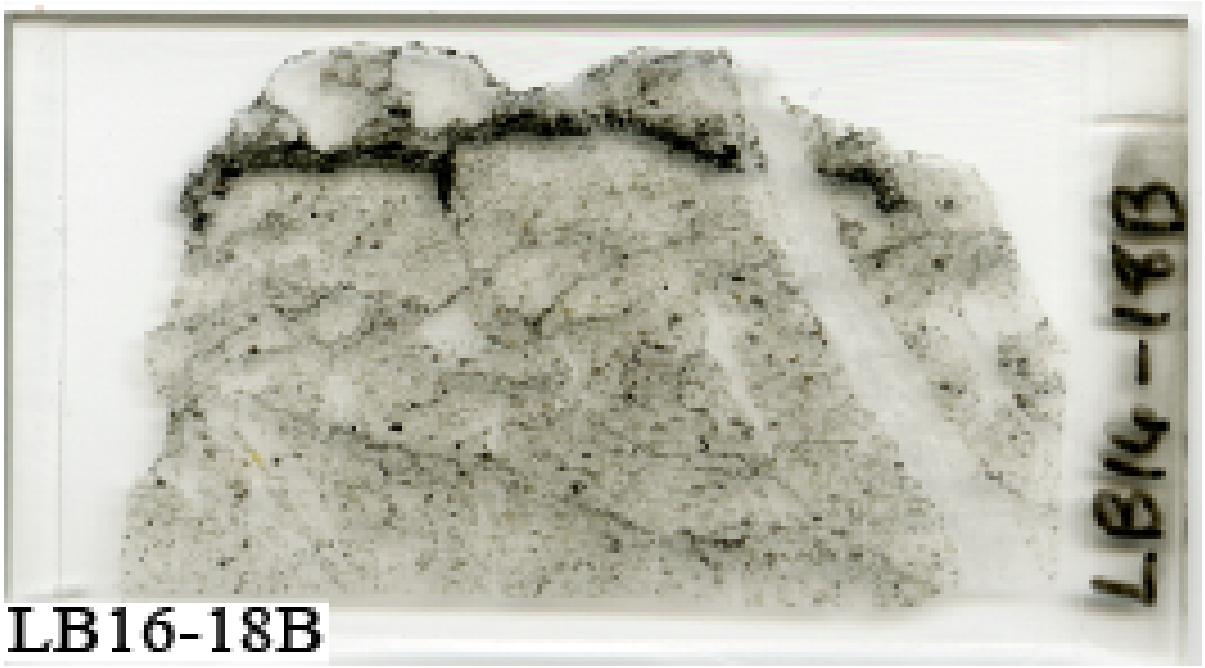

Figure B-10. *Scan of sample LB16-18b thin section.*

Figure B-11. *Scan of sample LB16-21 thin section.*

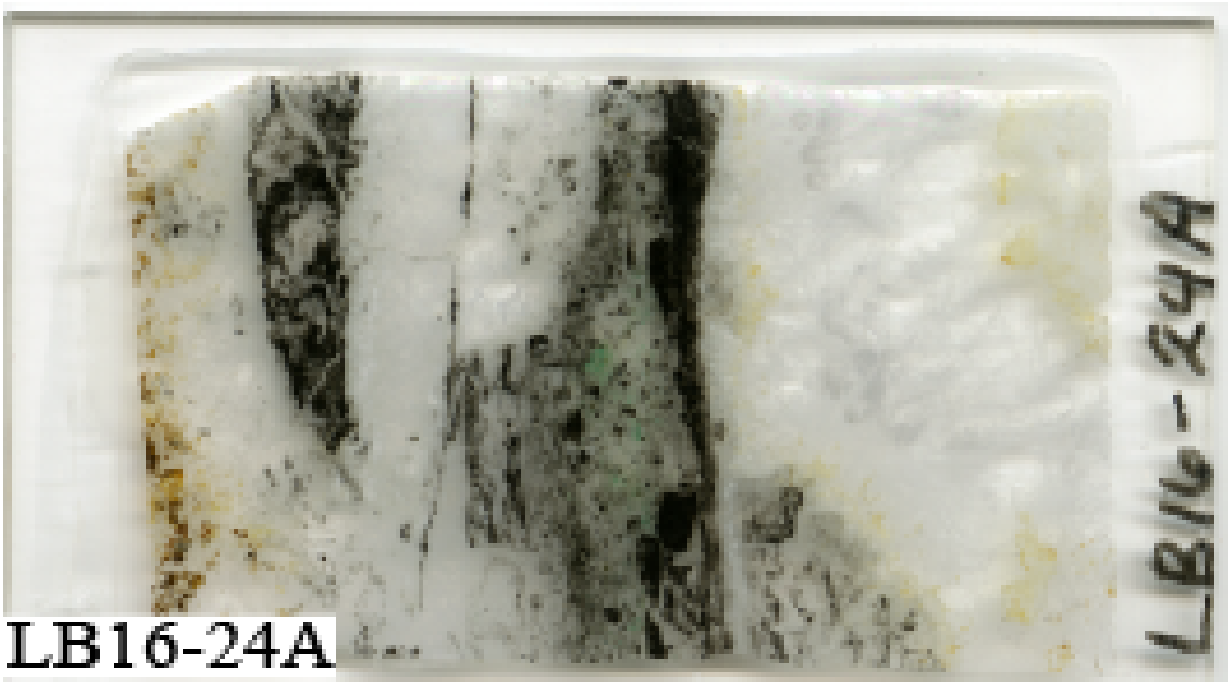

Figure B-12. *Scan of sample LB16-24a thin section.*

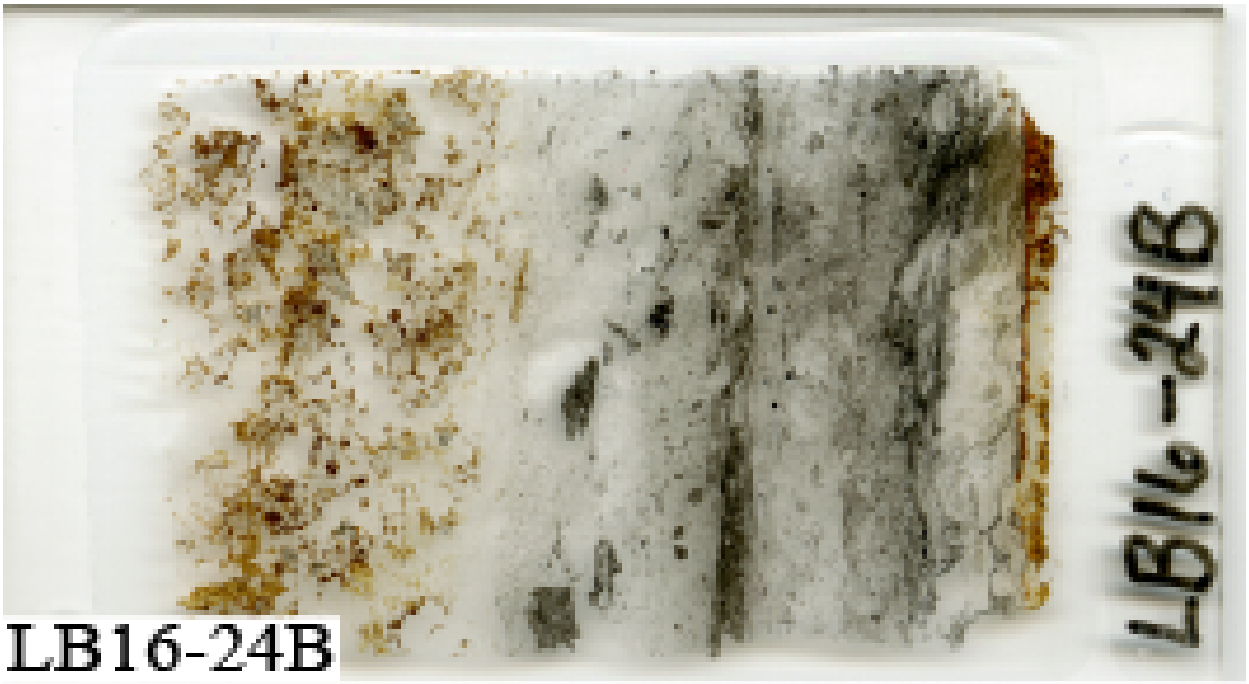

Figure B-13. *Scan of sample LB16-24b thin section.*

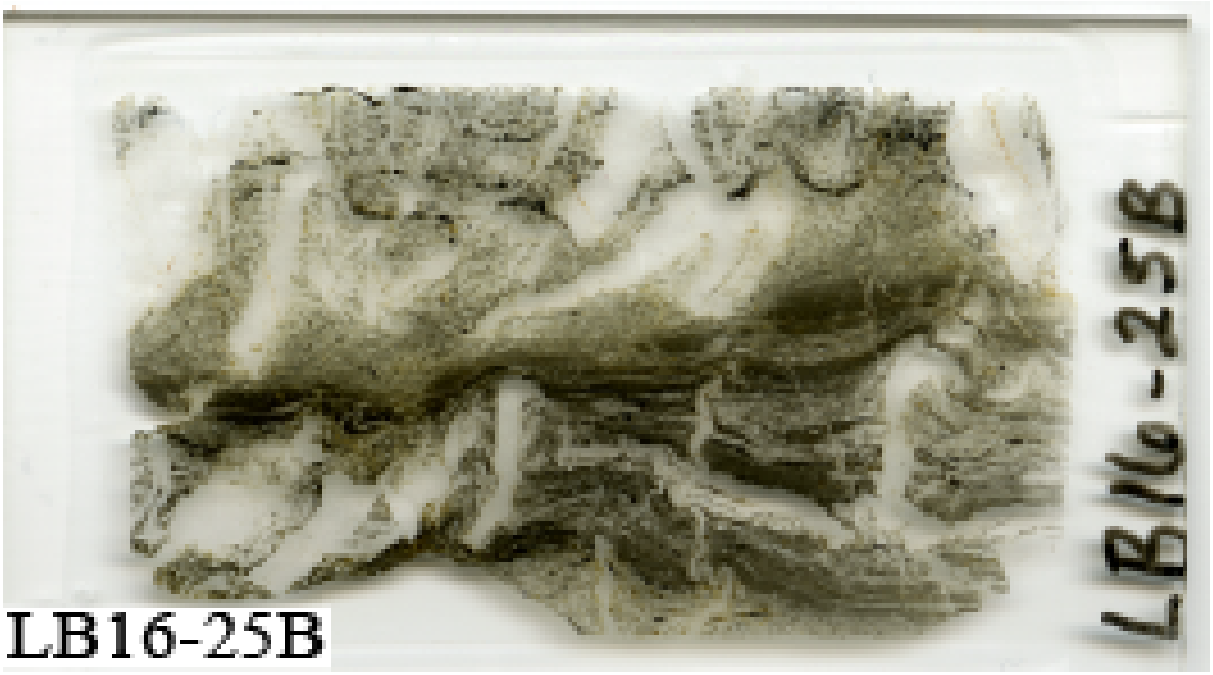

Figure B-14. *Scan of sample LB16-01 thin section.*

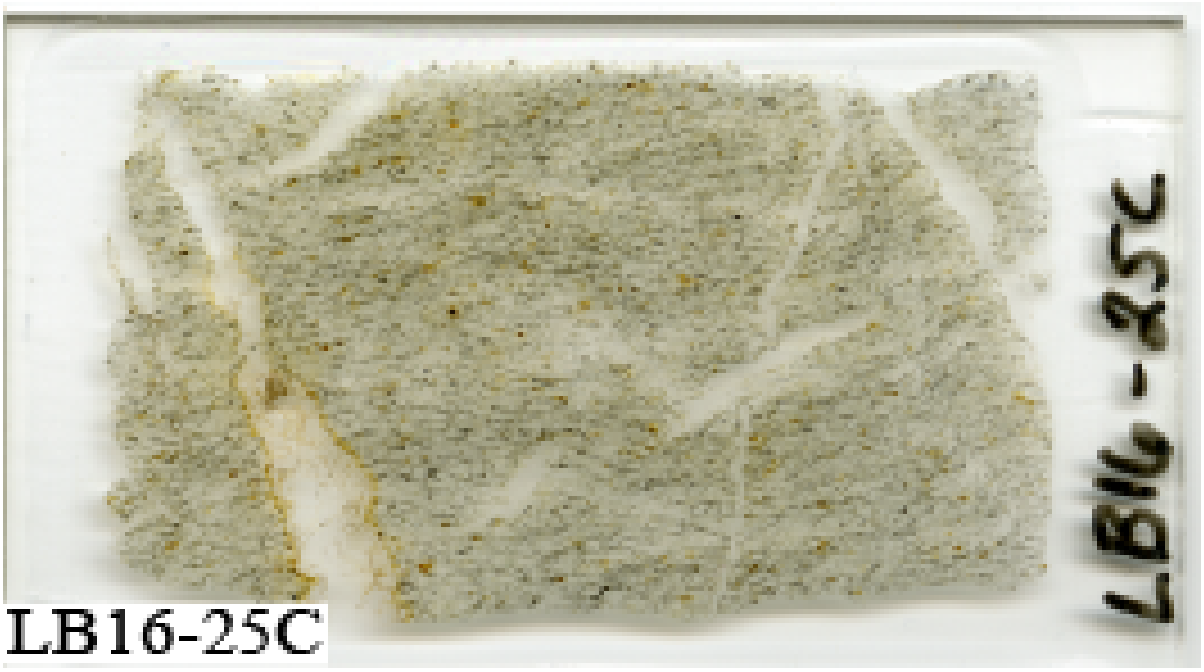

Figure B-15. *Scan of sample LB16-25c thin section.*

Figure B-16. *Scan of sample LB16-25d thin section.*

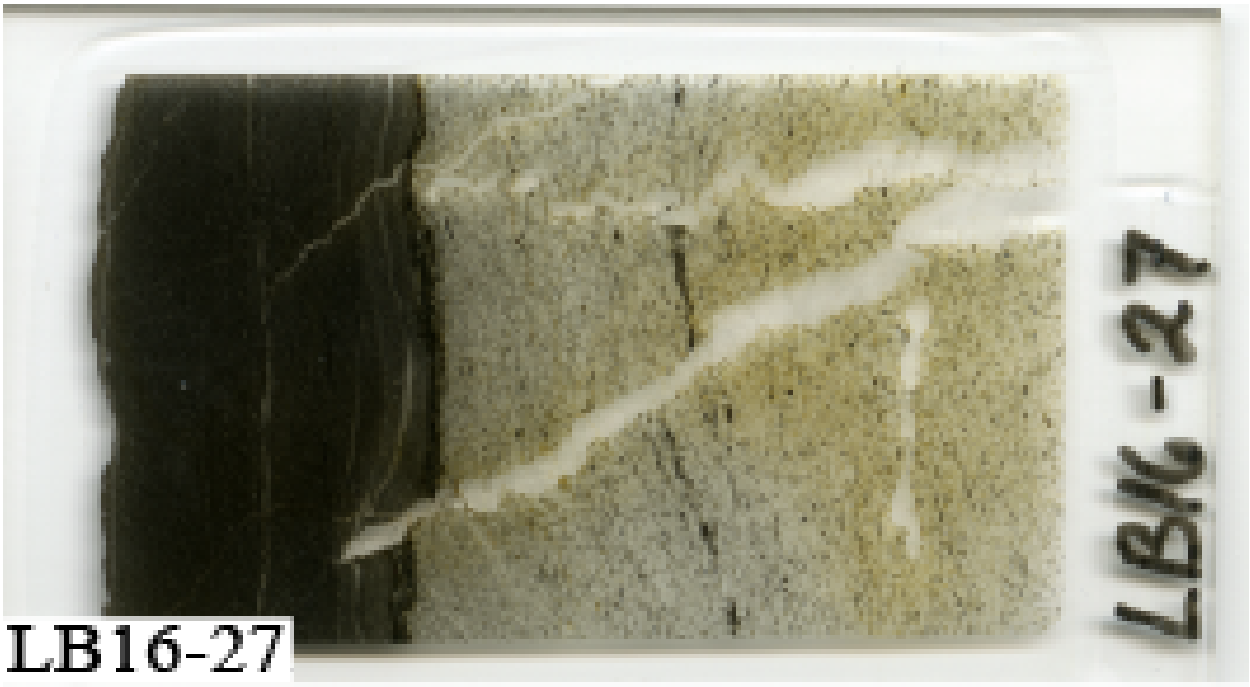

Figure B-17. *Scan of sample LB16-27 thin section.*

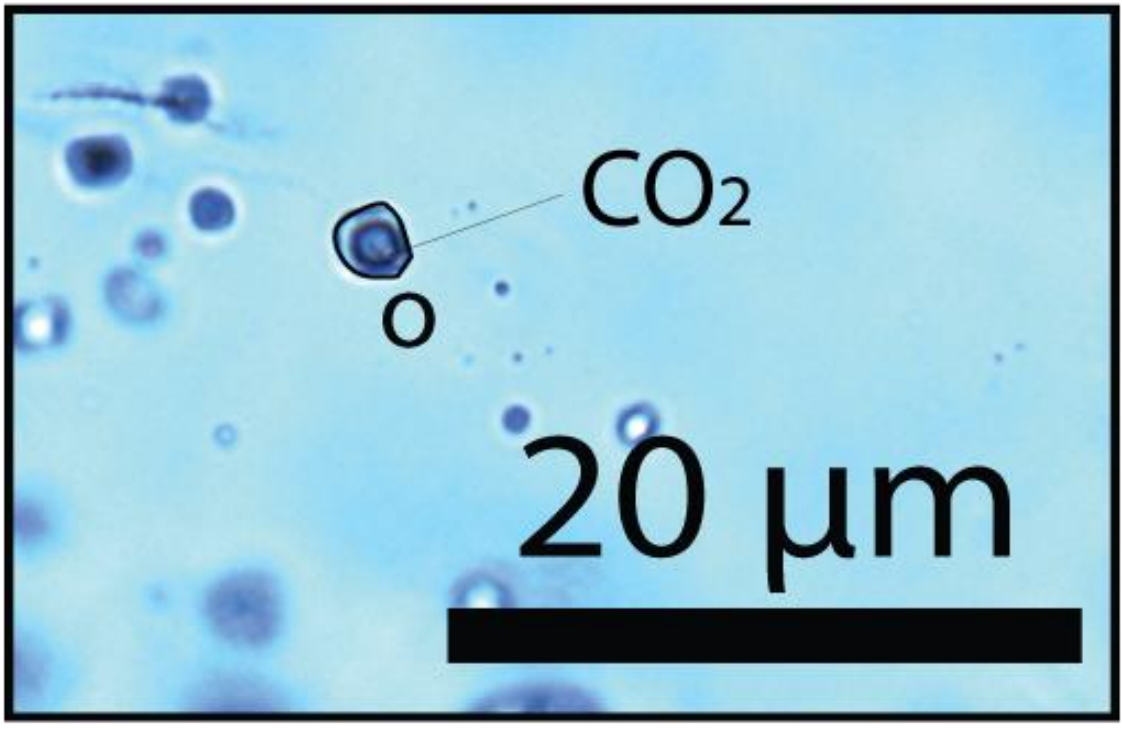

Figure B-18. *Representative photomicrograph of primary CO_2-bearing fluid inclusion from sample LB16-08a (as shown in **Figure 4-12**)*

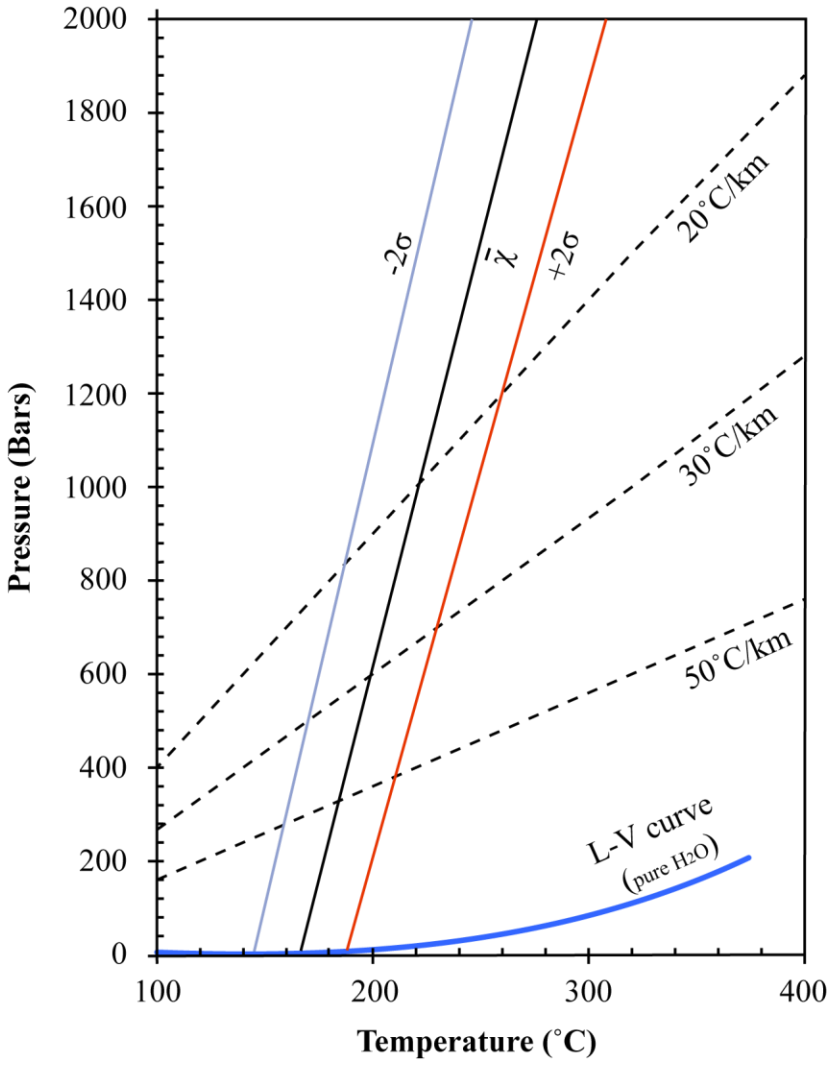

Figure B-19. *Isochore derived from the < 180˚C T_h population present across all samples.*

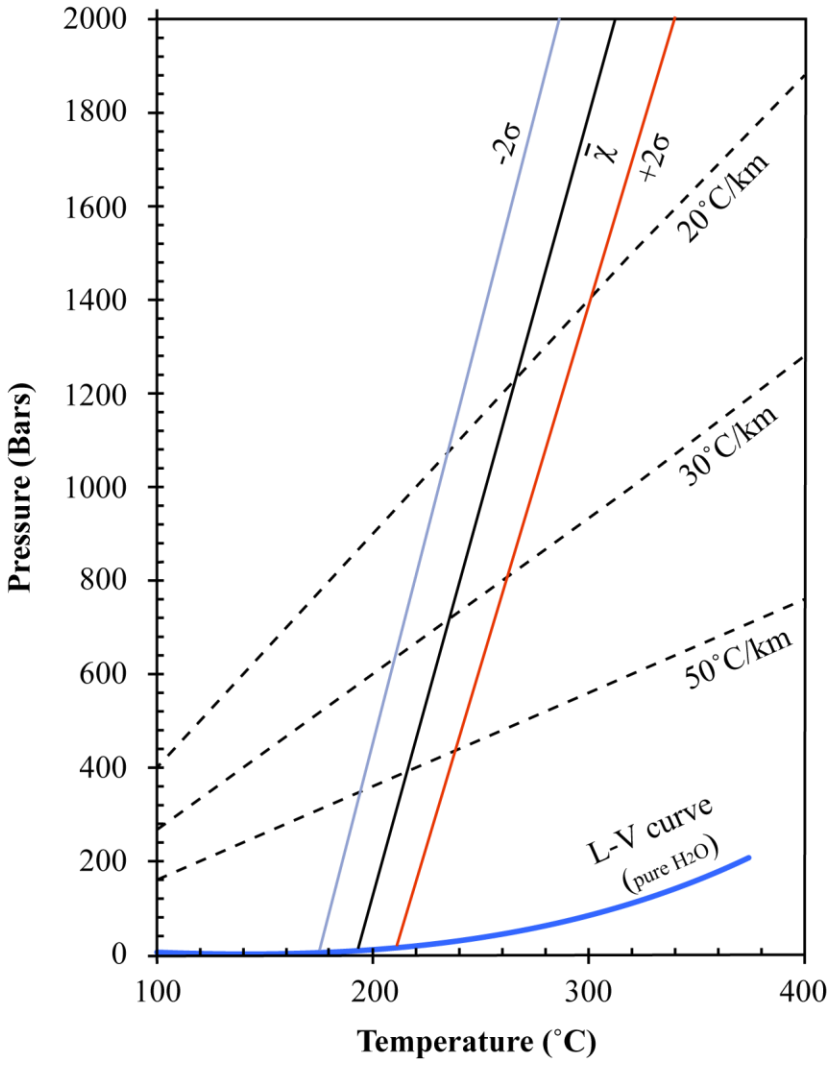

Figure B-20. *Isochore derived from the 180 - 210˚C T_h population present across all samples.*

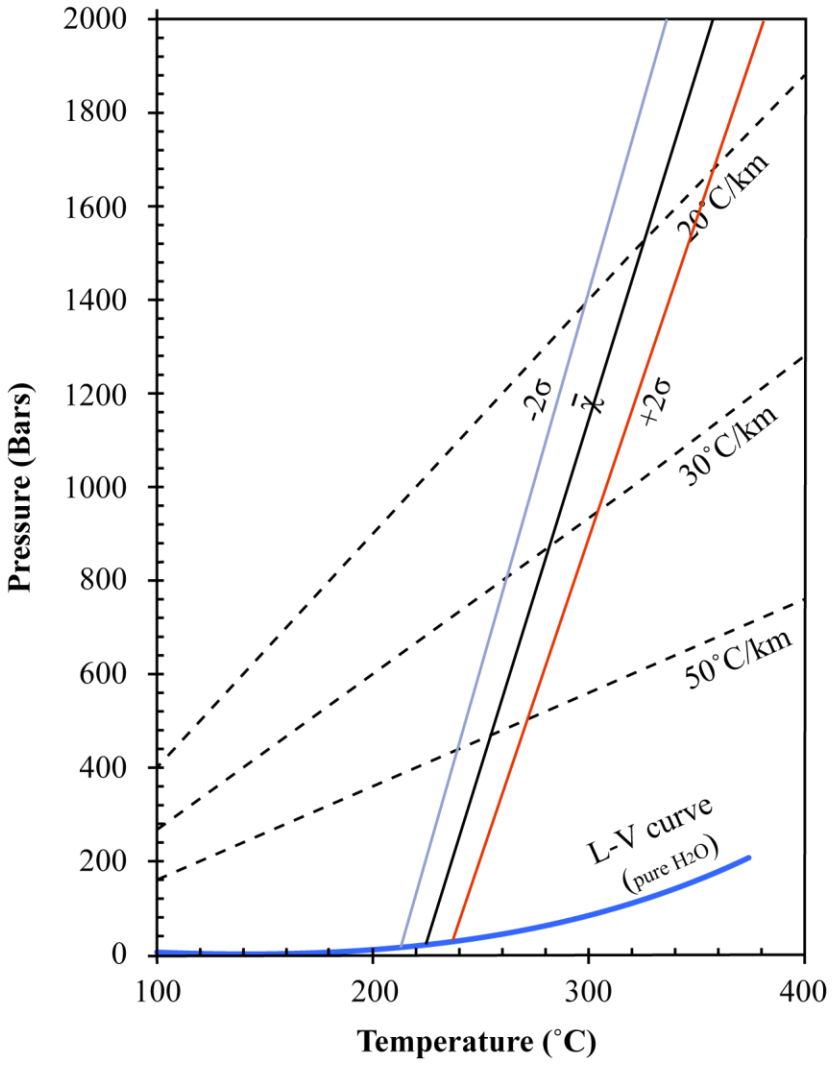

Figure B-21. *Isochore derived from the 210 - 235˚C T_h population present across all samples.*

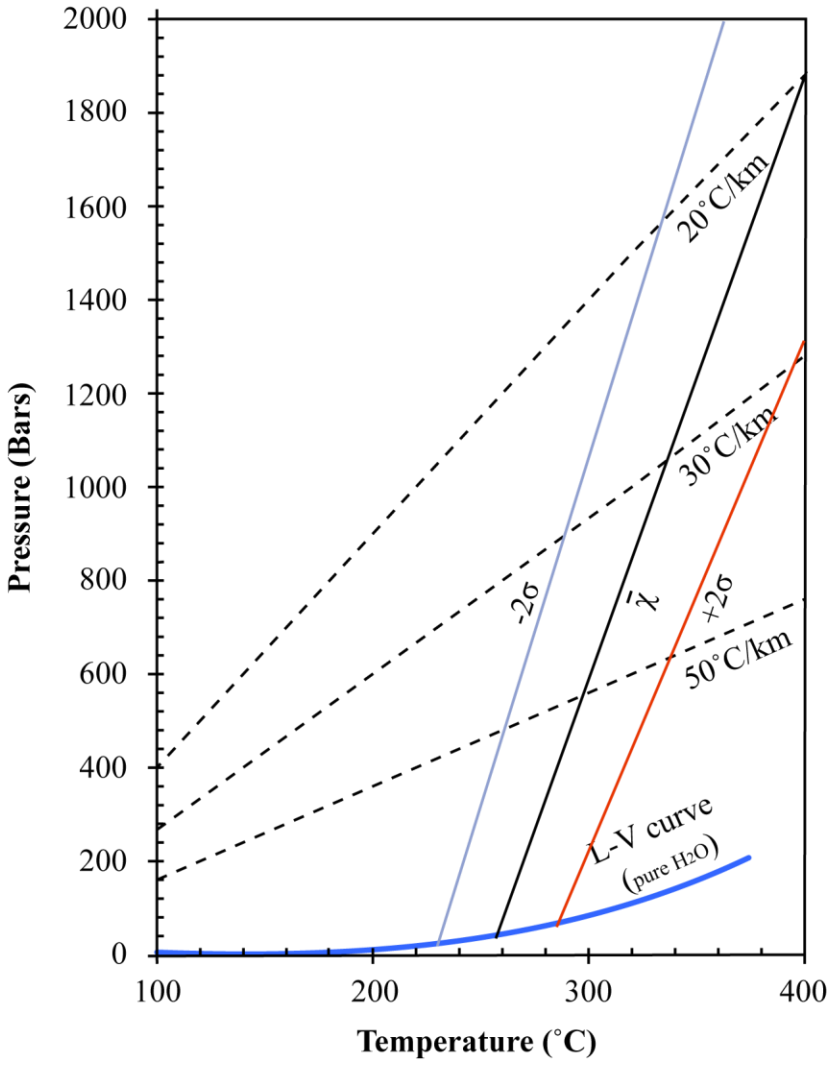

Figure B-22. *Isochore derived from the > 235˚C T_h population present across all samples.*

References

Adatte, T., Stinnesbeck, W., and Keller, G., 1996, Lithostrographic and mineralogic correlations of near K/T boundary clastic sediments in northeastern Mexico: Implications for origin and nature of deposition: Geological Society of America Special Papers 1996, no. 306, p. 211-226.

Blatt, H and Tracy, R. J., 1995, Petrology: Igneous, sedimentary and metamorphic. W. H. Freeman and Company, New York, p. 529.

Bierlein, F. P., and Smith, P. K., 2003, The Touquoy Zone deposit: an example of "unusual" orogenic gold mineralisation in the Meguma Terrane, Nova Scotia, Canada. *Canadian Journal of Earth Sciences*, v. 40, p. 447-466.

Bodnar, R. J., 1993, Revised equation and table for determining the freezing point depression of H2O-NaCl solutions. *Geochimica et Cosmochimica Acta*, v. *57*, p. 683-684.

Bodnar, R. J., 2003, Introduction to fluid inclusions: Analysis and interpretation, Samson, I., Anderson, A., and Marshall, D., eds: Mineralogical Association of Canada, Short Course 32, p. 1-8.

Chapman, A. D., Jacobson, C. E., Ernst, W. G., Grove, M., Dumitru, T., Hourigan, J., and Ducea, M. N., 2016, Assembling the world's type shallow subduction complex: Detrital zircon geochronologic constraints on the origin of the Nacimiento block, central California Coast Ranges. *Geosphere*, v. 12, p. 533-557.

Craw, D., 2002, Geochemistry of late metamorphic hydrothermal alteration and graphitisation of host rock, Macraes gold mine, Otago Schist, New Zealand. *Chemical Geology*, v. 191, p. 257-275.

Davis, C. H., 1912, The Los Burros mining district: Mining and Scientific Press, v. 104, p. 696-698.

Duan, Z., Moller, N., Greenberg, J., Weare, J.H., 1992, The prediction of methane solubility in natural waters to high ionic strength from 0 to 250˚C and from 0 to 1600 bars: *Geochimica et Cosmochimica Acta*, v. 56, p. 1451-1460.

Dubessy, J., Buschaert, S., Lamb, W., Pironon, J., and Thiéry, R., 2001, Methane-bearing aqueous fluid inclusions: Raman analysis, thermodynamic modelling and application to petroleum basins: *Chemical Geology*, v. 173, p. 193-205.

Ernst, W. G., 1980, Mineral paragenesis in Franciscan metagraywackes of the Nacimiento Block, a subduction complex of the Southern California Coast Ranges. *Journal of Geophysical Research: Solid Earth*, v. 85, p. 7045-7055.

Ernst, W. G., 2015, Franciscan geologic history constrained by tectonic/olistostromal high-grade metamafic blocks in the iconic California Mesozoic-Cenozoic accretionary complex. *American Mineralogist*, v. 100, p. 6-13.

Frezzotti, M. L., Tecce, F., Casagle, A., 2012, Raman spectroscopy or fluid inclusion analysis: *Journal of Geochemical Exploration*, v. 112, p. 1-20

Gao, Z.L. and Kwak, T.A.P., 1995. Turbidite-hosted gold deposits in the Bendigo-Ballarat and Melbourne Zones, Australia. I. Geology, Mineralization, stable isotopes, and implications for exploration. *International Geology Reviews*, v. 37, pp. 910–944

Gilbert, W. G., 1973, Franciscan rocks near sur fault zone, northern santa lucia range, california. *Geological Society of America Bulletin*, v. 84, p. 3317-3328.

Goldfarb, R. J., Groves, D. I., and Gardoll, S., 2001, Orogenic gold and geologic time: A global synthesis: *Ore Geology Reviews*, v. 18, p. 1-75.

Goldstein, R.H., Reynolds, T.J., 1994. Fluid inclusion microthermometry. In: Goldstein, R.H. (Ed.), Systematics of fluid inclusions in diagenetic minerals. SEPM Short Course, v. 31. SEPM (Society for Sedimentary Geology), Tulsa, Oklahoma, p. 87–121.

Graymer, R.W., Langenheim, V.E., Roberts, M.A., and McDougall, Kristin, 2014, Geological and geophysical maps of the eastern three-fourths of the Cambria 30’ x 60’ quadrangle, central California Coast Ranges. U.S. Geological Survey Scientific Investigations Map 3287, 1:100,000 scale, map sheets, 47 p.

Groves, D.I., Goldfarb, R.J., Gebre-Mariam, H., Hagemann, S.G., and Robert, F., 1998. Orogenic gold deposits—a proposed classification in the context of their crustal distribution and relationship to other gold deposit types: *Ore Geology Reviews*, v. 13, p. 7–27.

Guillaume, D., Teinturier, S., Dubessy, J., and Pironon, J., 2003, Calibration of methane analysis by Raman spectroscopy in H2O–NaCl–CH4 fluid inclusions. *Chemical Geology*, v. *194*, 41-49.

Hall, C.A., 1991, Geology of the Point Sur–Lopez Point region, Coast Ranges, California: A part of the Southern California allochthon: Geological Society of America Special Paper 266, 40 p.

Hamilton, F., 1916, Mines and mineral resources of the counties of Monterey, San Benito, San Luis Obispo, Santa Barbara, Ventura: Chapters of state mineralogist's report- Biennial period 1915-1916, p. 8-11.

Haynes, S. J., Keppie, J. D., and Boyle, R. W., 1986, Geology and chemistry of turbidite-hosted gold deposits: greenschist facies, eastern Nova Scotia. *Turbidite-hosted gold deposits*, p. 161-178.

Henne, A., and Craw, D., 2012, Synmetamorphic carbon mobility and graphite enrichment in metaturbidites as a precursor to orogenic gold mineralisation, Otago Schist, New Zealand. *Mineralium Deposita*, v. 47, p. 781-797.

Hill, J.M., 1922, The Los Burros District, Monterey County, California: *Contributions to Economic Geology*, Part I, p. 323-336.

Hu, S., Evans, K., Craw, D., Rempel, K., Bourdet, J., Dick, J., and Grice, K., 2015, Raman characterization of carbonaceous material in the Macraes orogenic gold deposit and metasedimentary host rocks, New Zealand: *Ore Geology Reviews*, v. 70, p. 80-95.

Jackson, M. L., 1969, Soil Chemical Analysis-Advanced Course. *Soil Chemical Analysis-Advanced Course.*, 2nd ed.

Kříbek, B., Sýkorová, I., Machovič, V., Knésl, I., Laufek, F., and Zachariáš, J., 2015, The origin and hydrothermal mobilization of carbonaceous matter associated with Paleoproterozoic orogenic-type gold deposits of West Africa: *Precambrian Research*, v. 270, p. 300-317.

Kübler B., 1964, Les argiles, indicateurs de me´tamorphisme. Revue de l'Institut Francaise du Petrole, v. 19, p. 1093-1112.

Kübler B, and Jaboyedoff M, 2000, Illite crystallinity: *Earth and Planetary Sciences*, v. 331, p. 75-89.

Lafuente, B., Downs, R.T., Yang, H., Stone, N., 2015, The power of databases; the RRUFF project. In: Highlights in Mineralogical Crystallography, T. Armbruster and R. M. Danisi, eds. Berlin, Germany, W. De Gruyter, p. 1-30.

Lahfid, A., Beyssac, O., Deville, E., Negro, F., Chopin, C., and Goffé, B., 2010, Evolution of the Raman spectrum of carbonaceous material in low-grade metasediments of the Glarus Alps (Switzerland). *Terra Nova*, v. 22, p. 354-360.

Lahfid, A., Delchini, S., and Lacroix, B., 2015, Contribution of the RSCM geothermometry to detect the thermal anomalies and peak temperatures induced by fluid circulation in

metasediments: 13th SGA Biennial Meeting, Aug 2015, Nancy, France. 2015. <hal-01164177>

Lahfid, A., Lacroix, B., Delchini, S., and Hughes, J., 2016, Thermal Anomaly Engendered by the Emplacement of an Au-deposit: Example from the Franciscan Complex. *In:* AGU Fall Meeting Abstracts.

Lindgren, W., 1909, Metallogenetic epochs: Economic Geology v. 4, p. 409– 420.

Lori, L. M. A., 2016, *Exhumation of the Nacimiento block: A thermochronologic analysis*. Missouri University of Science and Technology.

Lünsdorf, N. K., Dunkl, I., Schmidt, B. C., Rantitsch, G., and Eynatten, H., 2014, Towards a higher comparability of geothermometric data obtained by Raman spectroscopy of carbonaceous material. Part I: evaluation of biasing factors. *Geostandards and Geoanalytical Research*, v. 38, p. 73-94.

Moore, D. M., and Reynolds, R. C., 1997, *X-ray Diffraction and the Identification and Analysis of Clay Minerals*, v. 332, New York: Oxford university press.

Morisani, A.M., Housh, T.B., Tripathy, Alka, Jacobsen, C.E., and Cloos, M., 2005, Detrital zircon geochronology of greywacke blocks within the Franciscan mélange at San Simeon, California—Depositional age and provenance implications [abs.]: Geological Society of America Abstracts with Programs, v. 37, no. 7, p. 18-19.

N'diaye, I., Essaifi, A., Dubois, M., Lacroix, B., Goodenough, K.M., and Maacha, L., 2016, Fluid flow and polymetallic sulfide mineralization in the Kettara shear zone (Jebilet Massif, Variscan Belt, Morocco): Journal of African Earth Sciences, v. 119, p. 17-37.

Page, B. M., 1970, Sur-Nacimiento fault zone of California: Continental margin tectonics: Geological Society of America Bulletin, v. 81, p. 668–690.

Peterson, E.C., and Mavrogenes, J.A., 2014, Linking high-grade gold mineralization to earth-quake-induced fault-valve processes in the Porgera gold deposit, Papua New Guinea: Geology, doi: 10.1130/G35286.1.

Phillips, G.N., 2013, Australian and global setting for gold in 2013, *in* Proceedings, World Gold 2013, Brisbane, Australia, 26–29 September 2013: Carlton, Victoria, The Australian Institute of Mining and Metallurgy, p. 15–21.

Roedder, E., and Bodnar, R. J., 1980, Geologic pressure determinations from fluid inclusion studies. *Annual Review of Earth and Planetary Sciences*, *8*(1), p. 263-301.

Roedder, E and Ribbe, P.H., series ed., 1984, Fluid inclusions: Washington, D.C., Mineralogical Society of America, Reviews in Mineralogy, v. 12, 646 p.

Seiders, V. M., 1989a, Geologic map of Burnett Peak quadrangle, Monterey and San Luis Obispo counties, California: U.S. Geological Survey Geological Quadrangle Map GQ-1658, 1 sheet, 1:24,000 scale.

Seiders, V. M., 1989b, Geologic map of the Burro Mountain quadrangle, Monterey and San Luis Obispo counties, California: U.S. Geological Survey Miscellaneous Field Studies Map MF-2090, 1 sheet, 1:24,000 scale.

Seward, T. M., 1973, Thio complexes of gold and the transport of gold in hydrothermal ore solutions: *Geochimica et Cosmochimica Acta*, v. *37*, p. 379-399.

Sherlock, R. L., Tosdal, R. M., Lehrman, N. J., Graney, J. R., Losh, S., Jowett, E. C., and Kesler, S. E., 1995, Origin of the McLaughlin mine sheeted vein complex: Metal zoning, fluid inclusion, and isotopic evidence: *Economic Geology*, v. 90, p. 2156-2181.

Stoffer, P.W., 2006, Where's the San Andreas Fault? A guidebook to tracing the fault on public lands in the San Francisco Bay region: U.S. Geological Survey General Interest Publication 16, 123 p., online at http://pubs.usgs.gov/gip/2006/16/.

Suppe, J., and Armstrong, R.L., 1972, Potassium argon dating of Franciscan metamorphic rocks: *American Journal of Science*, v. 272, p. 217–233.

Taberner, C., Sosa, G., van den Kerkhof, A., Sneep, J., and Bell, A., 2012, Burial Dolomitization, Late Leaching and Thermochemical Sulphate-reduction Diagenesis in Arab C and D Reservoirs (Kingdom of Saudi Arabia): Impact on Reservoir Properties. In *Fourth EAGE Workshop on Arabian Plate Geology*.

Tomkins, A. G., 2013, On the source of orogenic gold. *Geology*, v. 41, no. 12, p. 1255–1256.

Trelan, W., 1888, California State Mineralogist Bureau Eighth Annual Report., p. 405-410.

Underwood, M. B., Laughland, M. M., Shelton, K. L., and Sedlock, R. L., 1995, Thermal-maturity trends within franciscan rocks near big sur, california: Implications for offset along the San Gregorio– San Simeon–Hosgri fault zone: *Geology*, v. 23, no. 9, p. 839-842.

United States Department of Labor, 2016. Bureau of Labor Statistics CPI Inflation Calculator. http://www.bls.gov/data/inflation_calculator.htm.

Verdel, C., van der Pluijm, B. A., Niemi, N., 2012, Variation of illite/muscovite $^{40}Ar/^{39}Ar$ age spectra during progressive low-grade metamorophism: An example from the US Cordillera: *Contributions to Mineralogy and Petrology*, v. 164, iss. 3, p. 521-536.